



January 2021

Analysis Of The 12 February 2020 Red River Valley Ground Blizzard During The Blown-Under Campaign

Alec T. Szczepanski

[How does access to this work benefit you? Let us know!](#)

Follow this and additional works at: <https://commons.und.edu/theses>

Recommended Citation

Szczepanski, Alec T., "Analysis Of The 12 February 2020 Red River Valley Ground Blizzard During The Blown-Under Campaign" (2021). *Theses and Dissertations*. 4187.
<https://commons.und.edu/theses/4187>

This Thesis is brought to you for free and open access by the Theses, Dissertations, and Senior Projects at UND Scholarly Commons. It has been accepted for inclusion in Theses and Dissertations by an authorized administrator of UND Scholarly Commons. For more information, please contact und.common@library.und.edu.

ANALYSIS OF THE 12 FEBUARY 2020 RED RIVER VALLEY GROUND BLIZZARD
DURING THE BLOWN-UNDER CAMPAIGN

by

Alec Tyler Szczepanski
Bachelor of Science, State University of New York at Oswego, 2019

A Thesis

Submitted to the Graduate Faculty

of the

University of North Dakota

in partial fulfillment of the requirements

for the degree of
Master of Science

Grand Forks, North Dakota

December
2021

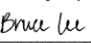
Copyright 2021 Alec Tyler Szczepanski

Name: Alec Szczepanski
Degree: Master of Science

This document, submitted in partial fulfillment of the requirements for the degree from the University of North Dakota, has been read by the Faculty Advisory Committee under whom the work has been done and is hereby approved.

DocuSigned by:

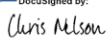
AARON KENNEDY
AARON KENNEDY

DocuSigned by:

BRUCE LEE
BRUCE LEE

DocuSigned by:

MARK ASKELSON
MARK ASKELSON

This document is being submitted by the appointed advisory committee as having met all the requirements of the School of Graduate Studies at the University of North Dakota and is hereby approved.

DocuSigned by:

CHRIS NELSON
Chris Nelson
Dean of the School of Graduate Studies
12/8/2021

Date

PERMISSION

Title Analysis of the 12 February 2020 Red River Valley Ground Blizzard During
the BLOWN-UNDER Campaign

Department Atmospheric Sciences

Degree Master of Science

In presenting this thesis in partial fulfillment of the requirements for a graduate degree from the University of North Dakota, I agree that the library of this University shall make it freely available for inspection. I further agree that permission for extensive copying for scholarly purposes may be granted by the professor who supervised my thesis work or, in his absence, by the Chairperson of the department or the dean of the School of Graduate Studies. It is understood that any copying or publication or other use of this thesis or part thereof for financial gain shall not be allowed without my written permission. It is also understood that due recognition shall be given to me and to the University of North Dakota in any scholarly use which may be made of any material in my thesis.

Alec Tyler Szczepanski
9 December 2021

TABLE OF CONTENTS

LIST OF FIGURES	viii
LIST OF TABLES	xiv
ACKNOWLEDGMENTS	xv
ABSTRACT	xvi
CHAPTER 1. INTRODUCTION	1
1.1. Blowing Snow and Blizzards	1
1.1.1. Properties of Blowing Snow	1
1.1.2. Types of Blizzards	3
1.1.3. Impacts and Hazards of Blowing Snow and Blizzards	4
1.2. Winter in the Red River Valley	6
1.2.1. Blowing Snow Plumes in the Red River Valley	7
1.3. Previous Blowing Snow Research	8
1.3.1. Surface-Based Remote-Sensing Research	8
1.3.2. Satellite-Based Research	11
1.3.3. In Situ Research	13
1.4. Introduction to BLOWN-UNDER	15
1.5. Objectives	16
CHAPTER 2. DATA COLLECTION AND METHODOLOGY	21
2.1. Instrumentation	21
2.1.1. Surface In Situ Instrumentation	21

2.1.2. Balloon-borne In Situ Instrumentation	23
2.1.3. Radar and Remote-Sensing Instrumentation	24
2.2. Analysis Techniques	25
2.2.1. Surface and Balloon-borne Data Analysis	25
2.2.2. Microphysics and Hydrometeor Imaging Data Analysis	25
2.2.3. Radar and Remote-Sensing Data Analysis	27
CHAPTER 3. 12 FEBRUARY 2020 METEOROLOGICAL ENVIRONMENT	
 AND IMPACTS	34
3.1. Meteorological Environment	34
3.2. Weather and Societal Impacts	35
CHAPTER 4. RESULTS AND DISCUSSION	46
4.1. Radar and Remote Sensing Analysis	46
4.1.1. Radar Analysis	46
4.1.2. Lidar Analysis	50
4.1.3. Satellite Analysis	51
4.1.4. Discussion	54
4.2. Surface In Situ Analysis	56
4.2.1. OSCRE	56
4.2.2. OSCRE vs Parsivel ²	57
4.2.3. Discussion	58
4.3. Balloon-borne Data Analysis	58
4.3.1. Evolution of the Boundary Layer	58
4.3.2. PASIV	59

4.3.3. Spatial Variability of Thermodynamics	60
4.3.4. Discussion	61
4.4. Numerical Weather Model Performance	62
4.4.1. Pre-Frontal Passage	62
4.4.2. Post-Frontal Passage	63
4.4.3. Discussion	66
CHAPTER 5. SUMMARY AND CONCLUSIONS	108
12 Feb 2020 Synopsis	108
Instrument Performance	108
Boundary Layer Evolution and Blowing Snow Plumes	110
Model Performance	112
REFERENCES	114

LIST OF FIGURES

Figure	Page
1. An image of blowing snow captured with the OSCRE during the 12 February 2020 RRV ground blizzard.....	18
2. Average number of blizzards per 1000 km ² for the 1959-60 through 2013-14 winter seasons. Darker filling indicates more blizzards per 1000 square kilometers. Adapted from Coleman and Schwartz (2017).....	19
3. (a) A schematic of horizontal convective rolls. Arrows indicate how winds are flowing around and within the rolls, h is the height of the rolls, λ is the distance between rising branches (the wavelength of the HCRs), and ε is the angle between the roll axis and the mean boundary layer geostrophic wind. Adapted from Weckwerth et al. (1997). (b) An image from the 1.63- μm channel on <i>GOES-16</i> during the 12 Feb 2020 ground blizzard. The yellow box is the domain used in Fig. 4. The yellow star marks the location of Grand Forks, ND.....	20
4. A map showing locations of instrumentation and surface stations used during the 12 Feb 2020 blizzard. The black dot for UND is the location for the UND NorthPol radar and where balloon launches were conducted.....	29
5. (a) The temporary UND NDAWN mesonet station located at the Oakville Prairie Observatory near Emerado, ND. The mesonet station is built on a tripod in the foreground, with a Parsivel ² mounted to the fence in the background. (b) DOW7 after the 12 Feb 2020 event. On the bed of the truck is an X-band radar, seen as the dish pointing away from the cab of the truck. The 10-m mast holds instrumentation to collect meteorological data. Image of the DOW7 courtesy of Caitlin Connell....	30
6. A picture of the OSCRE. The camera (left housing) captures pictures of hydrometeors in its field of view at the same rate as the strobe light (right housing) flashes. Image courtesy of Dr. Aaron Kennedy.....	31
7. A picture of Dr. Aaron Kennedy holding the PASIV near Fertile, MN after retrieving the instrument from a test deployment on 6 Feb 2020. Image courtesy of Dr. Aaron Kennedy.....	32
8. Global Forecasting System (GFS) analysis MSLP (black contours; hPa) and surface temperatures (color shading; °C) for (a) 11 Feb 2020 at 1800 UTC, and (b) 12 Feb 2020 at 0000 UTC.....	37

9.	As in Fig. 8, except for (a) 12 Feb 2020 at 0600 UTC, and (b) 12 Feb 2020 at 1200 UTC.....	38
10.	GFS analysis data on 11 Feb 2020 at 1800 UTC for (a) 850 hPa heights (black contours; meters) and temperatures (colored shading; °C), and (b) 850 hPa heights (black contours; meters) and winds (colored shading; knots).....	39
11.	Snow depth over the Upper Midwest and Northern Plains ending at (a) 0600 UTC on 11 Feb 2020, and (b) 0600 UTC on 12 Feb 2020. Minimal new snowfall was recorded across the Dakotas between the two times. Figures courtesy of the National Operational Hydrologic Remote Sensing Center (NOHRSC).....	40
12.	Data from the GFS initialized at 00Z on 12 Feb 2020. (a) Black lines are model 500-hPa heights in meters at 12 UTC (12 hours into the simulation), semi-transparent grey contours are model 500-hPa wind speeds at 12 UTC, and red and blue shading indicate modelled 6-hour temperature advection at 925 hPa from 06 to 12 UTC, with blue shading indicating cold air advection and red shading indicating warm air advection. (b) Black lines are model MSLP in hPa at 12 UTC, red dashed lines are model surface temperatures in degrees Celsius at 12 UTC, and blue and red contours indicate modelled 6-hour MSLP changes from 06 to 12 UTC, with blue shading indicating pressure falls and red shading indicating pressure rises.....	41
13.	False color imagery captured with MODIS on NASA’s <i>Terra</i> satellite on 12 Feb 2020. Clouds from the exiting Alberta Clipper can be seen over central MN and extreme southeast ND. Blowing snow plumes within the RRV are pointed out.....	43
14.	Meteograms featuring (a) 2-meter temperatures at UND NDAWN; (b) 3-meter instantaneous wind speed and wind gusts for every minute, with wind speed in blue and wind gusts in red; and (c) raw Parsivel ² cumulative particle counts per minute in orange and KRDR visibility in blue.....	44
15.	Webcam imagery from (a) UND NDAWN at 0710 UTC (1:10 AM CST), (b) UND NDAWN at 0715 UTC (1:15 AM CST), (c) NDAWN Headquarters in Fargo, ND at 0914 UTC (3:14 AM CST), and (d) NDAWN HQ at 0915 UTC (3:15 AM CST). (a) and (c) are taken before the Arctic front passes through at the respective locations, and (b) and (d) are taken after the frontal passage when blizzard conditions commence.....	45

16.	Radar imagery from DOW7 at 0720 UTC and KMVX at 0721 UTC. The DOW7 elevation angle is 1.3° and the KMVX elevation angle is 0.5° . Panels (a) and (c) show DOW7 reflectivity and velocity, respectively. Panels (b) and (d) show KMVX reflectivity and velocity, respectively. The black dashed boxes in (b) and (d) denote the domain used in (a) and (c). The circles in each panel indicate the locations of the centers of the respective radars. The triangles in each panel indicate the location of Grand Forks, ND. The dot-dashed black lines in (a) and (c) denote the azimuthal angle used in the RHI plots in Fig. 22.....	69
17.	As in Fig. 16, except for (a) DOW7 differential reflectivity, (b) KMVX differential reflectivity, (c) DOW7 correlation coefficient, and (d) KMVX correlation coefficient.....	70
18.	As in Fig. 16, except for DOW7 data at 0740 UTC and KMVX data at 0738 UTC.	71
19.	As in Fig. 17, except for DOW7 data at 0740 UTC and KMVX data at 0738 UTC.	72
20.	As in Fig. 16, except for DOW7 data at 0752 UTC and KMVX data at 0756 UTC.	73
21.	As in Fig. 17, except for DOW7 data at 0752 UTC and KMVX data at 0756 UTC.	74
22.	DOW7 RHI (a) reflectivity, (b) storm-relative velocity, (c) differential reflectivity, and (d) correlation coefficient observed at 0728 UTC at an azimuthal angle of 27.5° with respect to north. The white arrow in (a) indicates the direction the front was moving with respect to the radar.....	75
23.	DOW7 RHI (a) reflectivity, (b) storm-relative velocity, (c) differential reflectivity, and (d) correlation coefficient observed at 0755 UTC at an azimuthal angle of 100° with respect to north.....	76
24.	Radar reflectivity observations at 0840 UTC for (a) DOW7 (1.3°), (b) UND NorthPol (2.0°), and (c) KMVX at (0.5°). The red dots in each panel indicate the locations of each of the respective radars. The black dashed boxes in (b) and (c) denotes the domain of panel (a). The white arrows in panel (a) point out a few of the blowing snow plumes seen by DOW7.....	77
25.	DOW7 PPI (a) reflectivity, (b) radial velocity, (c) differential reflectivity, and (d) correlation coefficient observed at 0852 UTC at an elevation angle of 1.3° . The black triangles in each panel indicate the location of Grand Forks, ND. The white arrows in (a) point out a couple of the blowing snow plumes investigated in RHI imagery in Fig. 26.....	78
26.	DOW7 RHI (a) reflectivity, (b) storm-relative velocity, (c) differential reflectivity, and (d) correlation coefficient observed at 0855 UTC at an azimuthal angle of 100° with respect to north. The white arrow in (a) indicates the locations of the chosen blowing snow plumes from Fig. 25.....	79

27. A time-height series of KMVX radar reflectivity near 47.61°N, 97.34°W approximately 12.8 km (8 miles) north-northwest of KMVX. The radar reflectivity for the bin closest to this point is plotted for every available volume scan..... 80
28. Panel (a) shows the maximum blowing snow depth as measured with the Lufft ceilometer averaged every 5 minutes (black line), DOW7 (red line), and KMVX (blue line) from 0600 to 2400 UTC on 12 Feb 2020. Panel (b) shows the corresponding ceilometer for the same time period. Times with falling and blowing snow are annotated in (b), in addition to the frontal passage (“FROPA”) and when the signal was attenuated..... 81
29. *GOES-16* imagery from the 1.63- μ m band (band 5) at (a) 1406 UTC, (b) 1506 UTC, (c) 1606 UTC, and (d) 1706 UTC on 12 Feb 2020. The yellow dot indicates Grand Forks, ND..... 82
30. As in Fig. 29, except for (a) 1806 UTC, (b) 1906 UTC, (c) 2006 UTC, and (d) 2106 UTC on 12 Feb 2020..... 83
31. Imagery from the MODIS instrument aboard NASA’s *Terra* satellite collected around 1700 UTC on 12 Feb 2020 using the 0.45- μ m, 1.628- μ m, and 2.105- μ m bands. The yellow box in panel (a) indicates the domain of panel (b). The yellow dot in each panel denotes the location of Grand Forks, ND..... 84
32. Imagery from *Sentinel-2* at 1730 UTC on 12 Feb 2020 using the 0.665- μ m, 1.614- μ m, and 2.202- μ m bands. The black dashed polygon in panel (a) indicates the domain of panel (b). The yellow dot in each panel denotes the location of Grand Forks, ND..... 85
33. The CALIOP 532-nm calibrated, attenuated backscatter observed along the path denoted in the subplot in the upper-right. The red and yellow stars denote the approximate locations of Fargo, ND and Grand Forks, ND, respectively. Figure courtesy of Stephen Palm..... 86
34. (a) 10-meter wind speeds as recorded with DOW7; (b) a PSD time-series for OSCRE from 0645 to 0815 UTC, with times shifted 15 minutes into the past to match the frontal passage time recorded with the Parsivel²; (c) a PSD time-series for the Parsivel² from 0630 to 0800 UTC. Maximum particle diameter in (b) and (c) is plotted every minute in vertical bins starting at 0, 0.062, 0.187, 0.312, 0.437, 0.562, 0.687, 0.812, 0.937, 1.062, 1.187, 1.375, 1.625, 1.875, 2.125, 2.375, 2.750, 3.250, and 3.750 mm..... 87
35. OSCRE particle sizes during the 45 minutes prior to the frontal passage. Plotted in (a) is a gamma distribution, where the blue bars are the particle number density, the black line is the observed gamma distribution, and the red line is the ideal gamma distribution determined by Pomeroy (1988). Plotted in (b) is a particle size distribution..... 88

36.	As in Fig. 35 except for the 45 minutes after the frontal passage.....	89
37.	Thermodynamic profiles plotted on skew- T log- p diagrams from radiosondes launched at (a) 0500 UTC, (b) 0930 UTC, (c) 1140 UTC, (d) 1500 UTC, (e) 1640 UTC, and (f) 1945 UTC.....	91
38.	(a) A PSD with respect to height for the PASIV; (b) radar reflectivity PPI observed with DOW7 at 0641 UTC at an elevation angle of 1.8°; (c) radar reflectivity RHI observed with DOW7 at 0648 UTC at an azimuthal angle of 27.5° with respect to north; and (d) radar differential reflectivity RHI observed with DOW7 at the same time and angle as (c). In panel (b), the white ‘X’ indicates the locations that the PASIV was launched from, and the dashed black line indicates the scan angle for the radar imagery in panels (c) and (d). Grand Forks, ND and Thompson, ND are indicated by red dots. In panels (c) and (d), the red arrows indicate the approximate distance away from DOW7 that the PASIV was launched. Panel (a) is courtesy of Dr. Sean Waugh at the National Severe Storms Laboratory.....	92
39.	Composite images of hydrometeors from OSCRE for (a) 0500 to 0730 UTC, and (b) within a 200-second window at 0645 UTC coinciding with the PASIV launch. Panel (a) is adapted from Kennedy et al. (2021).....	93
40.	Data from the radiosonde launched with the PASIV plotted on a skew- T log- p diagram. The portion of the profile within the dendritic growth zone is highlighted in the yellow box.....	94
41.	A skew- T log- p showing the thermodynamic profiles from radiosondes launched at 1500 and 1640 UTC. The solid red and blue lines are the respective temperature and dewpoint profiles at 1500 UTC. The dot-dashed maroon and dark blue lines are the respective temperature and dewpoint profiles at 1640 UTC. The black and periwinkle wind barbs are the winds throughout the column at 1500 and 1640 UTC, respectively.....	95
42.	The 0500 UTC observed sounding is overlaid with multiple 00 UTC model soundings 5 model hours out (0500 UTC model time). The observed sounding is compared to (a) the GFS, (b) the NAM, (c) the NAM-3km, (d) the HRRR, and (e) the RAP. In each panel, the solid red and blue lines are the observed temperature and dewpoint profiles, respectively, and the dot-dashed maroon and navy lines are the model temperature and dewpoint profiles, respectively. The black wind barbs are observed winds and the periwinkle wind barbs are model winds.....	96

43.	Panel (a) shows 00 UTC model temperature error at model hour 5 (0500 UTC model time) compared to observed temperatures at 0500 UTC. Panel (b) is the same as (a), except for relative humidity. The thick black line at 0.0 °C in (a) is the respective observed temperature, and the thick black line at 0% in (b) is the respective observed relative humidity. The colored lines are the model error. In both panels, the red line is GFS model error, the yellow line is NAM model error, the green line is NAM-3km model error, the blue line is RAP model error, and the purple line is HRRR model error.....	97
44.	As in Fig. 42, except for 0645 UTC observations versus 00 UTC models at model hour 7 (0700 UTC model time).....	98
45.	As in Fig. 43, except for 0645 UTC observations versus 00 UTC models at model hour 7 (0700 UTC model time).....	99
46.	As in Fig. 42, except for 1140 UTC observations versus 00 UTC models at model hour 12 (1200 UTC model time).....	100
47.	As in Fig. 43, except for 1140 UTC observations versus 00 UTC models at model hour 12 (1200 UTC model time).....	101
48.	As in Fig. 42, except for 1500 UTC observations versus 00 UTC models at model hour 15 (1500 UTC model time).....	102
49.	As in Fig. 43, except for 1500 UTC observations versus 00 UTC models at model hour 15 (1500 UTC model time).....	103
50.	As in Fig. 42, except for 1640 UTC observations versus 00 UTC models at model hour 17 (1700 UTC model time).....	104
51.	As in Fig. 43, except for 1640 UTC observations versus 00 UTC models at model hour 17 (1700 UTC model time).....	105
52.	As in Fig. 42, except for 1945 UTC observations versus 00 UTC models at model hour 20 (2000 UTC model time).....	106
53.	As in Fig. 43, except for 1945 UTC observations versus 00 UTC models at model hour 20 (2000 UTC model time).....	107

LIST OF TABLES

Table		Page
1.	Instrument availability for the 12 Feb 2020 ground blizzard. Times along the x-axis are in UTC. The instruments are listed along the y-axis and are grouped by category: instruments that fell under the in situ or microphysical instrumentation category have a blue filling; instruments that fell under the radar and remote sensing instrumentation category have a red filling; and instruments that fell under the surface-based instrumentation category have a green filling. Filled boxes indicate that the instrument was used at some point during that hour.....	33
2.	A summary of the r_{mean} , α , and β values from Pomeroy (1988), for 45 minutes before the frontal passage, and 45 minutes after the frontal passage.....	90

ACKNOWLEDGMENTS

First, I would like to thank my academic advisor, Dr. Aaron Kennedy for his guidance and support throughout this project. Joining the BLOWN-UNDER project has been an honor; taking part in ground blizzard and blowing snow research in North Dakota has been an amazing learning experience, one that I wouldn't change for the world. I am grateful to Aaron for taking me under his wing, and I am looking forward to working with him on blowing snow research in the future. Additionally, I would like to thank my committee members, Drs. Bruce Lee and Mark Askelson, for sharing their helpful comments, edits, and knowledge during the writing of this thesis.

Next, I would like to thank Dr. Sean Waugh at the National Severe Storms Laboratory for building a PASIV for our project and for helping us post-process the data. I also thank Stephen P. Palm with NASA Goddard Space Flight Center for his help in processing *CALIPSO* CALIOP data. Thanks are extended to the Center for Severe Weather Research for loaning DOW7 for our project, and to Aly Gilliland for operating DOW7 for us throughout the intensive operation period of the campaign. Additionally, I thank the NSF AGS for funding BLOWN-UNDER, which allowed for the presented research to come to fruition.

Finally, I would like to thank my family and friends. I thank my family for their love and support over the years, and for their trust in what I was doing in when I moved from New York to North Dakota in 2019 to advance my career in grad school. I thank the tight-knit community of atmospheric science grad students at UND for their help and collaboration, and for being great friends to create memories with. I would not have gotten this far without the support of my family and friends, and I am grateful for each and every one of them.

ABSTRACT

Blowing snow and blizzards are wintertime hazards that greatly affect society in the Red River Valley (“RRV”) located between eastern North Dakota and northwestern Minnesota. With poor visibility, snow drifts, and dangerous wind chills, these events can cripple communities as transportation is brought to a standstill. While the underlying mechanisms for blowing snow and ground blizzard initiation are generally understood, there are still many unknowns, including how lofted and blowing snow in horizontal convective rolls affect the thermodynamics and evolution of the atmospheric boundary layer. In the winter of 2019-2020, a research campaign called Blowing Snow Observations at the University of North Dakota: Education through Research (BLOWN-UNDER) was conducted to investigate and better understand the thermodynamics, macrophysics, and microphysics in blowing snow events. The “homerun” event was the 12 February 2020 ground blizzard, which is the focus of this study. Instrumentation used to collect data during the event can be categorized into three main categories: surface in situ, balloon-borne and microphysical, and radar and remote-sensing. This suite of instrumentation allowed for the most comprehensive observations of a ground blizzard ever collected in the RRV. Imagery from a snowflake camera are processed to determine crystal habit and particle size distributions, whose statistics are then used to evaluate the performance of a laser disdrometer. Radar and laser ceilometer data are analyzed to investigate the macrophysics of blowing snow plumes and are used in conjunction with radiosonde data to diagnose boundary layer evolution throughout the blizzard. Lastly, individual instrument analysis is conducted to develop a thorough study of the blizzard’s meteorology as well as assess which instruments are best suited for future blizzard data collection.

Results of this study suggest that radar, satellites, radiosondes, and hydrometeor imaging instrumentation are useful for investigating blowing snow and blizzards, whereas lidar and laser disdrometer instrumentation have some limitations in these conditions.

CHAPTER 1

INTRODUCTION

1.1. Blowing Snow and Blizzards

1.1.1. Properties of Blowing Snow

Blowing snow acts as a mode of snow transport, which also includes drifting snow (Mahesh et al. 2003; Gossart et al. 2017). Although blowing and drifting snow are similar in this respect they are differentiated by the height of the snow transport, with drifting snow being constrained to near the ground at heights less than 2 meters (Gossart et al. 2017), and blowing snow reaching heights of at least eye-level (Li and Pomeroy 1997) but potentially extending hundreds of meters into the atmosphere (Gossart et al. 2017; Palm et al. 2011, 2017, 2018). Blowing snow can occur with snow that is falling or that has already fallen and is lofted by winds blowing over the surface. The particles that comprise surface-based blowing snow are generally small, irregularly shaped, and comprised of shattered snowflakes (Fig. 1) whose sizes follow a gamma distribution (Budd 1966, Schmidt et al. 1982, Pomeroy 1988, Déry et al. 1998). Per Pomeroy (1988), the gamma distribution function with respect to hydrometeor equivalent radii is as follows:

$$f(r) = \frac{r^{\alpha-1} \beta^{-\alpha} e^{-\frac{r}{\beta}}}{\Gamma(\alpha)} \quad (1.1)$$

where r is the hydrometeor radius, α is a dimensionless shape parameter, β is the scale parameter (r_{mean} / α , where r_{mean} is the mean hydrometeor radius of the dataset), and $\Gamma(\alpha)$ is the gamma function, equal to $(\alpha - 1)!$. Pomeroy (1988) suggests common values for a blowing snow saltation layer to be $\alpha = 5$, $r_{mean} = 100 \mu\text{m} = 0.1 \text{ mm}$, yielding $\beta = 0.02 \text{ mm}$ and $\Gamma(\alpha) = (5 - 1)! = 24$.

Various factors must be considered when determining the possibility of surface-based blowing snow. A strong force must be applied to the surface to break cohesive bonds of crystals

in a snowpack (Schmidt 1980), with the cohesion of the surface determining the threshold wind speed needed to break those bonds and loft particles (Schmidt 1982). Based on observations from the Byrd Snowdrift Project in Antarctica, Budd et al. (1966) found that a 1-meter wind speed of at least 14 m s^{-1} is necessary to overcome snowpack resistance, with actual wind speeds varying based on snow-particle bonding, cohesion, and kinetic properties. Temperature, equivalent water content, and age of a snowpack all factor into the threshold needed to be surpassed to dislodge snow from the surface and loft it into the atmosphere (Li and Pomeroy 1997).

Li and Pomeroy (1997) identified three different snow cohesive regimes that have different effects on the initiation of snow transport in the prairies of western Canada: a wet cohesive regime, a warm cohesive regime, and a cold cohesive regime. The wet cohesive regime is governed by the amount of snowmelt water within the snowpack and is most important at temperatures near freezing. The liquid water acts to melt the snowpack and increase the strength of the cohesive bonds between particles. The warm cohesive regime is indicated by a thicker quasi-liquid layer at the surface of the snowpack, whereas a cold cohesive regime is indicated by a thinner quasi-liquid layer at the surface of the snowpack. The equivalent water content of the snow also determines the strength of the cohesive bonds. Dry snow (snow with a low equivalent water content) is generally incapable of developing strong cohesive bonds, making it easier for wind to dislodge the snow from the snowpack and loft it. Wet snow (snow with a higher equivalent water content) is better able to develop strong cohesive bonds, making it more difficult for wind to dislodge the snow from the snowpack. Per Li and Pomeroy's (1997) findings, the 10-meter wind threshold to dislodge and loft wet snow is 7 to 14 m s^{-1} with an average of 9.9 m s^{-1} , and for dry snow is 4 to 11 m s^{-1} with an average of 7.7 m s^{-1} . Lastly, the age of the snowpack has an effect on the wind threshold. As time progresses, the snow within a snowpack will compact under its own weight, increasing

density and strengthening cohesive bonds. On average, it takes at least another 0.5 m s^{-1} on top of the above thresholds to break the bonds to dislodge and loft snow.

1.1.2. Types of Blizzards

Per the United States National Weather Service, blizzards are defined as storms with winds sustained or frequently gusting to 35 mph (16 m s^{-1}) or more, coupled with falling and/or blowing snow to reduce visibilities to 0.25 miles (400 m) or less for at least three hours (NWS 2021). Blizzards and blizzard conditions can develop from a variety of meteorological systems, including Colorado Lows and Alberta Clippers in the Central and Northern Plains (Kennedy et al. 2019), mid-latitude cyclones and Nor'easters along the east coast and into New England such as the “Storm of the Century” in 1993 (Kocin et al. 1995), and on occasion within lake-effect bands off of the Great Lakes (Niziol 1987).

While many believe blizzards must be associated with falling snow, blizzards can also occur due to strong winds lofting fallen snow from the ground. These types of blizzards are called ‘ground blizzards’ and are common wintertime threats for the Northern Plains (Kapela et al. 1995; Stewart et al. 1995; Kennedy et al. 2019). A well-known example of a ground blizzard is the Blizzard of '77 in western New York that lasted from 28 to 30 January 1977. Winds gusting more than 31 m s^{-1} (70 mph) lofted over $25,000 \text{ km}^2$ (over $9,652 \text{ mi}^2$) of powdery snow off of the frozen surface of Lake Erie and blew it into the suburbs of Buffalo, New York, effectively paralyzing the region (Rossi 1999; Call 2005).

Between 1979 and 2017, around one-quarter of all blizzards in the Red River Valley (“RRV”) were ground blizzards initiated by Arctic Fronts (Kennedy et al. 2019). As will be discussed in later chapters, the 12 February 2020 RRV ground blizzard falls into this category.

Further discussion of the RRV blizzard climatology is provided in Section 1.2.

1.1.3. Impacts and Hazards of Blowing Snow and Blizzards

Blowing snow and blizzards pose multiple threats to society. The most obvious is reduced visibility due to the increased extinction of visible light in blowing snow events (Pomeroy and Male 1988), often bringing transportation to a halt with dangerous to impossible driving conditions and leaving drivers stranded on the road in their vehicles (Rooney 1967; Hershey and Osborne 2008). This can slow or even halt the local economy, resulting in millions of dollars of lost work hours and retail sales (Burrows et al. 1979). Redistribution of snow via wind transport can also affect local agriculture and vegetation by taking away snow from a location and relocating it elsewhere, thereby affecting the potential amount of liquid water from springtime snowmelt (Keller et al. 2000; Jones et al. 2001; Hershey and Osborne 2008; Grünewald et al. 2010).

Beyond societal impacts, blowing snow and blizzards pose impacts to the environment. Snow that is lofted from the surface and into an unsaturated atmosphere (relative humidity less than 100%) is subject to sublimation (Schmidt 1972; Mann et al. 2000). Blowing snow can also affect the surface mass balance of water which can happen when snow is removed from the surface and redeposited elsewhere, or completely lost via sublimation in an unsaturated atmosphere (Thiery et al. 2012). In the mid- and high-latitudes of North America, where approximately 10 to 50% of snowpack is returned to the atmosphere via sublimation (Pomeroy and Essery 1999), this has impacts on local hydrology such as the timing and magnitude of snowmelt runoff (Luce et al. 1998, Grünewald et al. 2010), which in turn has an effect on infiltration and stream discharge (Pomeroy et al. 1997).

For locations such as Antarctica, blowing snow and sublimation can have drastic impacts

on surface mass balance, affecting the ice sheets, particularly over coastal Antarctica where blowing snow sublimation can reduce the snowpack (Gossart et al. 2017). The removal of this snow can lead to areas of blue ice that have a lower albedo than snow, allowing for more insolation to be absorbed at the surface, in turn decreasing stability of ice shelves (Bintanja et al. 1995; Lenaerts et al. 2016). If these ice shelves collapse, it can have significant impacts on sea level rise (Rignot et al. 2011).

Blowing snow also impacts the thermodynamics of the lower atmosphere, particularly the planetary boundary layer. From numerical modelling studies, it is generally accepted that sublimation will cool the blowing snow layer down to the frostpoint, allowing the layer to become saturated and, in turn, limit further sublimation (Mann et al. 2000; Bintanja 2001a). Observations outside of the drifting snow layer to support this theory were not collected until Palm et al. (2018) used dropsondes and the Cloud-Aerosol Lidar and Infrared Pathfinder Satellite Observation (*CALIPSO*) satellite to observe the thermodynamic structure of blowing snow layers over Antarctica. Before blowing snow initiation, a strong inversion typically exists in the lowest few hundred meters of the atmosphere due to radiative cooling, with stronger inversions occurring with lighter wind speeds. Once blowing snow initiates, surface temperatures increase and the environmental lapse rate within the blowing snow layer becomes, on average, between dry and moist adiabatic. Mixing and entrainment due to wind-shear-induced turbulence at the top of the blowing snow layer causes drier, warmer air from above the inversion to be mixed into the boundary layer, warming and drying the upper boundary layer. This creates a relative humidity profile with respect to ice such that the atmosphere is closest to saturation near the surface with relative humidity decreasing with height. These results suggest mixing is as important as sublimation with regards to the evolution of the boundary layer during blowing snow events.

1.2. Winter in the Red River Valley

The RRV located between North Dakota and Minnesota is a flat area that is a result of carving from glacial retreat during the most recent ice age and was once home to Glacial Lake Agassiz (Johnson 1962). In the center of the valley is the Red River of the North, a northward flowing river that extends from the United States into Canada. Within the U.S., the valley has a latitude of 45-49°N and is located near the geographical center of North America. Due to its distance away from any large bodies of water and mountain ranges, the valley is vulnerable to extreme cold and a variety of winter weather hazards. Per NCEI (2021) climatological data from 1991-2020, the region typically receives approximately 114.3-127 cm (45-50 inches) of snow per year. Normal wintertime (December-January-February) daily temperatures within the valley range from -13.4 °C (7.9 °F) in the north to -10.7 °C (12.8 °F) in the south.

Blowing snow and blizzards are a common hazard in the RRV. Schwartz and Schmidlin (2002) and Coleman and Schwartz (2017) produced a climatology of blizzards and determined this region is the most common place to see blizzards in the contiguous United States (Fig. 2). Kennedy et al. (2019) provided additional meteorological details to this climatology for the Fargo/Grand Forks National Weather Service Forecast Office (NWSFO) county warning area (CWA). Between the winters of 1979-80 and 2017-18, an average of 2.6 blizzards occur per year within the valley, with a range of 0 to 10 blizzards per season.

Blizzards in the RRV are most commonly initiated from synoptic-scale, snow-producing systems that boast strong winds produced by tight pressure gradients. The Fargo/Grand Forks NWSFO recognizes four different types of systems that initiate blizzards in the valley: Colorado Lows, Alberta Clippers, Arctic Fronts, and Hybrids (Kennedy et al. 2019). Colorado Lows form due to lee cyclogenesis off the Rocky Mountains near eastern Colorado and generally produce the

greatest amount of precipitation due to the northward advection of moisture originating from the Gulf of Mexico. Alberta Clippers form similarly east of the Rockies in Alberta, Canada and generally propagate quickly to the southeast. Their quick propagation and reduced moisture content typically results in minimal snowfall. With both Colorado Lows and Alberta Clippers, significant blizzard-criteria-satisfying winds can be realized. Hybrid systems are similar to both of the prior systems, except they form anywhere geographically between Colorado and Alberta. Arctic Fronts are strong cold fronts that pack bitterly cold temperatures and high winds behind the frontal boundary. The high winds with these fronts are typically strong enough to dislodge already fallen snow from the surface and loft it into the atmosphere. If enough snow is lofted, blowing snow and ground blizzard conditions can be realized on an otherwise clear day.

1.2.1. Blowing Snow Plumes in the Red River Valley

The RRV is a few hundred meters deep across a width of approximately 100 kilometers. Although rather shallow, there are numerous cases where blizzard conditions are only found within blowing snow plumes in the RRV (e.g., Fig. 2 of Kennedy et al. 2019). Significant visibility reductions are often confined to features that resemble horizontal convective rolls (HCRs) on satellite and radar (Kennedy et al. 2020). Outside of blowing snow plumes, clear skies prevail, notwithstanding cloud cover.

HCRs are a common form of boundary layer convection where long, counter-rotating rolls create areas of rising and sinking motions (Fig. 3) with rows of clouds forming along the rising branches of the rolls, creating cloud streets nearly parallel to the mean wind in the boundary layer (LeMone 1973; Brown 1980; Weckwerth et al. 1997, 1999). A variety of conditions exist that may produce HCRs. Dynamic instabilities such as parallel instability (Lilly 1966; Brown 1980;

Stensrud and Shirer 1988) and inflection point instability (Faller 1965; Brown 1980; Stensrud and Shirer 1988) both can initiate HCRs, in addition to thermal instability in the presence of wind shear (Asai 1971; Weckwerth et al. 1999). HCRs are not always immediately evident since not all HCRs produce clouds, fog, or haze (Weckwerth et al. 1997). The presence of HCRs has been inferred before by the linear flight pattern of seagulls (Woodcock 1942), through the vertical velocity perturbations of low-level aircraft flights (Grossman 1982), and through the lofting of blowing snow into plumes (Kennedy et al. 2019, 2020).

1.3. Previous Blowing Snow Research

The properties and impacts of blowing snow have been investigated in various parts of the world, with particular interest in high-latitude locations such as Antarctica (e.g. Bintanja 2001b; Mahesh et al. 2003; Palm et al. 2011, 2017, 2018; Yang et al. 2014; Gossart et al. 2017; Loeb and Kennedy 2021) and Canada (e.g. Li and Pomeroy 1997; Savelyev et al. 2006; Bourdages et al. 2009; Gordon and Taylor 2009; Gordon et al. 2009). Several studies are described herein. The results from these various studies, including the advantages and disadvantages of various instrumentation in observing blowing snow, proves useful for present and future blowing snow research in other parts of the world, such as the mid-latitudes of North America where research and literature are lacking.

1.3.1. Surface-Based Remote-Sensing Research

Surface-based remote-sensing instrumentation is a popular option when observing blowing snow since this instrumentation does not have to struggle with penetrating optically-thick clouds to view blowing snow (e.g., satellites), or determining the difference between clouds and a snow-

covered surface that have similar physical and radiative properties (Yamanouchi et al. 1987, Mahesh et al. 2003). In recent decades, ceilometers and lidars have been used extensively in Antarctica for blowing snow research. Mahesh et al. (2003) used data from a micropulse lidar located approximately 10 meters above the surface at the South Pole Station in Antarctica to investigate blowing snow events between 1999 and 2002. Two limitations with using lidar to investigate blowing snow were discussed: 1) the lidar used has a vertical resolution of only 30 m; 2) all lidar have a near-range signal limitation called the overlap function where the scattered signal is not yet fully focused at the detector, making observations difficult in the lowest 100 meters. Out of 40 cases, the blowing snow layer had an average height of 416 meters, with about 50% of the layers measuring less than 200 meters, and nearly all layers measuring less than 600 meters. No correlation was found between wind speed and the depth of a blowing snow layer. It is thought that once snow is lofted and suspended in the atmosphere, a weaker wind speed is needed to keep the snow suspended, thus when winds fall below the threshold to dislodge and loft snow from the surface, the winds may still be strong enough to keep snow suspended.

Gossart et al. (2017) used ground-based ceilometers to collect data at the Neumayer III (2011-2015) and Princess Elisabeth (2010-2016) research stations in East Antarctica to investigate blowing snow. A blowing snow detection algorithm was developed for the ceilometers, capable of detecting blowing snow layers that reach at least 30 meters in height. Compared to human observations, the algorithm agreed 78% of the time, with heavy blowing snow being observed at the Neumayer station 36% of the time, and 13% of the time at Princess Elisabeth. The algorithm was capable of detecting blowing snow for both clear and cloudy/precipitating scenes.

Loeb and Kennedy (2021) built on the work of Gossart et al. (2017) by enhancing their blowing snow detection algorithm by including meteorological thresholds such as wind speed,

visibility, and relative humidity, and by reducing time averaging from one-hour to five-minute periods. The updated algorithm was applied to data from the Atmospheric Radiation Measurement (ARM) West Antarctic Radiation Experiment (AWARE) field campaign in 2016, which was then compared to human observations collected at the McMurdo Station in eastern Antarctica. Incorporating these changes increased agreement between the algorithm and human observations, particularly in the spring and summer months (October through February). Although the algorithm performed better than the original algorithm developed by Gossart et al. (2017), it struggled with intense events with falling precipitation in the fall and winter (April, June through September). The authors emphasized that owing to a lack of ground truth (microphysical observations throughout the boundary layer), it was impossible to determine how accurate the algorithm was.

Beyond lidar and ceilometers, radar has been another key instrument for studying blowing snow and the forcing behind such events. Vertical-pointing radars such as the Ka-Band ARM Zenith Radar (KAZR; Loeb and Kennedy 2021) in Antarctica and the Micro Rain Radar (MRR; Walter et al. 2020) in the Gotschnagrat mountain range near Davos-Klosters, Switzerland have been used to investigate blowing snow, particularly for measuring intensity in the vertical, and for measuring the horizontal behavior of blowing snow at different wind speeds (Walter et al. [2020] turned their radar 90° into the horizontal to scan blowing snow plumes). Traditional weather radars are also useful for observing blowing snow. Kennedy and Jones (2020) used the Weather Surveillance Radar 88-Doppler (WSR-88D) radar in Mayville, North Dakota (KMVX) in their investigation of blowing snow plumes during the 24 Feb 2019 ground blizzard in eastern North Dakota and northwestern and west-central Minnesota. It was shown that the radar can be used to detect changes and differences in plume spacing, width, and length with time. One key drawback of longer wavelength radars such as KMVX is that blowing snow plumes can be below the

sensitivity of the radar, making blowing snow undetectable. Further, detection is limited to close to the radar where the beam height is sufficiently low.

Radar observations have not only been collected from the surface. Two-dimensional cross-section radar scans of atmospheric phenomena, such as those made with the Wyoming Cloud Radar (WCR) during the International H₂O Project (IHOP; Weckwerth et al. 2004), can reveal complex features. The WCR is a 95-GHz (3-mm) Doppler radar (Pazmany et al. 1994) that was installed on the university of Wyoming King Air aircraft during IHOP (Geerts et al. 2006). Geerts et al. (2006) investigated the vertical structure of a cold front over the Texas panhandle observed during campaign and showed that behind a well-defined and frontogenetic cold front existed intense turbulence indicative of a density current with Kelvin-Helmholtz billows (see Fig. 8c and 8d from their study). The same radar and aircraft were used later by Geerts et al. (2015) to study blowing snow in the Rocky Mountains of Wyoming and Colorado. The results from their study suggested that blowing snow and ice particles may be able to seed supercooled orographic clouds, enhancing snow growth and snowfall.

1.3.2. Satellite-Based Research

Although satellite remote sensing of blowing snow plumes can be difficult or impossible at times due to cloud cover, when clouds are absent, satellites are a powerful tool for investigating and observing blowing snow. Palm et al. (2011) used satellite lidar data from the Cloud-Aerosol Lidar with Orthogonal Polarization (CALIOP) aboard the *CALIPSO* satellite to investigate blowing snow properties in events between 2007 and 2009. Blowing snow was present as much as 70% of the time in the wintertime in portions of Antarctica with a thickness of 30 meters to 1000 meters and an average of 120 meters. Layer optical depth ranged between 0.05 and 1.00 with

an average of 0.20. Palm et al. (2017) combined blowing snow fields from *CALIPSO* with the meteorological fields from the Modern-Era Retrospective analysis for Research and Applications, v2 (MERRA-2) reanalysis package (Gelaro et al. 2017) to calculate blowing snow sublimation and transport rates over Antarctica between 2006 and 2016. Results from this study showed that sublimation occurs most often within 200 kilometers of the coast with sublimation exceeding 250 ± 125 millimeters of snow water equivalent per year even though blowing snow occurs more often further inland. This is due in part that the air near the coast is warmer and less humid than in the interior.

Due to the limited overpasses of polar-orbiting satellites such as *CALIPSO*, polar-orbiting observations occur less frequently at lower latitudes. Kennedy and Jones (2020) observed blowing snow in HCRs during the 24 Feb 2019 RRV ground blizzard using data from the Geostationary Operational Environmental Satellite-16 (*GOES-16*). The Advanced Baseline Imager (ABI; Schmit et al. 2017, 2018) on board *GOES-16* allowed for the viewing of blowing snow events. Blowing snow was identified based on near-infrared reflectance, making the process visible only during the day. The “Day Snow-Fog” composite – consisting of the 0.86-, 1.6-, 3.9-, and 10.3-micron wavelength bands – with gamma and clip setting modifications to follow solar zenith angle changes provided the most utility. The usage of *GOES-16* in forecasting and nowcasting blowing snow and blizzards has proven powerful in the operational setting. At the Fargo/Grand Forks NWSFO, *GOES-16* is used in conjunction with radar, automated and human surface reports of visibility, roadside cameras, and snowplow cameras to validate areas of blowing snow and refine wintertime products to smaller, more representative areas. Despite the increased situational awareness, there are limiting factors while using *GOES-16*: 1) there are times when the pixel resolution on *GOES-16* is too coarse to identify smaller blowing snow features that other higher-

resolution satellites can identify; 2) the connection between near-infrared products and surface visibility is still unknown, and it is unknown if other channels observe blowing snow better than those that make up the “Day Snow-Fog” composite; 3) due to the near-infrared nature of the channels used, blowing snow observations can only be derived during daylight hours when skies are clear or clouds are optically thin, making *GOES-16* most useful for ground blizzards.

1.3.3. In Situ Research

Other research has included the usage of in situ instrumentation such as dropsondes (such as with Palm et al. (2018); results of this study were discussed in section 1.1.3), disdrometers, and hydrometeor imagers. These avenues have not been utilized much since the harsh and complex environments that blowing snow exists in are also environments that make it difficult for collecting in situ observations, particularly by weather balloon.

Loeb and Kennedy (2021), in addition to investigating lidar data, also used Particle Size and Velocity (Parsivel²) disdrometer data (Löffler-Mang and Joss 2000) to investigate particle size distributions (PSDs) of fog, blowing snow under clear skies, blowing snow with some clouds and/or precipitation, and events with an intense mixture of blowing snow and precipitation. Overall, there was no distinction found between each type of event and their respective PSDs. Further, when PSDs are separated by wind speed, it was found that the number of particles detected that were greater than 1 mm in diameter had a marked increase with winds beyond 10 m s⁻¹ at the expense of the number of particles smaller than 0.5 mm. The authors hypothesized that a fundamental limitation may exist where at higher wind speeds, several small particles may create voltage signals indicative of singular larger particles with a greater diameter than reality.

Camera technology has proven to be a critical tool when studying the microphysics of

falling and blowing snow. Gordon and Taylor (2009) used a custom camera system in Churchill, Manitoba, Canada to study the particle shape, size distribution, velocity, and number flux of blowing snow. The camera works in a way where hydrometeors are blown into a slot where a halogen lamp illuminates the hydrometeors. A camera takes a picture of the shadow cast by the hydrometeors. They found that the average ratio of the longest particle axis to the perpendicular axis to be 1.41 with particle size distributions conforming to gamma distribution with an average shape parameter of $\alpha = 1.9$. Particle velocity measurements were found to not be accurate with the camera. The same camera system was used by Gordon et al. (2009) in Franklin Bay, Northwest Territories, Canada, except with a different lens to enlarge the viewing area. They studied the mass and number density profiles and the saltation height of blowing snow (the maximum height snow dislodged from the surface achieves before being transported back to the surface; above this height, the wind is strong enough to fully suspend the snow into the atmosphere). It was found that the average saltation layer ranges from 1 to 10 mm and is dependent on temperature and relative humidity, which affects snow particle bonding strength. There was no correlation between snowpack age and the average saltation layer height. With the help of a particle counter, they determined that particle fall velocity and particle size increases with increased wind speed with a slight plateau in particle sizes for a frictional velocity of 0.4 m s^{-1} .

More recently, blowing snow observations have been collected by Schaer et al. (2020) with the Multi-Angle Snowflake Camera (MASC; Garrett et al. 2012) at the Dumont d'Urville station in Antarctica in 2015 and 2017, and in Davos, Switzerland from 2015-2016. The instrument consists of three high-resolution cameras angled 36° from each other, all attached to a ring structure. As hydrometeors fall through the ring structure, they trip a near-infrared emitter-receiver array that activates the cameras to take a picture of the hydrometeors from the three angles. It was

found that of the images taken at Dumont d'Urville, about 75% contained blowing snow. Blowing snow was most often observed just after the start of precipitation, highlighting the importance of fresh snow for the process. Similar results were obtained at the Davos site.

An affordable, surface-based snowflake imager called the Open Snowflake Camera for Research and Education (OSCRE) was developed by Dr. Aaron Kennedy to investigate blowing snow properties in the RRV. Emphasis during development was affordability and reproducibility to make such observations more accessible since traditional imaging instruments are often very expensive due to complexity and infrequency of production (Kennedy et al. 2021). OSCRE specifications and the data collected with the instrument are discussed throughout this manuscript.

1.4. Introduction to BLOWN-UNDER

The Blowing Snow Observations at the University of North Dakota: Education through Research (BLOWN-UNDER) field campaign was conducted during the winter of 2019-2020 to collect macro- and microphysical measurements in the harsh winter conditions of eastern North Dakota (Kennedy et al. 2021). The primary goal of the campaign was to determine optimal and affordable strategies of observing blowing snow to better understand the dynamics and evolution of blizzard events. This campaign was student-led and met a variety of outreach, educational, and scientific objectives. The OSCRE was tested extensively during this campaign.

Observations of a wide variety of hydrometeor types, including falling and blowing hydrometeors, were collected between October 2019 and April 2020, with particular emphasis on the campaign's intensive operation period (IOP) from 20 January to 10 February 2020. This IOP period coincided with educational outreach involving the Center for Severe Weather Research (CSWR) Doppler on Wheels (DOW7; Wurman et al. 1997). The IOP period featured anomalously

quiet conditions for North Dakota. However, with permission from CSWR to keep DOW7 in town for a few extra days, the “homerun” event – IOP-3 on 12 February 2020 – ended the campaign on a high note with extensive data collection across several instrumental platforms in a classic ground blizzard (instrumentation are discussed further in Chapter 2). The data collected are used to describe and discuss the macro- and microphysical features of blowing snow throughout this thesis.

1.5. Objectives

Although blowing snow and blizzards are a common threat to the RRV in the wintertime, the way the boundary layer evolves in these events is still not understood. It is evident from past blowing snow research that sublimation and mixing in the boundary layer play important roles in the evolution of the boundary layer during blowing snow events. However, numerical weather models struggle with these processes since a lack of surface and boundary layer thermodynamic and microphysical data prevents the validation and improvement of blowing snow parameterizations. Thus, while the mechanisms responsible for blowing snow and blizzard initiation are known, it is still difficult to predict the intensity and impacts of these events.

The wide variety of instrumentation used and the data collected during BLOWN-UNDER can help develop solutions for these problems. With new methods of data collection explored during the campaign, affordable ways to collect widespread data may be realized where data assimilation into models can become an actualization, in turn allowing for more accurate and fine-tuned blowing snow and blizzard forecasting.

In short, this study will provide the most thorough and comprehensive analysis of a RRV ground blizzard ever. The results of this study will enhance understanding of the thermodynamic

and kinematic processes involving blowing snow and ground blizzards in the valley, help the navigation of future blowing snow research in the valley and elsewhere, and aid in operational forecasting.

The objectives of this study are as follows:

- 1) Analyze data collected using new and existing instrumentation during the 12 Feb 2020 RRV ground blizzard to develop a case study for the event. The thermodynamic and macro- and microphysical evolution of the event are investigated to determine the relationship to blowing snow and plume evolution within the RRV.
- 2) Data collected are assessed to determine the efficacy of instrument usage in future blowing snow research. In other words, instrumentation are scrutinized to see how well they performed for this ground blizzard event.



Figure 1 – An image of blowing snow captured with the OSCRE during the 12 February 2020 RRV ground blizzard.

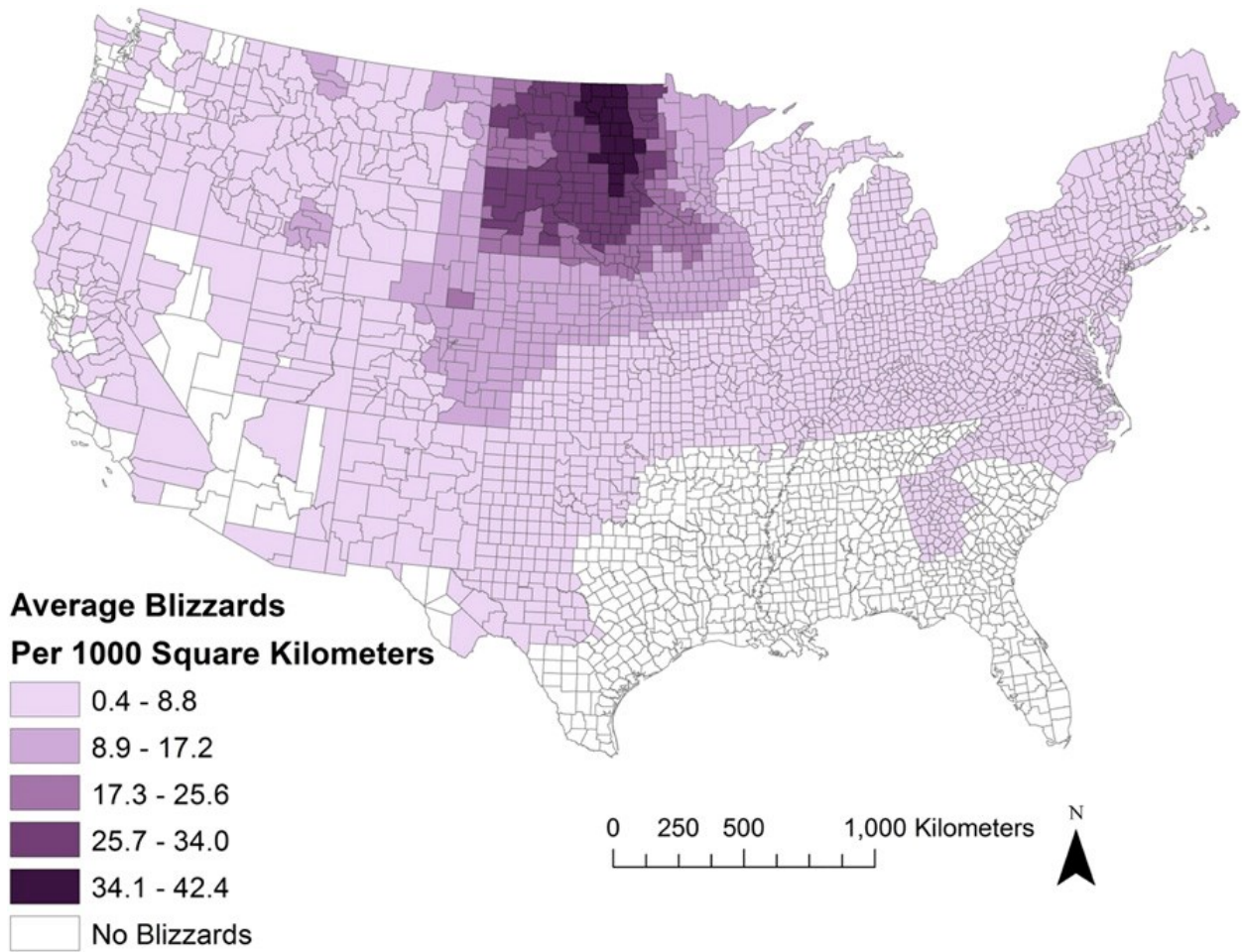


Figure 2 – Average number of blizzards per 1000 km² for the 1959-60 through 2013-14 winter seasons. Darker filling indicates more blizzards per 1000 square kilometers. Adapted from Coleman and Schwartz (2017).

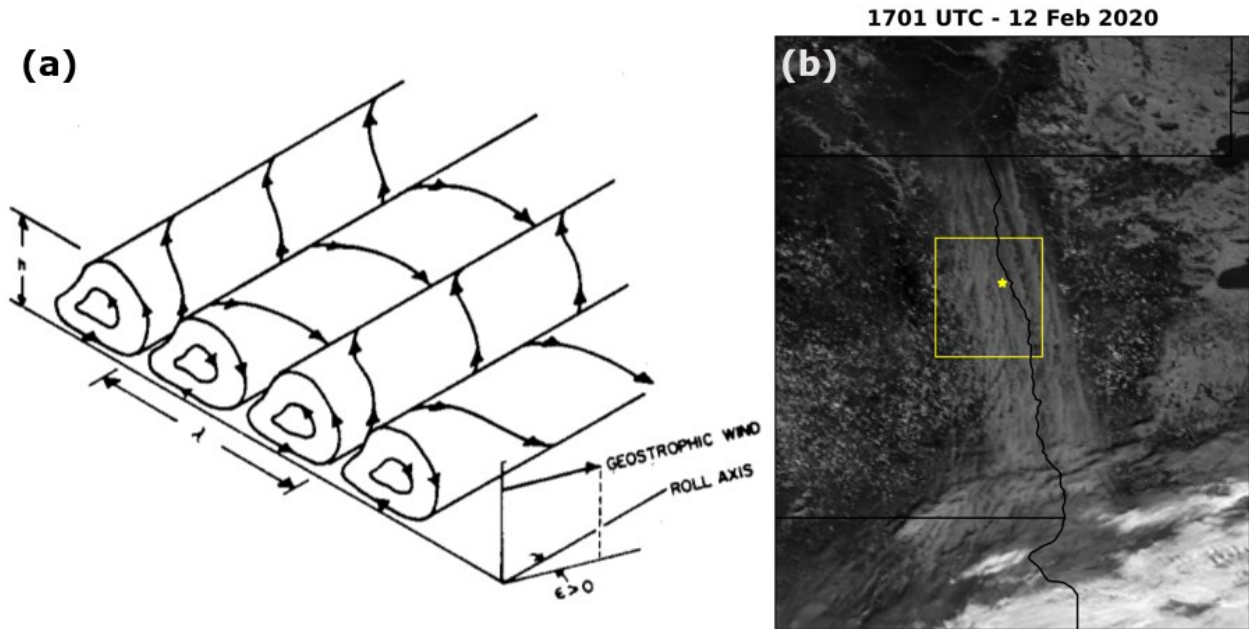


Figure 3 – (a) A schematic of horizontal convective rolls. Arrows indicate how winds are flowing around and within the rolls, h is the height of the rolls, λ is the distance between rising branches (the wavelength of the HCRs), and ϵ is the angle between the roll axis and the mean boundary layer geostrophic wind. Adapted from Weckwerth et al. (1997). (b) An image from the 1.63- μm channel on *GOES-16* during the 12 Feb 2020 ground blizzard. The yellow box is the domain used in Fig. 4. The yellow star marks the location of Grand Forks, ND.

CHAPTER 2

DATA COLLECTION AND METHODOLOGY

2.1. Instrumentation

Instrumentation used throughout BLOWN-UNDER and during the 12 Feb 2020 ground blizzard can be categorized into three categories: 1) surface in situ instrumentation, including instrumentation for microphysics and hydrometeor imaging; 2) balloon-borne in situ instrumentation; and 3) remote-sensing instrumentation. A timetable of instrument availability for the event is provided in Table 1. Locations of the available instrumentation and surface stations can be viewed in Fig. 4.

2.1.1. Surface In Situ Instrumentation

Surface-based instrumentation includes instruments designed to collect campaign-specific and other regional observations at or just above the surface such as standard meteorological data, microphysical data, and hydrometeor imagery. Regional surface observations are provided by the National Oceanic and Atmospheric Administration (NOAA) Automated Surface Observing Systems (ASOS) network (NOAA ASOS 2021) and the North Dakota Agricultural Weather Network (NDAWN; NDSU 2021). Both networks measure surface temperature, dewpoint, wind speed and direction, pressure, and precipitation measurements, while the ASOS network also provides visibility measurements. Sites of specific interest to the BLOWN-UNDER domain include the ASOS stations at Grand Forks International Airport (KGFK) and Grand Forks Air Force Base (KRDR). In addition, a temporary NDAWN mesonet station was deployed at the Oakville Prairie Observatory approximately 21 km (~13 miles) west of Grand Forks, just outside of Emerado, North Dakota. This temporary NDAWN station (hereafter, ‘UND NDAWN’)

collected temperature, dewpoint, and pressure data 2 meters above ground level (AGL), and wind speed and direction and solar radiation data 3 meters AGL, all at 1-minute resolution. The station also featured a webcam to allow remote viewing of the surrounding environment. UND NDAWN was additionally collocated with a Parsivel² laser disdrometer and a Lufft CHM-15K ceilometer. An image of UND NDAWN is provided in Fig. 5a.

DOW7 was deployed with an on-board surface meteorological station that collected temperature, dewpoint, and pressure data at 2 meters above ground level and wind speed and direction 10 meters AGL. For the 12 Feb 2020 event, DOW7 was stationed near Thompson, North Dakota. An image of DOW7 is provided in Fig. 5b.

Microphysics and hydrometeor imaging instrumentation includes instruments that are capable of measuring hydrometeor sizes, or instruments that capture images of hydrometeors that can be post-processed to measure and categorize hydrometeors. Two such instruments were operational on 12 Feb 2020: an OTT Parsivel², and the OSCRE.

The Parsivel² is a laser disdrometer that is capable of measuring particle size distributions of hydrometeors (Löffler-Mang 2000; Tokay et al. 2014). This instrument casts a sheet of light from a transmitter to a receiver that measures a voltage. When hydrometeors fall through the light sheet, the signal is decreased through extinction. The reduction in measured voltage is converted to a particle diameter, and how long the signal is disrupted provides an estimate of the particle fall velocity (Löffler-Mang 2000). The Parsivel² was collocated with UND NDAWN, as seen in the background of Fig. 5a.

The OSCRE is a surface-based hydrometeor imager consisting of a high-resolution camera, an LED strobe light, and a computing platform to control the camera and light, all mounted to a wood frame (Fig. 6). The LED strobe light illuminates hydrometeors in the field of view at speeds

of $\sim 10 \mu\text{s}$, fast enough to limit blurring due to wind (Kennedy et al. 2021). During the 12 Feb 2020 event, images of falling and blowing hydrometeors were taken at 30 fps at a distance of 0.8 m, resulting in a field of view of $54.5 \times 41.5 \text{ mm}$ with $27 \mu\text{m}$ pixels, effectively allowing for hydrometeors with radii as small as $54 \mu\text{m}$ to be resolved.

2.1.2. Balloon-borne In Situ Instrumentation

Balloon-borne in situ instrumentation includes those that were deployed via weather balloon to collect data as the balloon ascends through the atmosphere. Thermodynamic profiles of the atmosphere were collected using GRAW DFM-09 radiosondes, capable of observing temperature, dewpoint, pressure, and wind speed and direction.

In addition to radiosondes, the Particle Size, Imaging, and Velocity probe (PASIV; Waugh et al. 2015) was used experimentally during BLOWN-UNDER. The PASIV is designed to ascend through the atmosphere to measure hydrometeor size and shape, allowing for the creation of a particle size distribution in a profile of the atmosphere. The PASIV used during BLOWN-UNDER was an upgraded version of the first generation of the instrument, featuring a sample volume of $29 \times 20 \times 11.5 \text{ cm}$ capable of resolving hydrometeors more than $100 \mu\text{m}$ in diameter at a rate of about 20 frames per second (Kennedy et al. 2021). Waugh et al. (2015) used the first generation of the instrument to observe portions of severe thunderstorms throughout the entire troposphere deemed too dangerous to observe via traditional means. The incorporation of the PASIV into BLOWN-UNDER was experimental in it being the first time the instrument was deployed for winter weather research. During BLOWN-UNDER deployments, the PASIV was launched with an attached SPOT GPS to aid in instrument retrieval, as well as a radiosonde that would aid in matching a traditional thermodynamic profile with the microphysical hydrometeor profile, in addition to

acting as a back-up GPS. An image of the PASIV is provided in Fig. 7.

2.1.3. Radar and Remote-Sensing Instrumentation

Radar and remote-sensing instrumentation include instruments such as radars, lidars, and satellites. Three radars were used to sample the atmosphere during the 12 Feb 2020 blizzard: the NOAA WSR-88D in Mayville, North Dakota (KMVX); the University of North Dakota's NorthPol radar located atop of Clifford Hall; and the CSWR DOW7, located near Thompson, North Dakota during this event. All three radars are dual-polarimetric but operate at various wavelengths: KMVX at 10 cm (S-band), UND NorthPol at 5 cm (C-band), and DOW7 at 3 cm (X-band).

Collocated with UND NDAWN and the Parsivel² was a Lufft CHM-15K 1064 nm laser ceilometer. The ceilometer is a vertically pointing instrument capable of detecting aerosols, clouds, or other hydrometeors that backscatter transmitted radiation. This allows for surface-based detection of blowing snow layers and plumes (Gossart et al. 2017; Loeb and Kennedy 2021).

Multiple satellites provided both passive- and active remotely-sensed observations during the 12 Feb 2020 event. Fortuitously, the ground-track of the *CALIPSO* satellite transected the RRV, allowing for the detection of blowing snow from space with the CALIOP instrument, similar to Palm et al. (2011, 2017, 2018). Daily overpasses were also made by other satellites, including the NASA *Terra* satellite with the Moderate Resolution Imaging Spectroradiometer (MODIS), and the European Space Agency's Copernicus *Sentinel-2* satellite providing excellent high-resolution imagery of the blowing snow plumes driving blizzard conditions in the valley. Finally, *GOES-16* provided imagery of the RRV at multiple wavelengths via the ABI (e.g. Kennedy and Jones 2020).

2.2. Analysis Techniques

2.2.1. Surface and Balloon-borne Data Analysis

Surface data from UND NDAWN, the DOW, and local NDAWN and ASOS stations were used as indicators of surface meteorological variables, providing surface thermodynamic conditions throughout the event. ASOS stations also provided measured visibility within blowing snow. Data from surface stations were also used to determine when the Arctic frontal passage occurs at each station's respective location, indicated by a sudden increase in wind speed, decrease in temperature, and, where applicable, a decrease in visibility and increase in hydrometeor counts.

Thermodynamic soundings were plotted from data collected from radiosondes. These data were analyzed with respect to time to determine thermodynamic changes throughout the duration of the event. In addition, soundings from inside and outside of blowing snow plumes were compared to determine differences in the boundary layer profile thermodynamics and fluid dynamics.

The thermodynamic profiles from the soundings were used to assess operational numerical weather model performance throughout the event. Models include the North American Model (NAM), the NAM-3km, the High Resolution Rapid Refresh (HRRR), the Rapid Refresh (RAP), the Global Forecasting System (GFS), and the UND Weather, Research, and Forecasting model (UND WRF, which was run operationally with parameterization tuned for North Dakota throughout BLOWN-UNDER).

2.2.2. Microphysics and Hydrometeor Imaging Data Analysis

Imagery from the PASIV probe containing hydrometeors were analyzed by the National Severe Storms Laboratory. Hydrometeor sizes were measured and plotted in a particle size

distribution with respect to height. Pre-processed PASIV data from the event are provided by the National Severe Storms Laboratory.

OSCRE imagery were processed in a similar fashion; hydrometeors were measured and their sizes plotted in a particle size distribution as a function of time. Due to the nature of the ground blizzard forced by an Arctic cold front, gamma distributions were fit to the PSDs for the 45 minutes before the frontal passage and 45 minutes after the frontal passage. Analysis of before and after the frontal passage explores differences in the gamma distributions for falling snow (before the front) versus strictly blowing snow (after the front).

OSCRE imagery were processed using the open-source image-processing Python module OpenCV as follows:

- 1) Read in OSORE imagery in .png format.
- 2) Per image, measure the brightness of all pixels. If below a threshold (in this case, 45 on a greyscale of 0 to 255, where 0 is black and 255 is white), it is assumed the image is void of hydrometeors and is deleted from the dataset.
- 3) Perform a median blur to help blend hydrometeor details together. If image blurring is not done, the program may interpret details of an individual hydrometeor as multiple particles instead of one singular particle.
- 4) For each hydrometeor, find the edges by performing `cv2.Canny`, `cv2.dilate`, and `cv2.erode`. Canny attempts to contour the edge of any object in the image and outline that edge, removing any filling. Dilate acts to enhance the contours of the found edges and fill in any gaps in the contour. Erode acts to take the filled-in contours and reduce them to a uniform thickness for measuring dimensions.
- 5) Draw boxes around each edge contour. The short axis of the box is the shortest

- dimension of the hydrometeor. The long axis of the box is the longest dimension of the hydrometeor.
- 6) To determine if the hydrometeors are in focus or out of focus, sharpness and contrast of contours are measured. Sharpness is found via `cv2.Laplacian`, where smaller numbers (in this case, < -3) are considered for hydrometeors in-focus. Pixel standard deviation is calculated to determine contrast and average contrast is calculated. If hydrometeors meet the sharpness and contrast criteria for being in-focus, they are measured. Any hydrometeors that do not meet the criteria of being in-focus are ignored.
 - 7) The box dimensions of all in-focus particles are measured, in pixels. These dimensions are multiplied by the $27 \mu\text{m}$ per pixel resolution of OSCRE. For each hydrometeor, the time of the hydrometeor's image and the dimensions of the hydrometeor are saved to a .txt file for later analysis.

OSCRE data were also used to assess Parsivel² performance in blowing snow. Particle size distributions from each instrument were analyzed with OSCRE serving as ground truth.

2.2.3. Radar and Remote-Sensing Data Analysis

Data from the three radars were examined to understand the kinematics and macrophysics of the frontal passage that initiated the ground blizzard and the HCRs that developed after the frontal passage. Ceilometer data from UND NDAWN were reviewed, which in addition to radar PPI and RHI data enhance understanding of blowing snow layer heights.

CALIPSO satellite data were analyzed in a similar fashion to Palm et al. (2018) where calibrated backscatter from CALIOP were plotted, utilizing a radiosonde launched nearly concurrently with the satellite's passing over the RRV to provide a thermodynamical analysis.

Additionally, CALIOP data provide insight into characteristics of the late-event blowing snow layer.

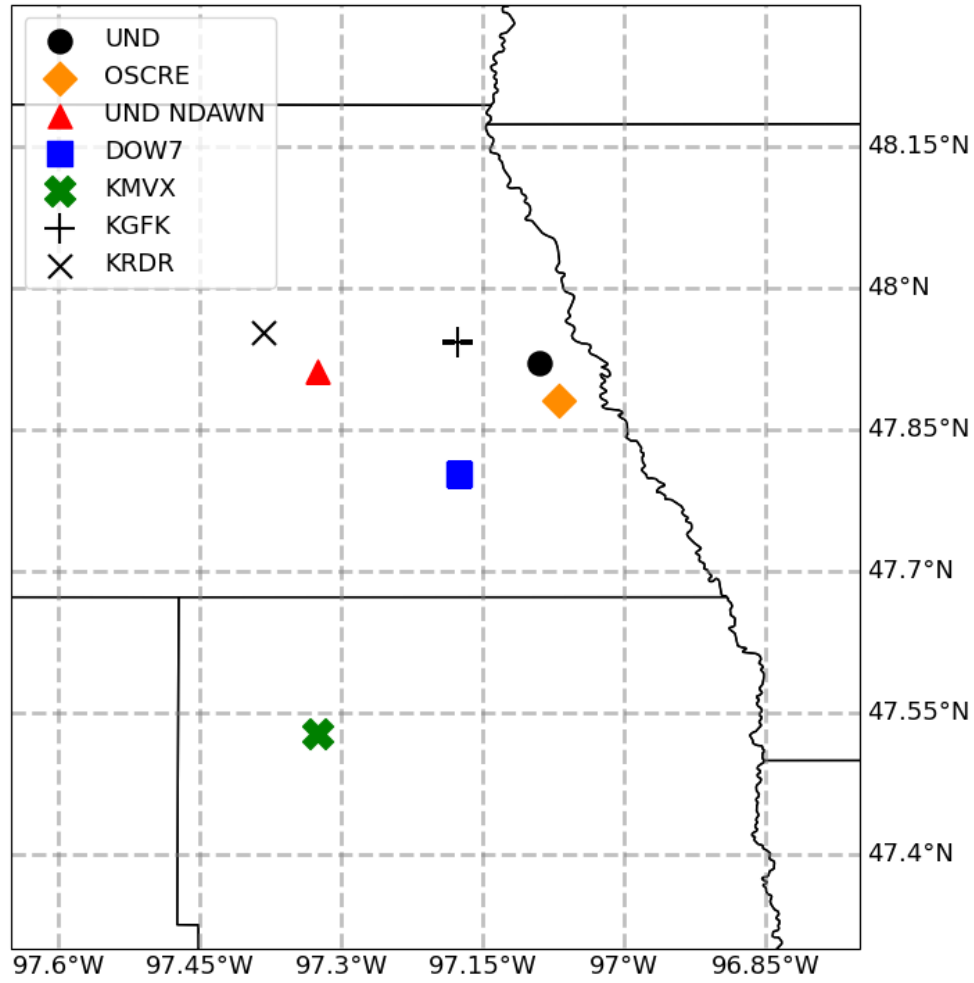


Figure 4 – A map showing locations of instrumentation and surface stations used during the 12 Feb 2020 blizzard. The black dot for UND is the location for the UND NorthPol radar and where balloon launches were conducted.

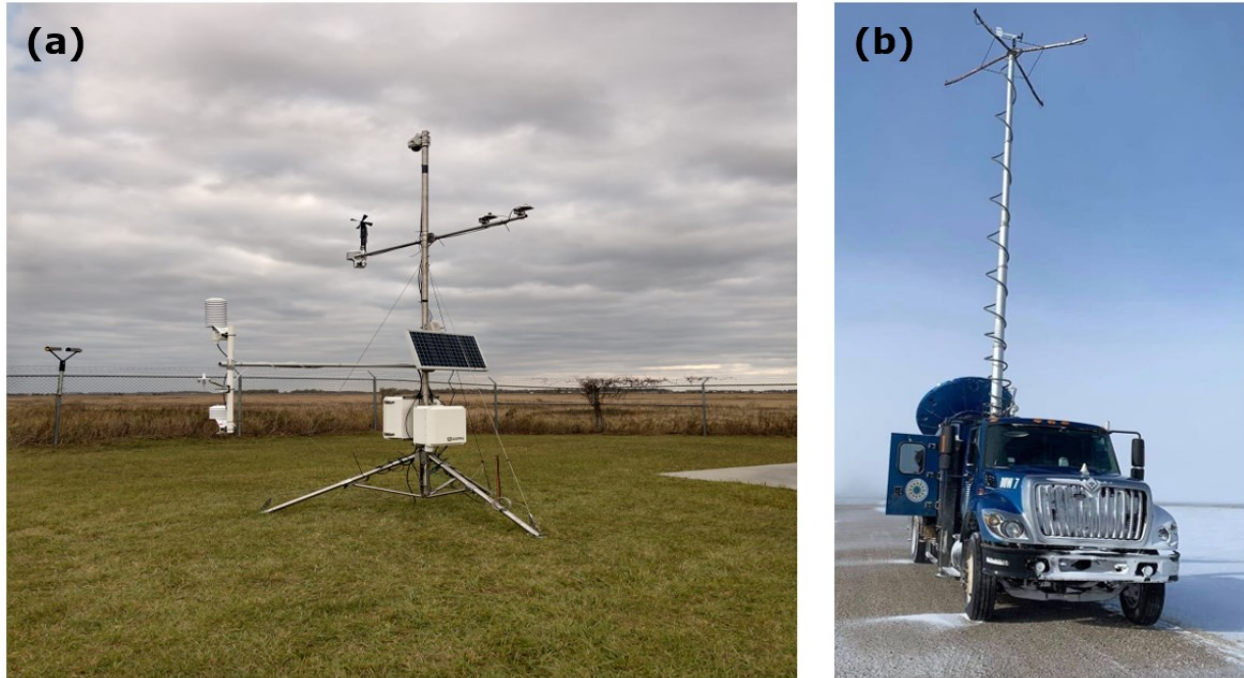


Figure 5 – (a) The temporary UND NDAWN mesonet station located at the Oakville Prairie Observatory near Emerado, ND. The mesonet station is built on a tripod in the foreground, with a Parsivel² mounted to the fence in the background. (b) DOW7 after the 12 Feb 2020 event. On the bed of the truck is an X-band radar, seen as the dish pointing away from the cab of the truck. The 10-m mast holds instrumentation to collect meteorological data. Image of the DOW7 courtesy of Caitlin Connell.



Figure 6 – A picture of the OSCRE. The camera (left housing) captures pictures of hydrometeors in its field of view at the same rate as the strobe light (right housing) flashes. Image courtesy of Dr. Aaron Kennedy.



Figure 7 – A picture of Dr. Aaron Kennedy holding the PASIV near Fertile, MN after retrieving the instrument from a test deployment on 6 Feb 2020. Image courtesy of Dr. Aaron Kennedy.

Table 1 – Instrument availability for the 12 Feb 2020 ground blizzard. Times along the x-axis are in UTC. The instruments are listed along the y-axis and are grouped by category: instruments that fell under the in situ or microphysical instrumentation category have a blue filling; instruments that fell under the radar and remote sensing instrumentation category have a red filling; and instruments that fell under the surface-based instrumentation category have a green filling. Filled boxes indicate that the instrument was used at some point during that hour.

	0500	0600	0700	0800	0900	1000	1100	1200	1300	1400	1500	1600	1700	1800	1900
Radiosondes			■		■		■		■		■	■			■
PASIV			■												
OSCRE		■	■	■	■	■	■	■	■						
DOW7 High	■	■	■	■	■										
DOW7 Low	■	■	■	■	■	■	■	■	■						
UND NorthPol				■	■	■	■	■	■	■	■	■	■	■	■
KMVX WSR-88D	■	■	■	■	■	■	■	■	■	■	■	■	■	■	■
Lufft Ceilometer							■	■	■	<i>Attenuated</i>	■	■	■	■	■
Parsivel ²	■	■	■	■	■	■	■	■	■	■	■	■	■	■	■
UND NDAWN	■	■	■	■	■	■	■	■	■	■	■	■	■	■	■
DOW7 Mesonet	■	■	■	■	■	■	■	■	■						

CHAPTER 3

12 FEBRUARY 2020 METEOROLOGICAL ENVIRONMENT AND IMPACTS

3.1. Meteorological Environment

The day preceding the blizzard was unseasonably warm and sunny for the RRV, with temperatures peaking at $-1.1\text{ }^{\circ}\text{C}$ ($30\text{ }^{\circ}\text{F}$) at Grand Forks International Airport (KGFK) and $-1.7\text{ }^{\circ}\text{C}$ ($29\text{ }^{\circ}\text{F}$) at Hector International Airport (KFAR) in Fargo, North Dakota. These temperatures were catalyzed by southwest winds from an exiting $\sim 1026\text{ hPa}$ surface high pressure system (Fig. 8a, 8b) and 850 hPa temperatures across the valley between -5 and $-10\text{ }^{\circ}\text{C}$ (Fig 10a). Warm temperatures and southwesterly flow persisted into the late evening of the 11th. Just after midnight on the 12th (0600 UTC), an Alberta Clipper propagating in association with an upper-level shortwave trough moved through the region, producing 2.5 to 5 centimeters (1 to 2 inches) of fresh snow across the RRV. Behind the Alberta Clipper was an Arctic front extending from a $\sim 998\text{ hPa}$ low centered over Ontario, Canada, and a strong $\sim 1042\text{ hPa}$ surface high pressure system (Fig. 9a, 9b). Around this time, the snowpack in the valley was between 25 to 50 cm (9.8 to 20 inches; Fig. 11b) deep with an average snowpack temperature below $-5\text{ }^{\circ}\text{C}$ ($+23\text{ }^{\circ}\text{F}$) (NOHRSC 2021).

The Arctic front began its passage through North Dakota at approximately 0300 UTC on the 12th and reached the northern extent of the valley at around 0500 UTC. The front passed KGFK at 0730 UTC with an associated intense pressure gradient and strong northerly winds sustained above 15 m s^{-1} (33.6 mph), above the threshold to dislodge and loft snow from the surface. KFAR was hit by the front at around 0915 UTC. By 1000 UTC, widespread blizzard conditions were realized throughout most of the RRV. A peak wind gust of 26.7 m s^{-1} (59.8 mph) was recorded at KGFK at 0855 UTC.

As the morning progressed, temperatures in the valley continued to fall past $-20\text{ }^{\circ}\text{C}$ (Fig.

9b) with the help of strong low-level cold air advection, with 925 hPa temperatures falling 12 to 24 °C over the RRV between 0600 and 1200 UTC (Fig. 12a). A strong pressure gradient kept wind speeds elevated with the help of 6-hour pressure tendencies as high as +20 hPa (Fig. 12b). Widespread blizzard conditions became more localized as wind-parallel HCRs formed within the valley, driving blowing snow plumes oriented parallel to the valley (Fig. 13). Outside of the blowing snow plumes, mostly sunny skies prevailed. Inside of the blowing snow plumes, reduced visibilities down to near-whiteout conditions were realized. Winds remained elevated into the early afternoon hours allowing blowing snow plumes and localized blizzard conditions to persist.

As the center of high pressure continued propagating toward North Dakota, the pressure gradient weakened, and winds fell below blizzard criteria after 1830 UTC. Blowing snow plumes dissipated in the hours after, with visibilities improving across the region by 0000 UTC on the 13th.

3.2. Weather and the Societal Impacts

Once the Arctic front swept through the region, conditions deteriorated rapidly. UND NDAWN 3-m wind speeds increased from around 5 m s⁻¹ (11.1 mph) before the Arctic frontal passage at 0715 UTC to ~15 m s⁻¹ (33.6 mph) after the frontal passage (Fig. 14b). This caused visibilities at the nearby Grand Forks Air Force Base (~3 km NNW of UND NDAWN) to drop from 7 miles (11.2 km) to 0.25 miles (0.4 km) in a matter of minutes. This reduction in visibility coincides with blowing snow (Fig. 14c; Fig. 15). Parsivel² particle counts per minute increased from several hundred particles per minute before the frontal passage to several thousand particles per minute after the frontal passage. The combination of these factors made travel between cities in the valley nearly impossible, forcing many to stay put until visibility improved. Those that were caught in open country (such as the PASIV retrieval team) became stranded. Interstate 29 – a

north-south interstate highway that runs from the South Dakota border up to the Canadian border through Fargo and Grand Forks, North Dakota – was closed for the duration of the blizzard. The author experienced whiteout conditions and impossible travel conditions once outside of city limits. This prevented a rescue attempt of the PASIV retrieval team; they would return around 1700 UTC on the 12th as conditions improved.

The combination of poor visibility, nearly impossible driving conditions, and dangerously cold wind chills down to -47.2 °C (-53 °F) caused local schools and the University of North Dakota to cancel classes for the day. Some local businesses also closed for the day or reduced their hours to protect their employees from the conditions. Overall, society came to a near halt for at least part of the day. One big reason the blizzard did not end up being more disruptive than it could have is that a bulk of the event occurred during the overnight hours when many were still asleep.

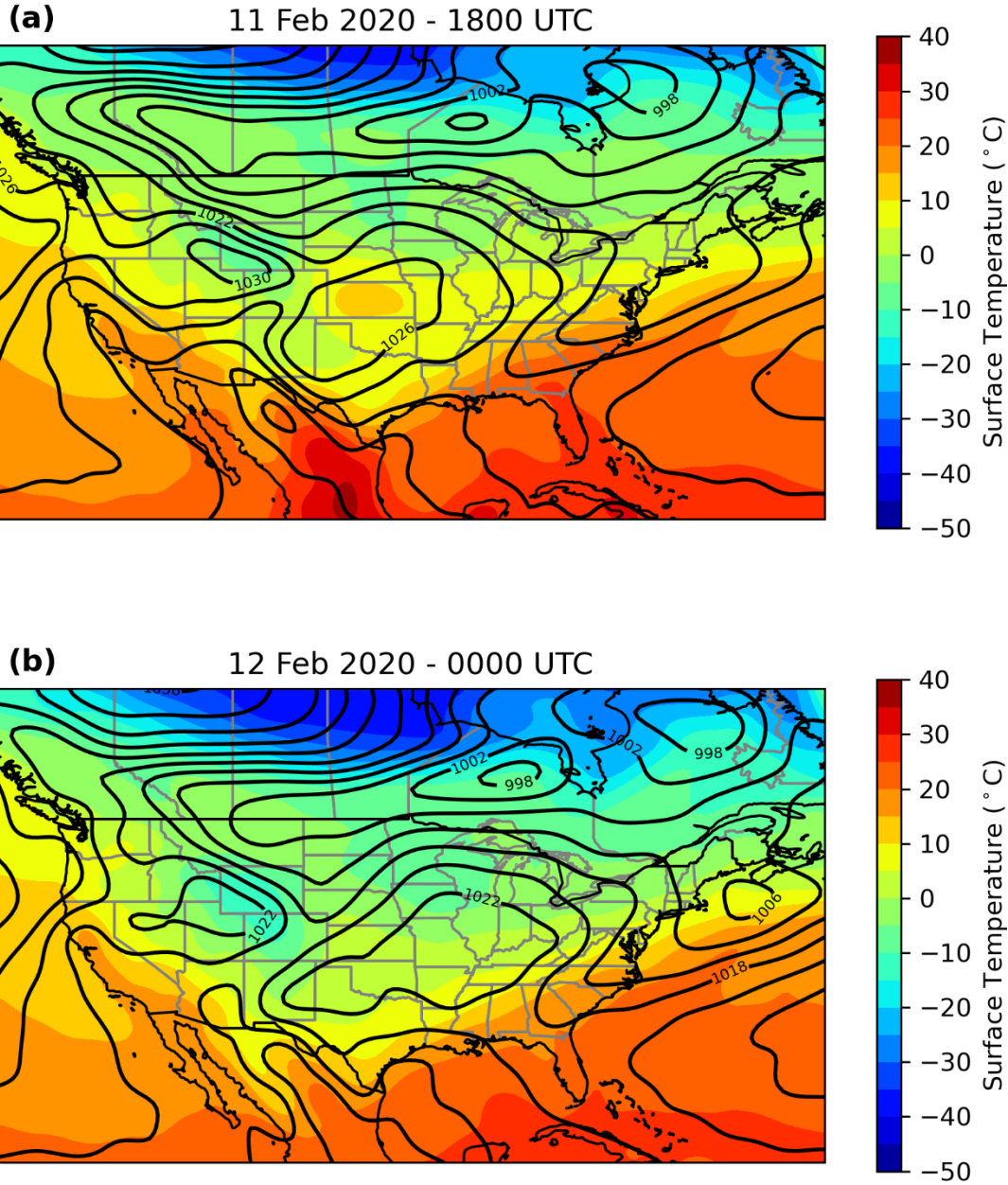


Figure 8 – Global Forecasting System (GFS) analysis MSLP (black contours; hPa) and surface temperatures (color shading; °C) for (a) 11 Feb 2020 at 1800 UTC, and (b) 12 Feb 2020 at 0000 UTC.

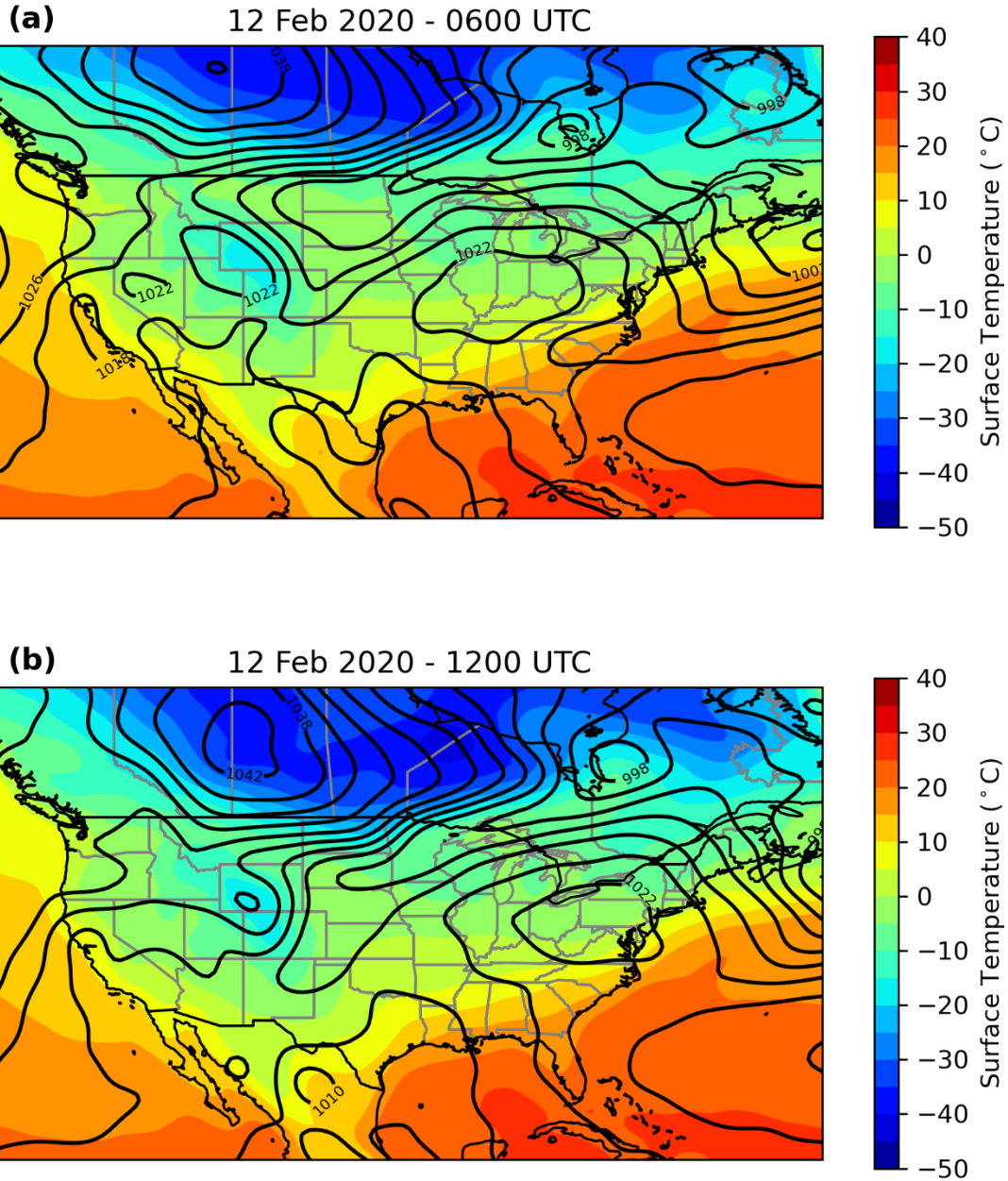


Figure 9 – As in Fig. 8, except for (a) 12 Feb 2020 at 0600 UTC, and (b) 12 Feb 2020 at 1200 UTC.

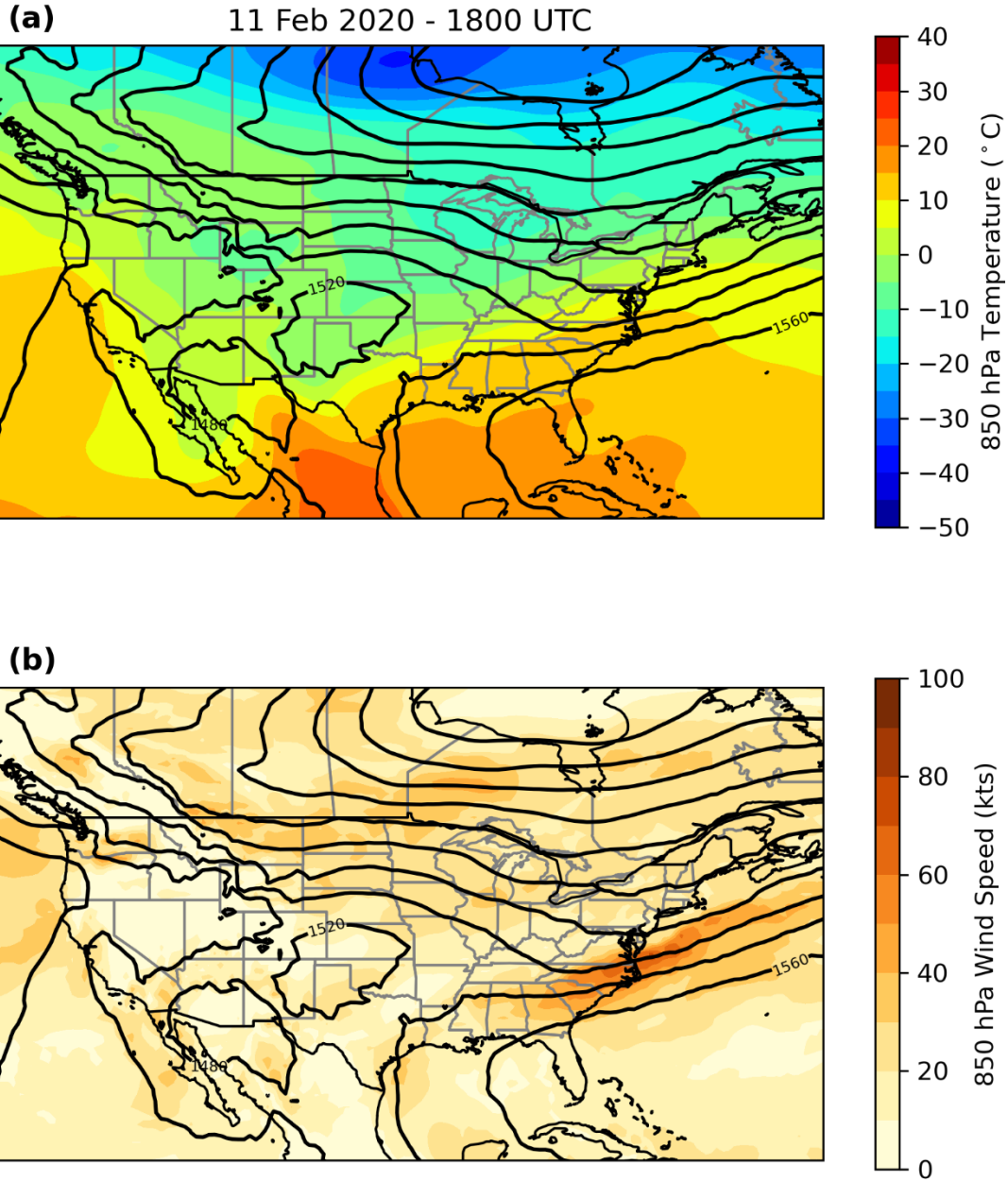


Figure 10 – GFS analysis data on 11 Feb 2020 at 1800 UTC for (a) 850 hPa heights (black contours; meters) and temperatures (colored shading; °C), and (b) 850 hPa heights (black contours; meters) and winds (colored shading; knots).

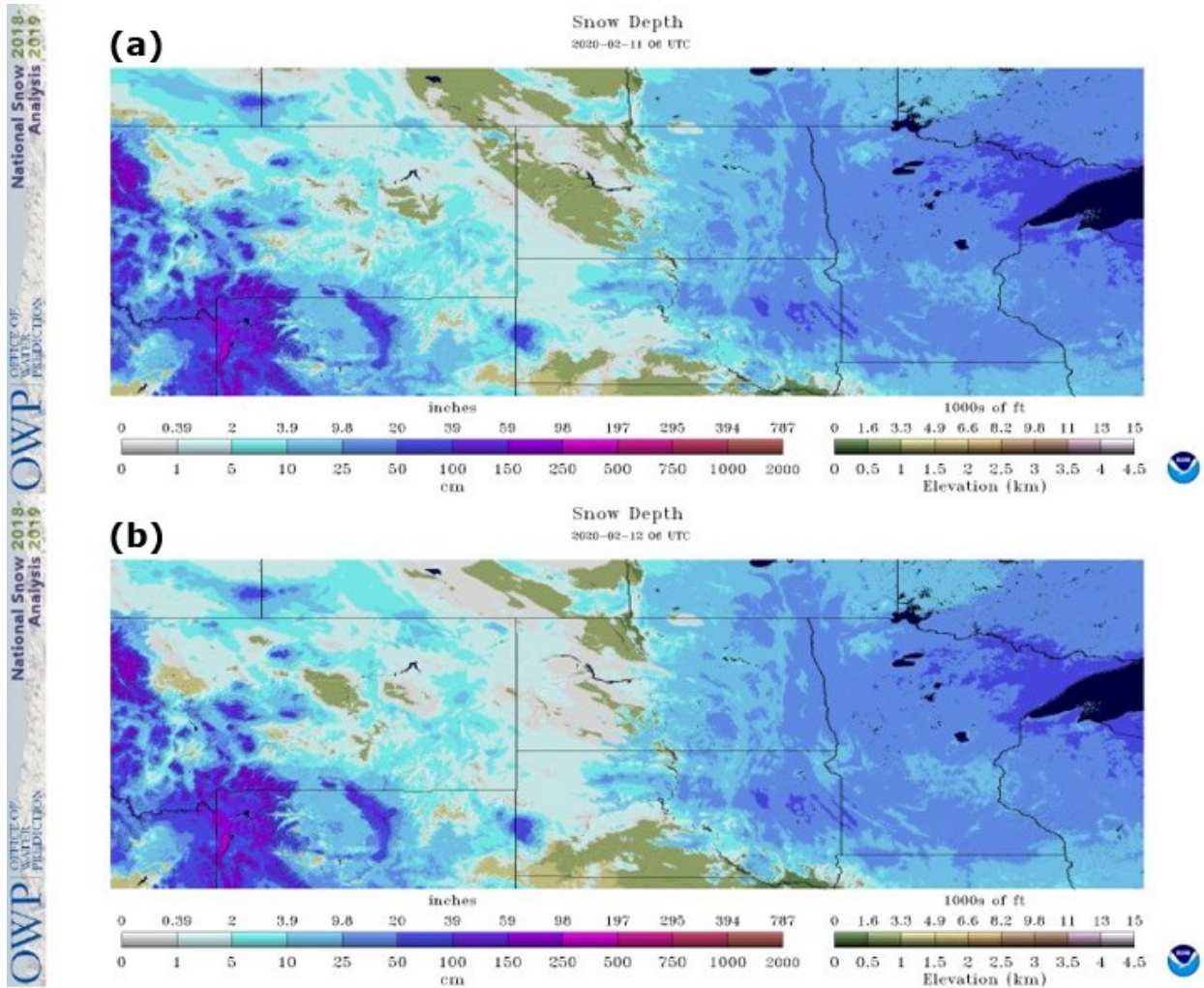


Figure 11 – Snow depth over the Upper Midwest and Northern Plains ending at (a) 0600 UTC on 11 Feb 2020, and (b) 0600 UTC on 12 Feb 2020. Minimal new snowfall was recorded across the Dakotas between the two times. Figures courtesy of the National Operational Hydrologic Remote Sensing Center (NOHRSC).

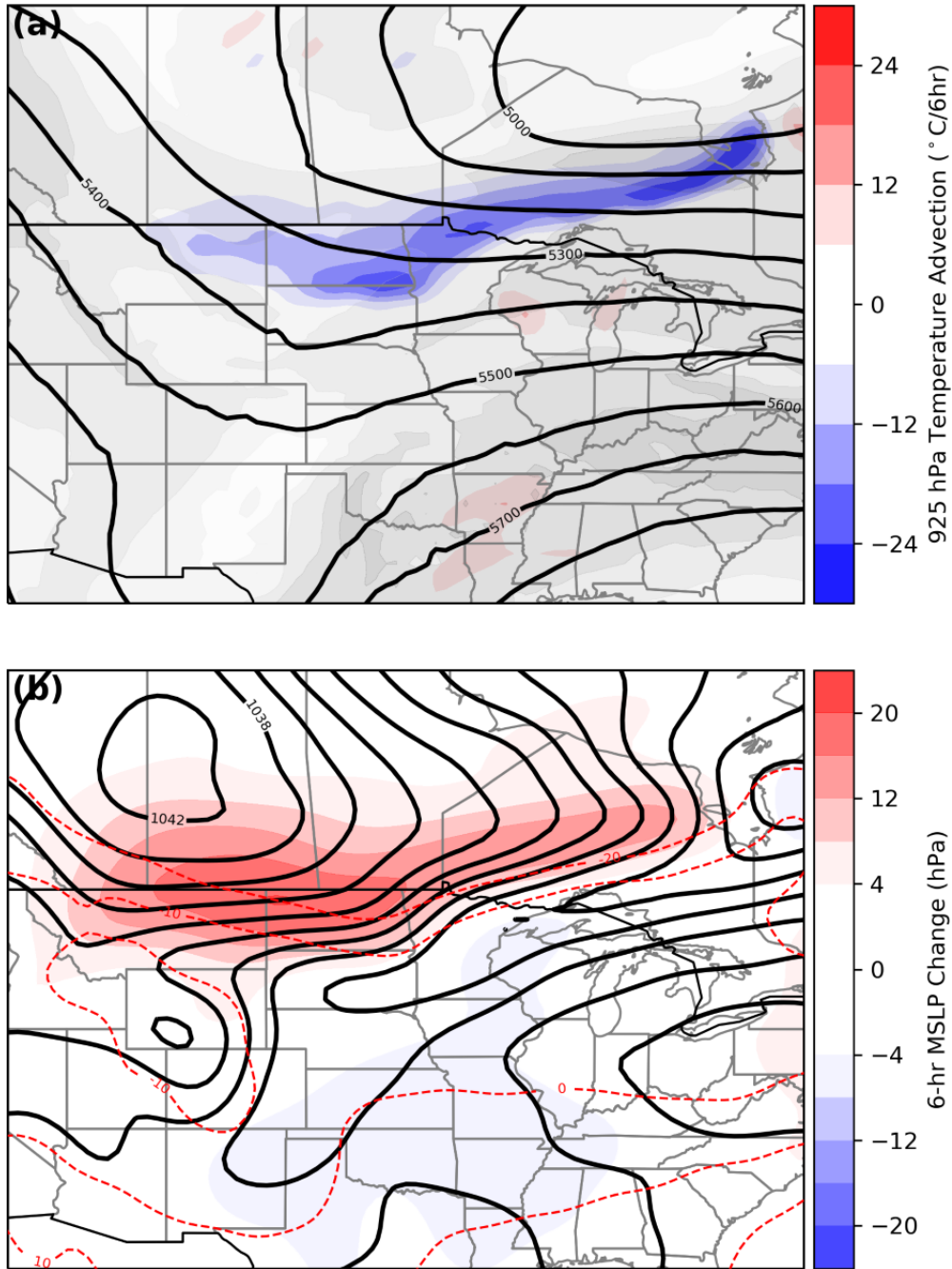


Figure 12 – Data from the GFS initialized at 00Z on 12 Feb 2020. (a) Black lines are model 500-hPa heights in meters at 12 UTC (12 hours into the simulation), semi-transparent grey contours are model 500-hPa wind speeds at 12 UTC, and red and blue shading indicate modelled 6-hour temperature advection at 925 hPa from 06 to 12 UTC, with blue shading indicating cold air

advection and red shading indicating warm air advection. (b) Black lines are model MSLP in hPa at 12 UTC, red dashed lines are model surface temperatures in degrees Celsius at 12 UTC, and blue and red contours indicate modelled 6-hour MSLP changes from 06 to 12 UTC, with blue shading indicating pressure falls and red shading indicating pressure rises.

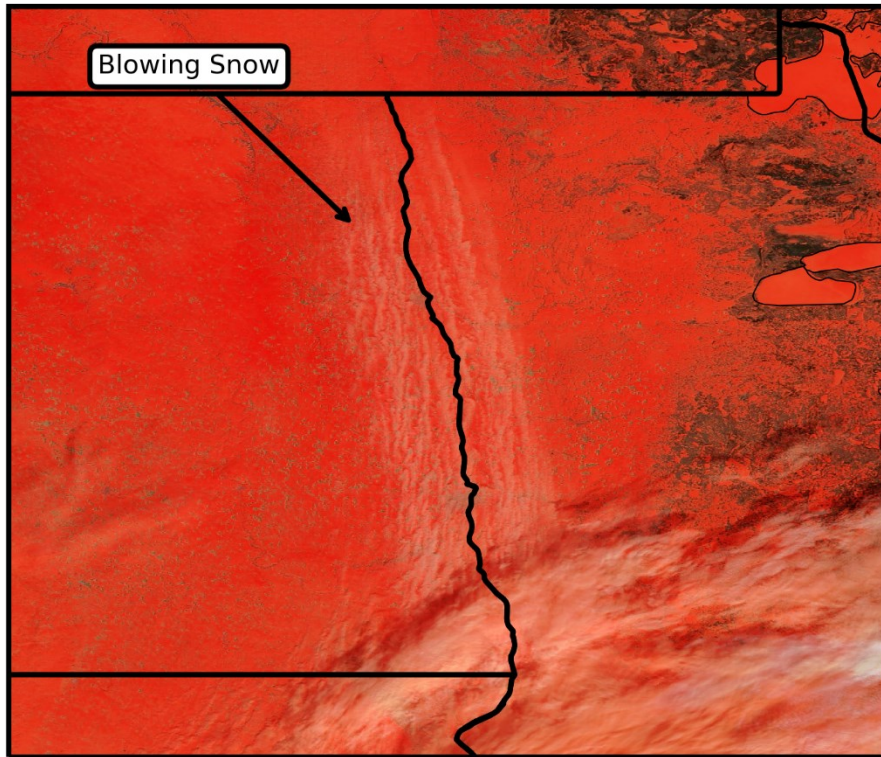


Figure 13 – False color imagery captured with MODIS on NASA’s *Terra* satellite on 12 Feb 2020. Clouds from the exiting Alberta Clipper can be seen over central MN and extreme southeast ND. Blowing snow plumes within the RRV are pointed out.

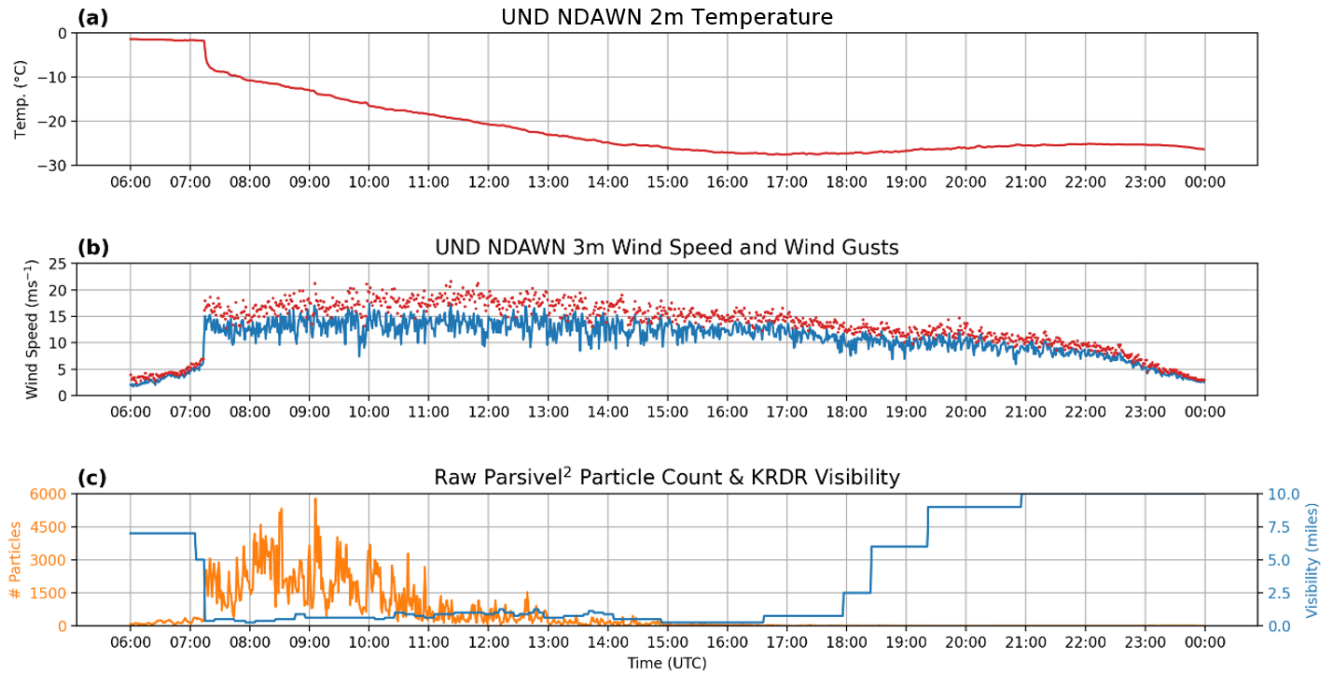


Figure 14 – Meteorgrams featuring (a) 2-meter temperatures at UND NDAWN; (b) 3-meter instantaneous wind speed and wind gusts for every minute, with wind speed in blue and wind gusts in red; and (c) raw Parsivel² cumulative particle counts per minute in orange and KRDR visibility in blue.

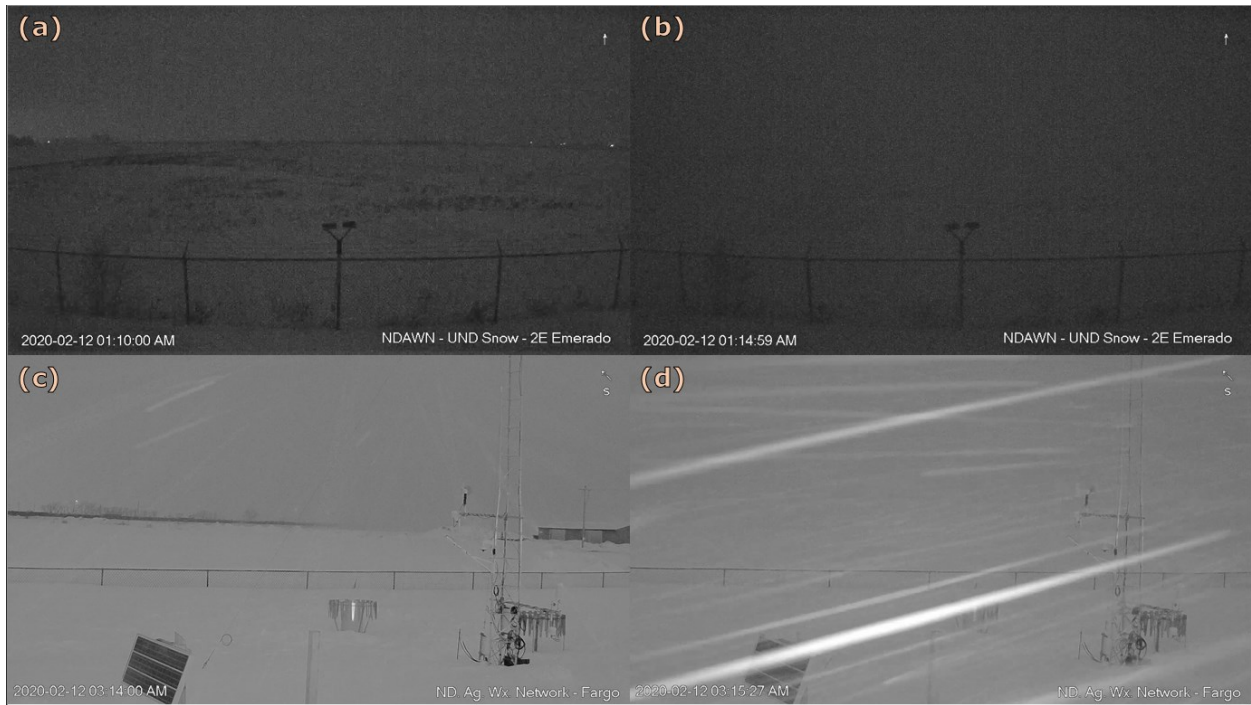


Figure 15 – Webcam imagery from (a) UND NDAWN at 0710 UTC (1:10 AM CST), (b) UND NDAWN at 0715 UTC (1:15 AM CST), (c) NDAWN Headquarters in Fargo, ND at 0914 UTC (3:14 AM CST), and (d) NDAWN HQ at 0915 UTC (3:15 AM CST). (a) and (c) are taken before the Arctic front passes through at the respective locations, and (b) and (d) are taken after the frontal passage when blizzard conditions commence.

CHAPTER 4

RESULTS AND DISCUSSION

4.1. Radar and Remote Sensing Analysis

4.1.1. Radar Analysis

The 12 Feb 2020 event evolved from pre-frontal snow to a strong Arctic frontal passage, with strong winds behind the front helping to sustain blowing snow and blizzard conditions. This evolution was observed with multiple radars, which are analyzed here. UND NorthPol data are not thoroughly examined as contamination at all elevation angles prevented analysis of mesoscale features such as HCRs. It was determined that the radar was calibrated correctly and that faulty equipment in the radar dome may have interfered with the radar's signal, creating artificial "clutter" in the return signal (personal communication, Jared Marquis). Additionally, DOW7 was operational until approximately 1300 UTC when the radar succumbed to the impacts of blowing snow and cold, thus data do not exist from DOW7 after this time.

The initial transition from pre-frontal precipitation to post-frontal blowing snow as observed with DOW7 and KMVX is shown in Figs. 16-21. At around 0720 UTC (Fig. 16-17), the front, which is identified as a fineline stretching across Grand Forks County, North Dakota (Fig. 16a-b), was quickly propagating to the southeast at approximately 16 m s^{-1} . Both radars show pre-frontal, near-surface flow from the northwest at less than 10 m s^{-1} (Fig. 16c-d). Behind the front, winds are significantly greater, with maximum DOW7 radial velocities $\sim 20 \text{ m s}^{-1}$. The front itself had differential reflectivity values of $\sim 0 \text{ dB}$ near the surface (Fig. 17a) and between -1 and 0 dB aloft (Fig. 17b). Differential reflectivity is defined as $Z_{DR} = 10 \log (Z_H / Z_V)$, where Z_H and Z_V are the horizontal and vertical components of radar reflectivity, respectively (Seliga and Bringi 1976). Particles whose horizontal and vertical axes are equal will return a Z_{DR} of 0 dB . Positive Z_{DR}

indicates a larger horizontal axis, and negative Z_{DR} indicates a larger vertical axis. Thus, Z_{DR} values ~ 0 dB near the surface indicate mainly spherical or randomly oriented particles (such as snow) near the surface. Z_{DR} values between -1 and 0 aloft indicate either primarily vertically-oriented particles, or particles whose vertical axes are larger than their horizontal axes. Correlation coefficient values (ρ_{hv}) were near or at 1.0 , indicating strictly meteorological phenomena (Fig. 17c-d).

Approximately 20 minutes later (Fig. 18-19), the front had passed over surface instrumentation at UND NDAWN, OSCRE, and DOW7. Additional stratiform precipitation was occurring just behind the front as evidenced by broad areas of higher reflectivity seen in PPI (Fig. 18a-b) and RHI (Fig. 23) imagery. Near-surface winds behind the front were northerly with speeds near 20 m s^{-1} (Fig 18c). Post-frontal precipitation had similar Z_{DR} values as the front itself, indicating hydrometeors that were ice-phase (PPI: Fig. 19a-b; RHI: Figs. 22c, 23c). By 0756 UTC (Figs. 20-21), the front had passed KMVX, and the fineline associated with the front was visible until 0917 UTC.

RHI scans of the frontal passage provided additional insight into the structure and properties of the boundary. By 0728 UTC, the front was ~ 5 km from DOW7. Behind the frontal boundary, data indicated turbulent flow with multiple surface-based billows of reflectivity up to 20-25 dBZ (Fig. 22a). Associated with these billows were turbulent velocity eddies (Fig. 22b). This structure is similar to the turbulence observed by Geerts et al. (2006) where a frontogenetic cold front acted as a density current with Kelvin-Helmholtz instability along the top of the structure. As seen with the PPI imagery, Z_{DR} values within the boundary were ~ 0 dB (Fig. 22c) and ρ_{hv} values were near or at 1.0 (Fig. 22d). As many of the hydrometeors can be assumed to be snow dislodged from the surface comprised of snowflake fragments (e.g. Fig. 1), $Z_{DR} \sim 0$ dB and

ρ_{hv} near 1.0 make sense. Evidence from PPI imagery also suggest the presence of lobes and clefts (seen as bumps or cusps along the edge of the frontal boundary in Figs. 16a, 18a, and 20a), a common feature of cold fronts and gravity currents, indicative of existing lobe and cleft instability (Simpson 1972; Lee and Wilhelmson 1997; Härtel et al. 2000; Young et al. 2005) which can dominate local transport of mass and momentum (Xie et al. 2019).

The first evidence of blowing snow plumes arranged in HCRs occurred approximately 40-60 minutes after the frontal passage, or approximately 36-54 km (20-30 miles) behind the front (Fig. 24). KMVX radar observations of blowing snow plumes were collected throughout the event until its conclusion around 1900 UTC. During the blizzard phase of the event, the valley-oriented HCRs made analysis of these features in DOW7 RHIs difficult due to the alignment of the rolls with respect to the RHI azimuthal angles. Despite this issue, a few plume cross-sections were successfully viewed with DOW7, as shown in Figs. 25-26. Two plumes of interest can be seen in the 0852 UTC 1.3° PPI scan (Fig. 25a), which were intercepted by the 100° (with respect to north) RHI scan at 0855 UTC as seen in Fig. 26. The closer plume was approximately 1 km in width and 400 m in height, whereas the further plume was approximately 2.5 km in width and 450 m in height, with approximately 4 km distance between the roll centers. These values yield an aspect ratio (wavelength (λ) over height (h); Walter 1980; Atkinson and Zhang 1996; Weckwerth et al. 1997; Young et al. 2002) of 8.89 - 10.0, which is high for land-based rolls (Atkinson and Zhang 1996), but on-par with values calculated for blowing snow plumes by Kennedy and Jones (2020). Shifts in the wind are observed in both plumes, as shown in the storm-relative velocity (SRV) profiles in Fig. 26b. For the plume closest to the radar, SRV toward the radar was observed in the western side of the plume (the side of the roll closer to the radar) and underneath the plume whereas the radar observed SRV was near 0 m s⁻¹ in the eastern side of the plume. Due to the presence of

westward storm-relative motion below and to the west side of the plume and near-zero storm-relative motion to the eastern side of the plume, it is hypothesized the forcing mechanism for suspending blowing snow within the plume is a vertical momentum flux within the updraft of the HCR. A similar wind field was present for the plume further from the radar, however the elevation of the lowest tilt makes it impossible to see the near-surface, storm-relative flow. The SRV signatures of these plumes, particularly the plume closer to the radar where more of the profile is visible, is consistent with the conceptual model for HCRs in Fig. 3. Focusing on the plume closer to the radar, the SRV had a noticeable shift in direction in the center of the plume, ~4.5 km from the radar, with velocities toward the radar favored on the western side of the plume, and velocities near 0 m s^{-1} on the eastern side. SRV toward the radar were observed near the surface on the eastern side (~5 km from the radar) and aloft on the western side (~4 km from the radar). This is indicative of near-surface air parcels being lofted into the updraft between two HCRs as they travel toward the radar.

Since DOW7 was not available after 1300 UTC, an alternative method for diagnosing blowing snow plume height via radar was investigated with KMOVX. A time series with KMOVX reflectivity from a single point near Hatton, North Dakota is shown in Fig. 27. This location was chosen as it was in line with UND NDAWN and the ceilometer but close enough to the radar as to not overshoot blowing snow plumes. Between 1000 and 1100 UTC, the strongest signal was observed below 400 m AGL. Above 400 m AGL, clouds from the exiting clipper still lingered, providing minimal additional falling snow. After 1100 UTC, as the clouds moved away from Hatton, surface-based blowing snow remained, generally peaking to heights around 290 m and occasionally reaching above 400 m AGL.

Another alternative method of diagnosing blowing snow plume height was investigated

with DOW7 and KMVX. Blowing snow plume heights are estimated using the furthest distance away from each radar that plumes are visible and applying the distance to an equation for beam height when applying standard refraction. Given by Rinehart (1997):

$$H = \sqrt{r^2 + R_*^2 + 2rR_*\sin\phi} - R_* + H_o \quad (4.1)$$

where H_o is the height of the radar antenna (20 m for KMVX; 2 m for DOW7), r is the range from the radar to the point of interest, ϕ is the radar elevation angle (0.5° for KMVX; 1.8° for DOW7), and R_* is equal to four-thirds Earth's radius ($\frac{4}{3} \times 6374$ km). The results of these calculations are presented in Fig. 28a. Calculations from DOW7 data end at 1252 UTC, minutes before it succumbed to blizzard conditions. Calculations from KMVX begin at 1128 UTC when the farthest discernable plumes were no longer obscured from elevated precipitation and end at 1900 UTC when plumes fell below the sensitivity of the radar. In the 84 minutes where the two overlap, calculated plume heights from DOW7 were 33–134 m greater than the calculated plume heights from KMVX. This can be attributed to differences in radar sensitivity, where KMVX is less sensitive than DOW7.

4.1.2. Lidar Analysis

The Lufft ceilometer was active throughout the duration of the blizzard (Fig. 28b). The instrument detected fall-streaks due to falling snow prior to the Arctic frontal passage at 0715 UTC. Immediately after the frontal passage, backscatter greatly increased in magnitude and was confined to below 400 m. As the event progressed, the signal was quickly extinguished by blowing snow, remaining attenuated for several hours. Around 1700 UTC, as wind speeds decreased, the signal slowly returned, revealing an elevated blowing snow layer. This layer lifted and eventually dissipated shortly after 2000 UTC, marking the end of the event. This was consistent with

improving visibilities in the region.

Ceilometer backscatter was used to determine the average height of the blowing snow layer every five minutes and was compared to heights estimated from DOW7 and KMVX (Fig. 28a). After the frontal passage and before the signal was attenuated, blowing snow heights estimated from the ceilometer were ~200-350 m lower than those estimated from DOW7. This is likely due to the beginnings of signal attenuation. Later in the event when the ceilometer signal returned, blowing snow heights estimated with ceilometer data were similar to those estimated with KMVX data.

4.1.3. Satellite Analysis

The 12 February 2020 blizzard was observed using multiple satellites, including *GOES-16*, *Terra*, *Sentinel-2*, and *CALIPSO*. *GOES-16* was available for the entirety of the event due to its geostationary orbit, whereas the other three satellites offered limited but high-resolution data during select overpasses from 1700-1945 UTC. All four satellites provided blowing snow observations, providing a unique spatial perspective of the event.

The geostationary orbit of *GOES-16* allows for the evolution of the blizzard to be investigated. Hourly images from the 1.63- μm band (band 5, a near-infrared “snow/ice” band) are provided in Figs. 29 and 30. With this band, blowing snow plumes are brighter (more reflective) than the ice-covered background due to differences in scattering at this wavelength. As a result of this scattering, clouds, particularly liquid water clouds, appear brightest. As shown in Fig. 29a-c, blowing snow plumes behind the Alberta Clipper consolidate into the RRV where blizzard conditions persisted through the morning and into the afternoon of the 12th. Later into the day, as wind speeds near the surface decreased from north to south, blowing snow plumes dissipated from

north to south (Fig. 30a-d). Farther south, blowing snow plumes could not be seen due to the presence of optically thick clouds above the plumes (Fig. 29a-b).

An overpass by the NASA *Terra* satellite at around 1700 UTC offers a higher resolution view of the blowing snow than *GOES-16* (250-m versus 1-km resolution). A false color image created from the 0.450- μm , 1.628- μm , and 2.105- μm bands is shown in Fig. 31. This composite imagery allows for discrimination of the blowing snow plumes (grey-brown) versus the snow-covered surface (red). It is also easier with this color scheme to see the height difference between the blowing snow plumes and the clouds in the exiting Alberta Clipper. The clouds, although shallow in depth, were at a high enough altitude to cast shadows on the surface. Conversely, the blowing snow plumes were shallow enough (or possibly optically thin enough) to cast no shadows.

A fortuitous *Sentinel-2* overpass allowed for a high-resolution (20-m) view of the blowing snow plumes around 1730 UTC. Figure 32 shows the resulting imagery when bands 4 (0.665- μm), 11 (1.614- μm), and 12 (2.202- μm) are combined into a composite. Snow and ice appear blue, water as black or dark blue, and other land surfaces as a variety of colors. Clouds and other atmospheric features appear brighter, such as the north-south rolls seen in Fig. 27a. A close-up view of these rolls centered over Grand Forks is shown in Fig. 27b. It is clear that HCRs west of Grand Forks exhibited more turbulent structure than those east of Grand Forks, which were more laminar. The high resolution of the *Sentinel-2* data allows for the roll aspect ratio to be calculated. In Fig. 32b, roll wavelength varied between ~ 2 km (see rolls southwest of Grand Forks) to ~ 10 km (see rolls east of Grand Forks). Assuming a roll depth of 425 m (based on radiosonde observations of the boundary layer from 1640 UTC), this yields an aspect ratio between 4.7 and 23.5, which is near-average to very high for land-based rolls (Atkinson and Zhang 1996).

Another fortuitous overpass was made by *CALIPSO* toward the end of the event around 1945 UTC. The overpass was aligned from 44.0°N, 95.5°W (Des Moines River Township, Minnesota) to 49.0°N, 97.5°W (Neche, North Dakota). Although the event was wrapping up in the northern RRV and near Grand Forks, visibilities were still reduced in Fargo, North Dakota (~120 km or 75 mi south of Grand Forks) and into southwest Minnesota at the time of the overpass. For example, from ASOS data, the surface winds in Fargo, North Dakota at 1945 UTC were from 340° at 12.3 m s⁻¹ gusting to 16.5 m s⁻¹ (24 kts gusting to 32 kts) with visibility down to 0.8 km (0.5 mi) and unknown precipitation. Similarly, in Wheaton, Minnesota (~240 km or 150 mi south-southeast of Grand Forks, or ~120 km or 75 mi south-southeast of Fargo), at 1955 UTC the surface winds were from 350° at 14.4 m s⁻¹ gusting to 18.0 m s⁻¹ (28 kts gusting to 35 kts) with visibility down to 0.8 km (0.5 mi) and light snow reported. Conversely, at KFGF and KRDR, visibilities had improved to 4.8 km (3 mi) and 14.5 km (9 mi), respectively.

Calibrated attenuated backscatter data from the CALIOP instrument are shown in Fig. 33. Throughout the valley, blowing snow plume heights are consistent with what was observed with the Lufft ceilometer. As viewed with the satellite, plume heights range from approximately 300 to 475 m with greater backscatter values toward the top of the plumes. The location of higher backscatter values makes sense since the lidar's signal cannot easily penetrate through optically thick layers. As it may be mistaken that the feature detected with CALIOP is elevated in nature since the signal does not penetrate the entire layer, verification of conditions below the maximum backscattering can be made with previously described surface instrumentation. Based upon previously discussed surface data, blowing snow plumes were elevated over Grand Forks at this time while they were still near the surface over southern portions of the RRV.

4.1.4. Discussion

Radars have been used in the past to investigate characteristics of blowing snow (e.g. Kennedy and Jones 2020; Walter et al. 2020; Loeb and Kennedy 2021). The varying wavelengths of radars used in these studies – 0.8 cm (Ka-band) in Loeb and Kennedy (2021), 1.25 cm (K-band) in Walter et al. (2020), and 10 cm (S-band) in Kennedy and Jones (2020) – allowed for different aspects of blowing snow to be investigated. Presented were similar observation methods using multiple radars of different wavelengths and sensitivities. Regardless of sensitivity, the primary features of interest, including the frontal boundary, blowing snow plumes, and pre- and post-frontal precipitation, were visible with all three radars (notwithstanding blowing snow plumes on UND NorthPol due to technical issues). Radar sensitivity is an important consideration when investigating blowing snow plumes. The lower sensitivity of KMOVX was an issue when calculating blowing snow plume height since the radar was incapable of detecting the highest portions of the plumes, resulting in heights being estimated more than 100 m shallower than other instruments at times. The lack of an RHI scan strategy with KMOVX also prohibited a detailed look at plume cross-sections like what was possible with DOW7. When RHI scans successfully intercepted blowing snow plumes, important information about plume shape and circulations that drive the plumes were apparent. RHI scans also allowed for analysis of the structure of the frontal boundary. A very turbulent environment consisting of Kelvin-Helmholtz billows and lobes and clefts was observed, similar to those seen in previous studies such as Geerts et al. (2006) and Young et al. (2005). While it cannot be definitively concluded that either the Kelvin-Helmholtz billows or lobe and cleft instability are responsible for blowing snow initiation, these processes may have played a role in dislodging snow from the surface.

Regardless of the radar used, two challenges arose when viewing blowing snow plumes:

1) plumes are shallow features that can exist below the minimum beam height of the radar and hence be undetectable; 2) plumes can become obscured by precipitation signatures. To remedy these challenges, lower elevation angles can be used to view under the precipitation, but ground clutter close to the radar can then obstruct the radar beam. Further, radar reflectivity is proportional to $N*D^6$, where N is the number and D is the diameter of scatterers (Sekhon and Srivastava 1970; Smith et al. 1975; Chandrasekar and Bringi 1987). Because D is smaller for blowing snow, the signal will be dominated by falling snow.

Past research has demonstrated that ceilometers can be useful tools for observing blowing snow plumes (e.g. Gossart et al. 2017; Loeb and Kennedy 2021). For this study, limitations are apparent as the signal was quickly extinguished during the blizzard. This emphasizes the importance of having radar in addition to lidar during blizzard events. Radar data were used to fill in some of the missing blowing snow plume heights, but radar has limitations such as not always being able to observe features close to the surface.

Satellites can be a valuable tool when optimal conditions are present. For instance, ground-based blowing snow plumes cannot be seen if optically thick clouds are present above the plumes (such as south of Grand Forks in Fig. 29a and 29b). Thus, clear skies are needed to see the blowing snow plumes. Additionally, near-infrared channels are only useful during the daytime since these channels require the reflection and refraction of insolation. Channels that view longer wavelengths, such as infrared, can be used at nighttime—however plumes may be indistinguishable from the surface if they have similar brightness temperatures. Although satellites can be a powerful tool for nowcasting blowing snow, conditions must be right to view the phenomenon. Similar conclusions were drawn in Kennedy and Jones (2020). High-resolution polar-orbiting satellites offer an excellent opportunity to observe the meso- and microscale structure of blowing snow plumes and,

when coupled with observations of blowing snow plume or boundary layer depth, can be used as another means to determine HCR aspect ratio. Polar-orbiting satellites usage is limited by their temporal resolution, often having a revisit period of 0.5 to 1 day, making them sub-optimal for nowcasting.

4.2. Surface In Situ Analysis

4.2.1. OSCRE

Hydrometeor imagery were collected with OSCRE between 0645-1221 UTC. With a framerate of 30 frames per second, approximately 750,000 images were taken and then processed. A time-series of PSDs is provided in Figure 34b. Pre-frontal precipitation dictated the profile prior to 0730 UTC with particles sizes typically < 1 mm in diameter. After 0715 UTC and just before the front passed over OSCRE, an increase in snowflakes > 3 mm was observed. With the front passing over OSCRE at 0730 UTC, particle population increased dramatically, particularly for sizes < 1 mm in diameter. This is apparent in greater detail in Figs. 35 and 36 where gamma distributions and two-dimensional PSDs for the 45 minutes before and after the frontal passage are plotted. Before the frontal passage, the gamma distribution was flatter than those typical of blowing snow (Pomeroy 1988), indicating that hydrometeors observed with OSCRE were diverse in size (Fig. 35a). This is also due in part to the overall fewer number of particles observed compared to the 45 minutes after the frontal passage, where the number of particles observed that were smaller than 1 mm increased significantly after the front passed (Fig. 35b versus 36b). Collectively, these features indicate hydrometeors were falling snow. The gamma distribution observed after the frontal passage more closely matches the distribution from Pomeroy (1988), with higher numbers of smaller hydrometeors.

Some discrepancy can be expected between previously documented distributions and those

calculated from OSCRE data. OSCRE can only identify hydrometeors with diameters $> 54 \mu\text{m}$ whereas Pomeroy (1988) and similar studies (e.g. Budd 1966, Déry et al. 1998) included particles as small as $2 \mu\text{m}$. This is exemplified with a post-front mean particle radius of 0.162 mm versus the suggested 0.100 mm particle radius by Pomeroy (1988). This number is also likely biased upward due to some post-frontal snowfall. Overall, particle sizes smaller than 0.5 mm were most common. A summary of the gamma distribution values for the event is provided in Table 2.

4.2.2. OSCRE vs Parsivel²

The OSCRE was used as ground truth to assess the performance of the Parsivel² laser disdrometer. Loeb and Kennedy (2021) observed in Antarctica that the Parsivel² had overly broad PSDs and reduced particle counts for smaller particles at higher wind speeds, suggesting flawed performance during blowing snow events. A comparison of PSDs between the two instruments is presented in Fig. 34. During the pre-frontal falling snow, PSDs were similar, favoring particle sizes near and below 1 mm with a larger spread of particle sizes in the 7-10 minutes immediately before the frontal passage. After the frontal passage, Parsivel² observations were similar to those observed in Loeb and Kennedy (2021). Using OSCRE as ground truth, PSDs were predominately composed of particles $< 1 \text{ mm}$ in diameter with few particles $> 2 \text{ mm}$ in diameter (Fig. 34b). Conversely, the Parsivel² observed a broader distribution of particles sizes, with the majority falling between $1\text{-}3 \text{ mm}$ in diameter and additional particles $> 3 \text{ mm}$ in diameter (Fig. 34c). This characteristic lasted for the duration of the blowing snow event. Imagery from OSCRE prove that the Parsivel² measurements are inaccurate as the concentration of larger particles is unrealistic.

4.2.3. Discussion

The results from OSCRE show promise in its ability to provide observations of both falling and blowing snow. The gamma distributions computed from observations agree well with previous studies, and PSDs evolve as expected during an event that transitioned from falling to blowing snow. The results from the analysis of the OSCRE and Parsivel² provide the first clear evidence that the Parsivel² has erroneous PSDs at high wind speeds. Observations from this study are supportive of the hypothesis in Loeb and Kennedy (2021). However, additional work is needed to retrieve number concentrations from OSCRE and Parsivel².

4.3. Balloon-borne Data Analysis

4.3.1. Evolution of the Boundary Layer

Meteorological soundings were launched at 0500, 0645, 0930, 1140, 1500, 1640, and 1945 UTC. Each of the soundings, except 0645 UTC, are shown in Fig. 37 (the 0645 UTC sounding is investigated separately with PASIV data).

Before the frontal passage, the column was relatively moist with temperatures decreasing an average of $4.75^{\circ}\text{C km}^{-1}$ in the lowest 3 km. The lowest 150 hPa became more moist between 0500 UTC (Fig. 37a) and 0645 UTC (Fig. 40) as snow eventually fell to the surface, eroding a surface-based inversion that existed at 0500 UTC. Winds up to 850 hPa exhibited veering before mildly backing at higher heights.

After the frontal passage, significant changes to the profile were observed (Fig. 37b-f). In the first four to five hours after the frontal passage, the boundary layer cooled rapidly, particularly around 925 hPa where the temperature decreased from -4.0°C at 0645 UTC to -21.1°C at 1140 UTC. The environmental lapse rate in the boundary layer peaked at $21.3^{\circ}\text{C km}^{-1}$ at 0930 UTC

(-10.0 °C at the surface to -18.0 °C at 375 m AGL) and maintained a super adiabatic lapse rate throughout the event (the boundary layer environmental lapse rate bottomed out at 12 °C km⁻¹ at 1945 UTC). Care was taken to make sure all radiosondes were acclimated to the outside conditions before launch to avoid unnatural contamination of the profile, thus the observed super adiabatic lapse rates are considered to be true. Over time, the profile became dryer, particularly above the boundary layer when mid-level clouds exited the region (Fig. 37c-d). After 1140 UTC, the most humid portion of the atmosphere was the blowing snow layer within the boundary layer. Observed moisture levels in the boundary layer varied based on whether the sounding was launched inside or outside of blowing snow plumes. A more detailed analysis of the thermodynamics inside versus outside of a blowing snow plume is provided in section 4.3.3.

The wind profile also exhibited large changes before and after the frontal passage. Before the frontal passage, winds were out of the southwest at the surface and veered to the north with height, peaking at no more than ~12.8 m s⁻¹ (25 kts) below 800 hPa. After the frontal passage, winds below 800 hPa turned northerly, ranging between 12.8-23.2 m s⁻¹ (25-45 kts) throughout the boundary layer in a direction between 345° and 15° (NNW and NNE). Above 800 hPa, winds backed with height, which agrees with the intense cold air advection seen at lower levels and the more gradual cold air advection at mid-levels.

4.3.2. PASIV

The PASIV was launched at 0645 UTC into pre-frontal precipitation and ascended to 5591 m (minimum pressure of 445.8 hPa) before a hotwire cut-off timer detached the instrument from the balloon. Throughout the column, smaller particles with diameters < 1.5 mm were observed, with two maxima in diameters < 1 mm recorded around 1 and 2 km AGL (Fig. 38a). These maxima

coincide with areas of elevated reflectivity where Z_{DR} ranges from 0-2 dB, corresponding with the large population of smaller snowflakes and a mix of fewer larger dendrites (Fig. 38b, 38c). A third, less evident maximum was found at a height of ~ 3.75 km AGL, coinciding with a less-intense layer of elevated reflectivity with Z_{DR} from 0-1 dB. The majority of particles greater than 2 mm in diameter were found below 2.5 km AGL. This suggested the development of aggregation and is supported by hydrometeor images captured with OSCRE (Fig 39). Thermodynamically, the atmosphere did not allow for the development of larger snowflakes during this time. As seen in the skew- T log- p diagram in Fig. 40, the thermodynamic profile from a radiosonde launched with the PASIV shows the dendritic growth zone was elevated and shallow (1563 m deep from 756.5 hPa to 615.4 hPa), limiting the development of larger snowflakes.

4.3.3. Spatial Variability of Thermodynamics

The soundings at 1500 and 1640 UTC were launched out- and inside of blowing snow plumes, respectively, as the plumes passed over Clifford Hall (Fig. 41). At both times, the boundary layer is shallow compared to the rest of the profile with heights ~ 435 m for both soundings. These heights are similar to blowing snow plume heights observed with the ceilometer, radar, and CALIOP in section 4.1. The boundary layer at 1500 UTC was consistently 1.8 to 2.2 °C warmer than at 1640 UTC. The dewpoint profiles in the lowest tens of meters followed a slightly different profile, where dewpoints with respect to geopotential height decreased faster at 1500 UTC (-27.5 °C at the surface to -34.6 °C at 78 m AGL) than at 1640 UTC (-29.5 °C at the surface to -33.4 °C at 77 m AGL). Above this layer, the dewpoint remained nearly constant throughout the boundary layer at 1500 UTC. Conversely, at 1640 UTC, the dewpoint continued to decrease with height, eventually becoming colder than the dewpoint profile at 1500 UTC. Both the temperature

and dewpoint profiles just above the boundary layer remained nearly constant with time, varying no more than 1 °C over time with respect to pressure between 930 and 900 hPa, or 1.2 °C over time with respect to geopotential height between 450 and 703 m AGL.

4.3.4. Discussion

The evolution of the boundary layer appeared to follow a combination of the traditional theory of cooling by sublimation of blowing snow, and through mixing of dry and moist air from different levels as described by Palm et al. (2018). The entire boundary layer cooled and became more saturated with time, with average relative humidity throughout the layer increasing from 55.0% at 1500 UTC to 65.1% at 1640 UTC. A near-equal cooling throughout the entire boundary layer suggests influence by sublimation. Although the entire boundary layer became more moist, since the dewpoint profile saw its lapse rate within the layer increase with time, the bottom half of the boundary layer moistened more than the top of the boundary layer (relative humidity increased from 44% to 62% near 975 hPa, versus 58% to 65% near 930 hPa). Even though the profile did not become dryer with height as Palm et al. (2018) suggest it should, it does suggest that significant mixing was present in the boundary layer to mix dryer air from lower levels to higher levels to lower the dewpoint at the top of the boundary layer.

A key process that makes it difficult to ascertain how much of an influence sublimation and mixing truly had on the boundary layer is the background cold air advection present throughout the event. Evidence that suggests sublimation played a role lies in analysis of profiles between 1640 and 1945 UTC (Fig. 37e-f), the latter sounding being near the end of the event when winds were beginning to die down and the amount of suspended snow was decreasing.

4.4. Numerical Weather Model Performance

An important tool for forecasting blizzard conditions is numerical weather prediction (NWP) with computer models. An assessment of operational model performance for this event follows for the GFS, NAM, NAM-3km, RAP, and HRRR models. For all models, the 00 UTC initializations from 12 Feb 2020 are analyzed at model hours 0500, 0700, 1200, 1500, 1700, and 2000 UTC.

4.4.1. Pre-Frontal Passage

The soundings from 0500 and 0645 UTC are compared to the model outputs from hours 0500 and 0700 UTC. Overall, the models had a decent grasp on the atmospheric profile before the Arctic frontal passage with varying degrees of temperature, dewpoint, and wind magnitude and direction errors. The global model had a distinct moist bias leading up to the frontal passage, whereas the mesoscale models had dry biases at 0500 UTC that eventually gave way to moistening. Details of the model biases are provided below.

The 0500 UTC observed sounding versus each of the model soundings is presented in Fig. 42. At this point in time, the observation is 2.5 hours before the frontal passage at the balloon launch site in Grand Forks, North Dakota. The only global model (GFS; Fig. 42a) was too moist throughout the sounding. Conversely, each of the mesoscale models (NAM, NAM-3km, HRRR, and RAP; Fig. 42b, 42c, 42d, and 42e, respectively) had some degree of a dry bias in the 1000-750 hPa layer, particularly above 925 hPa. Model biases for temperature and relative humidity (RH) are shown in Fig. 43. Although the GFS was too moist, it was the closest to the observed temperature and RH, varying no more than ~ 2 °C throughout the profile, and 10% RH above 950 hPa. The mesoscale models were too cold near the surface and too warm between ~ 950

and 800 hPa. Above 700 hPa, all of the models performed well thermodynamically, with temperature errors within ± 1.25 °C and RH errors within -3 to +11%. With respect to winds, all the models did a reasonable job of resolving the correct wind direction throughout the profile within an error of $\sim 20^\circ$ at most levels (Fig. 42a-42e). Despite this agreement, all models struggled with wind magnitude at different levels. Overall, wind magnitude was $2.5\text{-}5.1$ m s^{-1} (5-10 kts) too high in the boundary layer and as much as 12.9 m s^{-1} (25 kts) too high aloft for almost all of the models. The RAP had the most accurate surface winds, with the correct magnitude and direction within $\sim 10^\circ$ of observations.

Results for 0645 UTC are presented in Fig. 44. This sounding was launched with the PASIV into pre-frontal precipitation. The GFS, HRRR, and RAP resolved a moist profile, whereas the NAM and NAM-3km both had a dry level around 900-925 and 800 hPa. A breakdown of temperature and RH errors is included in Fig. 45. Both the NAM and NAM-3km had temperatures closest to reality, but also had RH values that were the furthest off, resulting in an inaccurate moisture profile. Below 775 hPa, the GFS was too cold with dewpoints too high, resulting in a profile in the lower levels that is too moist (Fig. 44a, 45b). The HRRR and RAP both are too moist throughout the column. With respect to winds, the models struggled with timing of the shift in wind direction below 800 hPa (Fig. 44a-e), particularly the NAM and NAM-3km. The HRRR and RAP each were too quick with the wind shift. Although wind magnitudes below 900 hPa were more accurate at this time than at 0500 UTC, the models still struggled with wind magnitude aloft.

4.4.2. Post-Frontal Passage

After the frontal passage, timing and magnitude of changes in atmospheric thermodynamics and kinematics became issues for the models. Most of the models tended to have

cold biases, particularly early on, with consistent issues resolving accurate moisture profiles. The models performed decently at resolving the correct wind directions throughout the atmosphere with time but struggled at times with magnitudes. Details of model errors are provided below.

A model analysis for the 0930 UTC sounding is not provided due to the sounding being directly in the middle of two model hours. Thus, the 1140 UTC sounding will be the first post-frontal sounding used here for model analysis, the results of which are presented in Fig. 46. All models cooled the boundary layer temperature and dewpoint profiles quicker than what was observed. In addition, all models developed a dry layer just above the boundary layer that was not observed. Model struggles within the boundary layer are evident in the temperature and RH error plots in Fig. 47. Just above the surface, the NAM and NAM-3km fared the best with forecasted temperatures within the boundary layer, whereas the other models were off by more than 3 °C for temperature but performed better at forecasting moisture. From the top of the boundary layer to 700 hPa, the models exhibited varying degrees of success with temperatures, but all had a layer where dewpoints were too cold, with all models but the RAP resolving RH values > 30% too low. Above 700 hPa, all models performed well in the mid and upper levels of the atmosphere. With respect to winds, all models had a good grasp of wind direction throughout the column (Fig. 46a-e). Wind magnitude was still a struggle throughout the column, particularly in the boundary layer. In the boundary layer, all models had winds that were 2.5-7.7 m s⁻¹ (5-15 kts) too weak.

The 1500 UTC observed sounding versus each of the model soundings is presented in Fig. 48. While the models correctly dried out the atmosphere above the boundary layer, the amount of drying at different levels varies. The NAM and NAM-3km did well with temperature forecasts but struggled significantly with dewpoints. The other models fared well with forecasting temperatures above the boundary layer, but they kept the boundary layer itself too cold and moist. This can be

seen in Fig. 49b where all the models exhibited moist biases in the boundary layer. All five models forecasted an atmosphere that immediately dried out above the boundary layer, whereas in reality dewpoints rose with increasing temperature. This is illustrated in Fig. 49b where all models exhibited dry biases above the boundary layer. With respect to winds, the models performed reasonably well with wind direction, but struggled with wind speed (Fig. 48a-e). Once again, boundary layer winds are $2.5\text{-}7.7\text{ m s}^{-1}$ (5-15 kts) too weak in all of the models. Similar profile characteristics were observed at 1640 UTC (Fig. 50), however results should be considered with a reminder that the 1640 UTC radiosonde was launched directly into a blowing snow plume. The GFS, NAM, and NAM-3km all forecasted the temperature profile rather well, with the largest error between the three models at any level being $2.7\text{ }^{\circ}\text{C}$ (Fig. 51a). The HRRR and RAP both forecasted too cold, particularly in the boundary layer. The GFS, RAP, and HRRR had a better grasp on the moisture profile at this time, however the NAM and NAM-3km each maintained significant moist biases, particularly around 925 hPa (Fig. 51b). With respect to winds, wind direction was still handled decently in all the models (Fig. 50a-e). Boundary layer wind speeds were still an issue, but the magnitude of the error decreased since observed winds began to weaken.

The final sounding of the event, launched at 1945 UTC, coincided with a decrease of wind speed and blowing snow, which is expected to work in the favor of NWP results. Being at the tail end of the event with surface blowing snow mostly subsided over Grand Forks, it is expected that the models should be more accurate since blowing snow is not parameterized operationally. A comparison of the observed sounding versus each of the model soundings is presented in Fig. 52. The GFS, HRRR, and RAP had the boundary layer too deep, but temperatures within the boundary layer were not far off with errors of less than $2\text{ }^{\circ}\text{C}$ (Fig. 53a). Conversely, the NAM and NAM-3km forecasted the boundary layer depth well but forecasted the boundary layer to be too warm.

The GFS, HRRR, and RAP had a decent grasp for the moisture content of the profile, and the NAM and NAM-3km continued to maintain moist biases. With respect to winds, all models performed better with boundary layer wind speeds, but deviation of wind direction became apparent with models favoring a north-northwest wind.

4.4.3. Discussion

The absence of blowing snow in numerical models raises key issues regarding simulation of the boundary layer including the thermodynamic evolution and associated radiative energy budgets (Barral et al. 2014). First, it has been observed that drifting and blowing snow suppresses net longwave radiative cooling at the surface due to increased extinction (Yamanouchi and Kawaguchi 1985). Since blowing snow is not actively parameterized in operational models, these radiative effects are not simulated, and the radiation budget cannot be accurately forecasted (Barral et al. 2014; Yang et al. 2020). Second, a lack of blowing snow in the models affects the simulated moisture distribution in the boundary layer. Blowing snow sublimation will cause the lower atmosphere to become more saturated. Models without blowing snow parameterizations, in turn, suffer a systematic dry bias, affecting the energy budget (Barral et al. 2014). Both of these impacts can then negatively impact temperature forecasts.

Relating these ideas to the present study, nearly all of the models exhibited a consistent cold bias throughout the event, a positive moisture bias in the boundary layer, and a negative moisture bias just above the boundary layer after the frontal passage. It is questionable if the cold biases are due to any effect from too much radiative cooling in the models, or if the models were too forward with cold air advection. The moist biases seen in the models conflict with past research, where dry biases would be expected due to the lack of sublimation from blowing snow.

It is not immediately clear from the thermodynamic diagrams why these models favored more saturated boundary layers in the absence of blowing snow, even later in the event when falling snow was not available to saturate the profile. A likely explanation is that the moist biases are simply by-products of the cold biases. Nonetheless, it is a topic of future research to determine which model boundary layer processes are responsible for these biases, if any are responsible.

Determining optimal methods of parameterizing blowing snow has received traction since the 1990s with promising results in recent years. Letcher et al. (2021) used the Weather Research and Forecasting model (WRF) to re-forecast the 24 February 2019 Northern Plains ground blizzard, using data from Kennedy and Jones (2020) as verification. Blowing snow was parameterized as a two-step process: saltation, and turbulent suspension of particles. Coupled with the assumption of a gamma particle size distribution, model visibility was tested during the event. Satellite and ASOS data were used to verify the model output. It was found that the simple blowing snow parameterization offered greater accuracy in visibility forecasting, which can aid forecasters in determining areas that would be at risk for blowing snow. The authors noted a key limitation to their method that also holds true for other methods. Model verification can become difficult, which can make measuring model accuracy a challenge. It was noted that ASOS stations during this event significantly under-reported blowing snow, often classifying it as other hazards such as haze or freezing fog. As ASOS stations are the only source of ground data in many parts of the country, inaccurate observations pose challenges to model verification. Additionally, as discussed by Kennedy and Jones (2020), the visualization of blowing snow using satellites with near-infrared channels is dependent on clear skies and daylight, making observations and verification with cloudy skies or at nighttime impossible.

It is important to note that Letcher et al. (2021) focused on only visibility forecasting.

Impacts on radiation or energy flux forecasting were not discussed, as the scheme was decoupled from the other parameterizations. The author is unaware of other research that used the same method to evaluate such fluxes. Additionally, it is not clear which current operational model parameterizations negatively affected these fluxes in the present study. A future modelling study further testing parameterization and the effects on radiation and energy fluxes could prove useful in identifying model deficiencies.

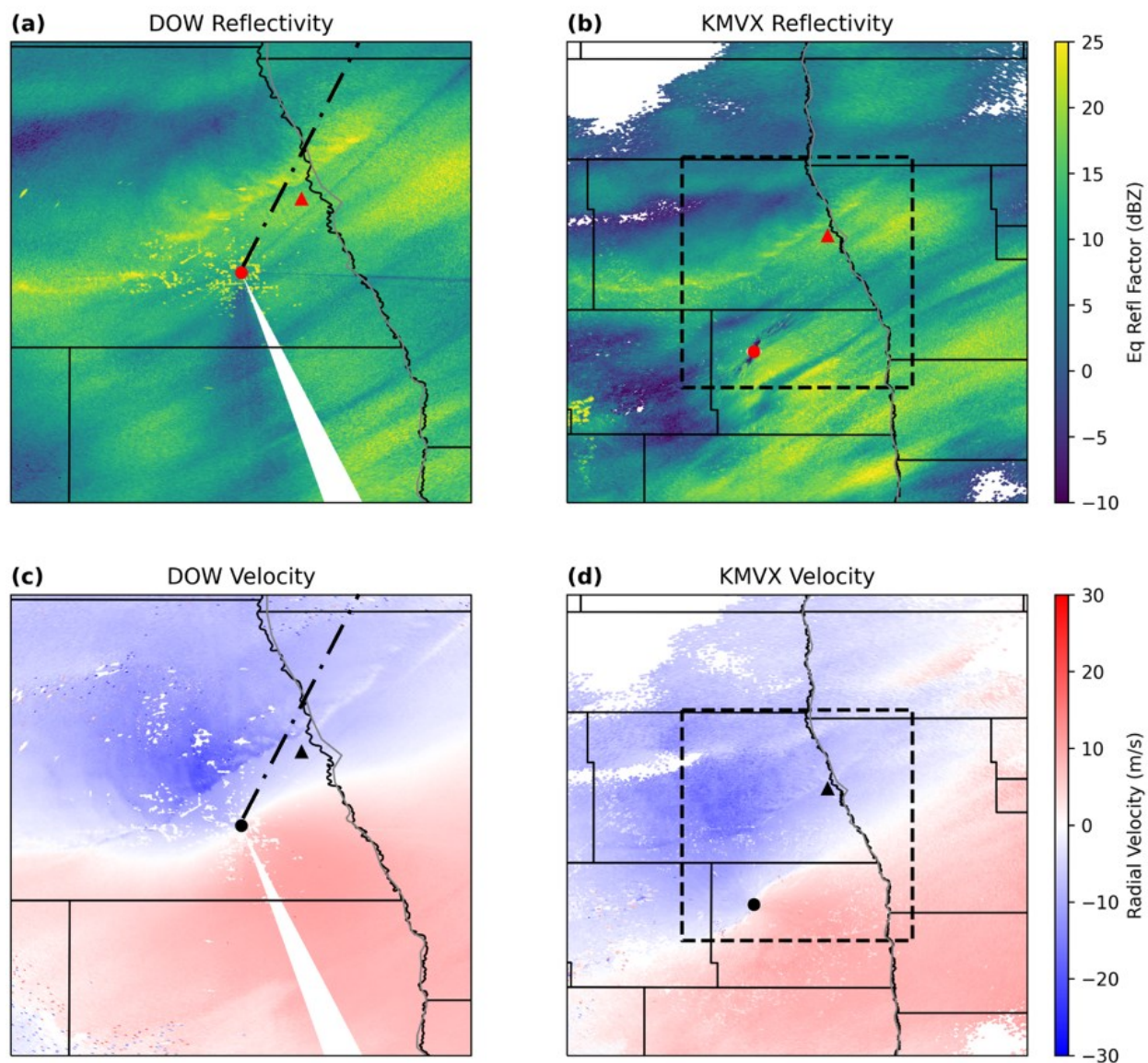


Figure 16 – Radar imagery from DOW7 at 0720 UTC and KMVX at 0721 UTC. The DOW7 elevation angle is 1.3° and the KMVX elevation angle is 0.5° . Panels (a) and (c) show DOW7 reflectivity and velocity, respectively. Panels (b) and (d) show KMVX reflectivity and velocity, respectively. The black dashed boxes in (b) and (d) denote the domain used in (a) and (c), respectively. The circles in each panel indicate the locations of the centers of the respective radars. The triangles in each panel indicate the location of Grand Forks, ND. The dot-dashed black lines in (a) and (c) denote the azimuthal angle used in the RHI plots in Fig. 22.

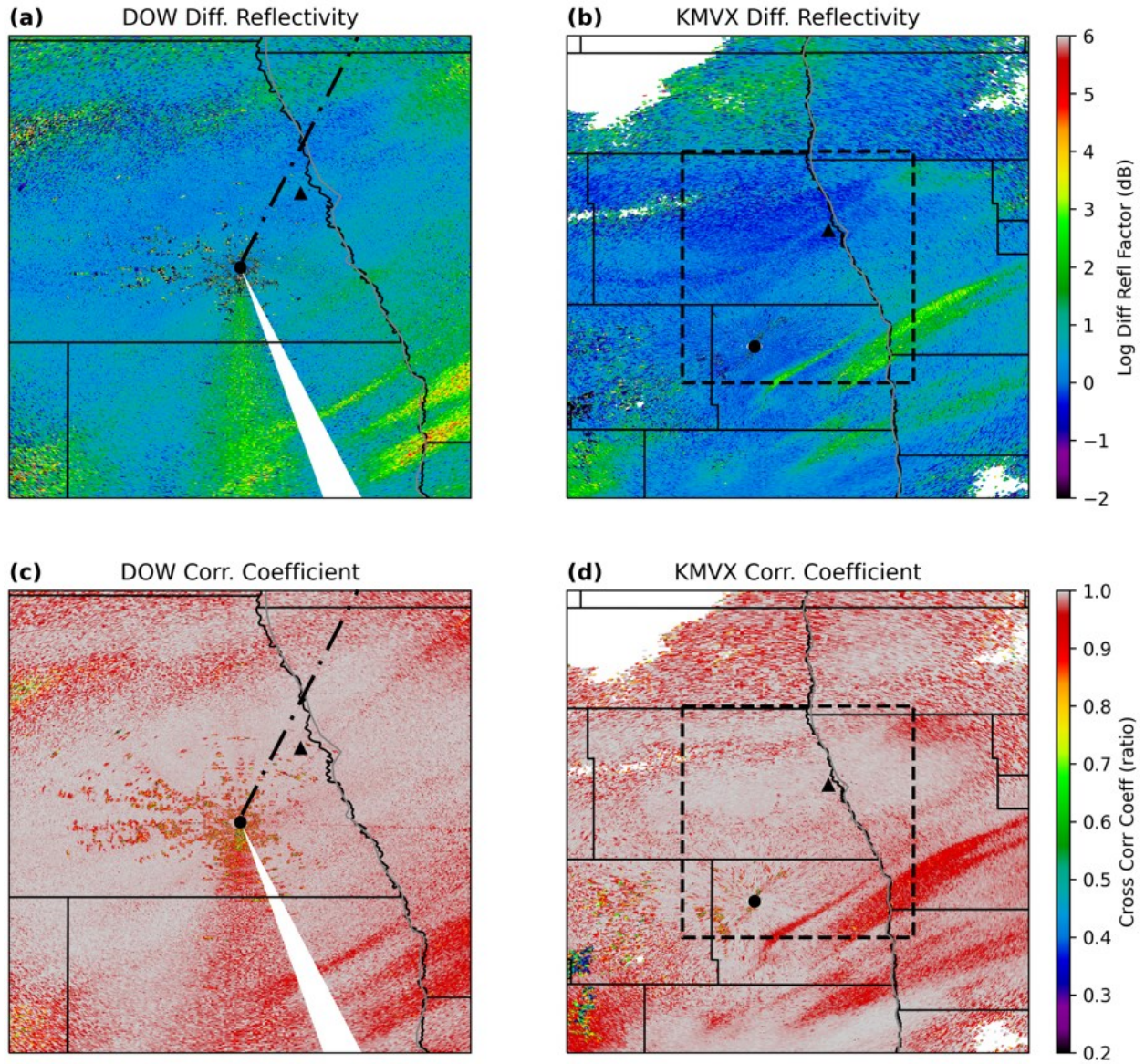


Figure 17 – As in Fig. 16, except for (a) DOW7 differential reflectivity, (b) KMOVX differential reflectivity, (c) DOW7 correlation coefficient, and (d) KMOVX correlation coefficient.

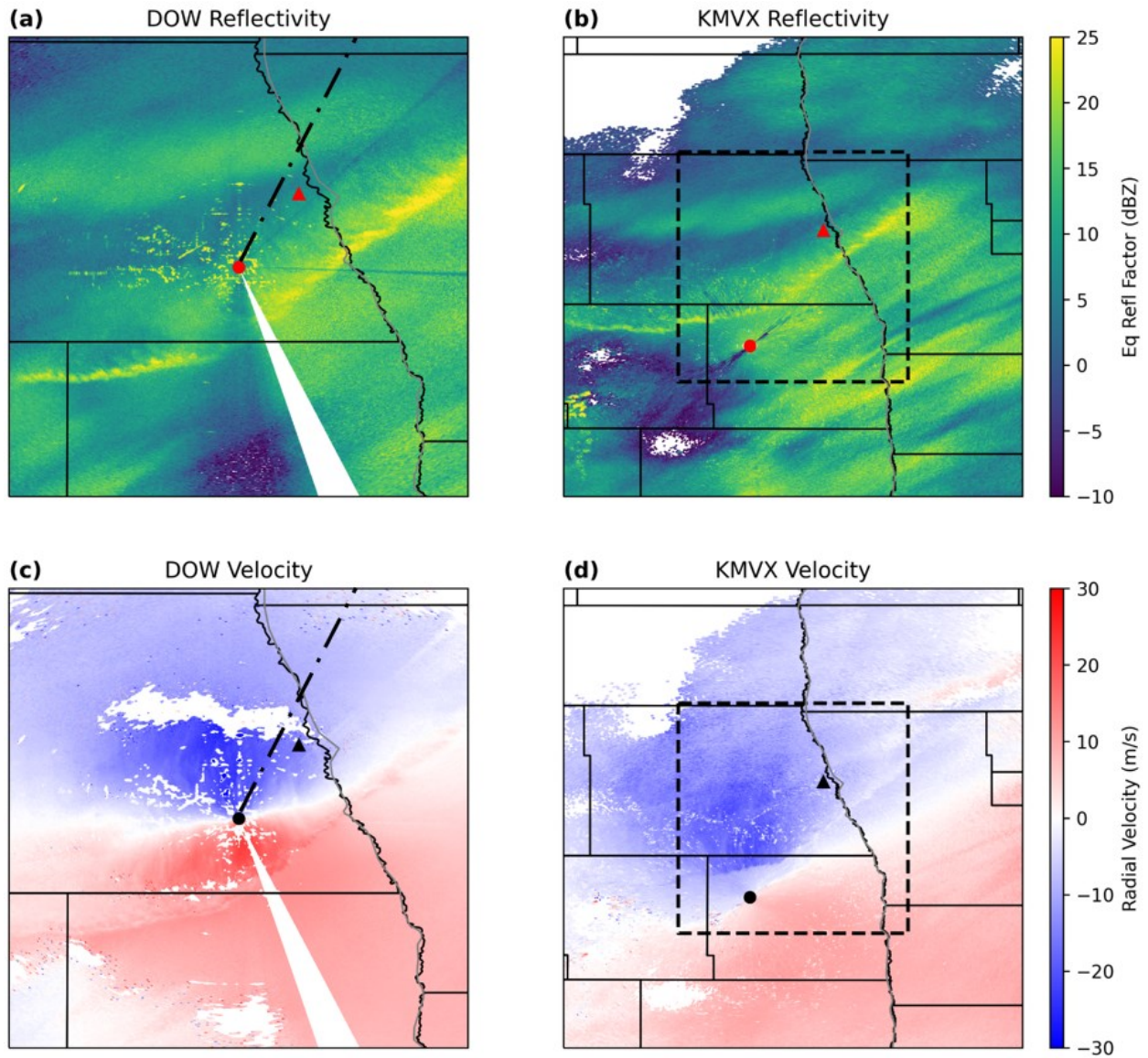


Figure 18 – As in Fig. 16, except for DOW7 data at 0740 UTC and KMVX data at 0738 UTC.

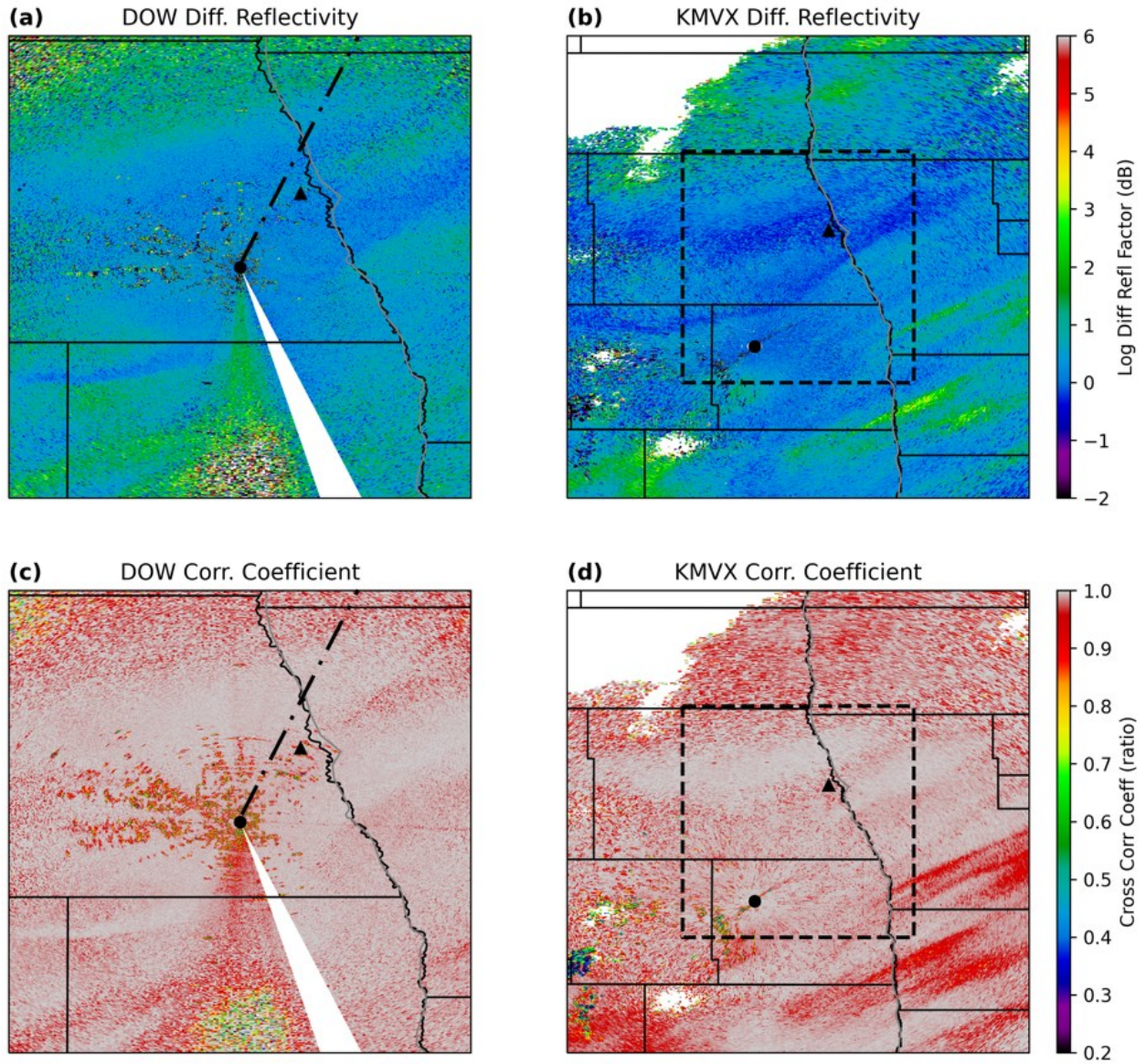


Figure 19 – As in Fig. 17, except for DOW7 data at 0740 UTC and KMOVX data at 0738 UTC.

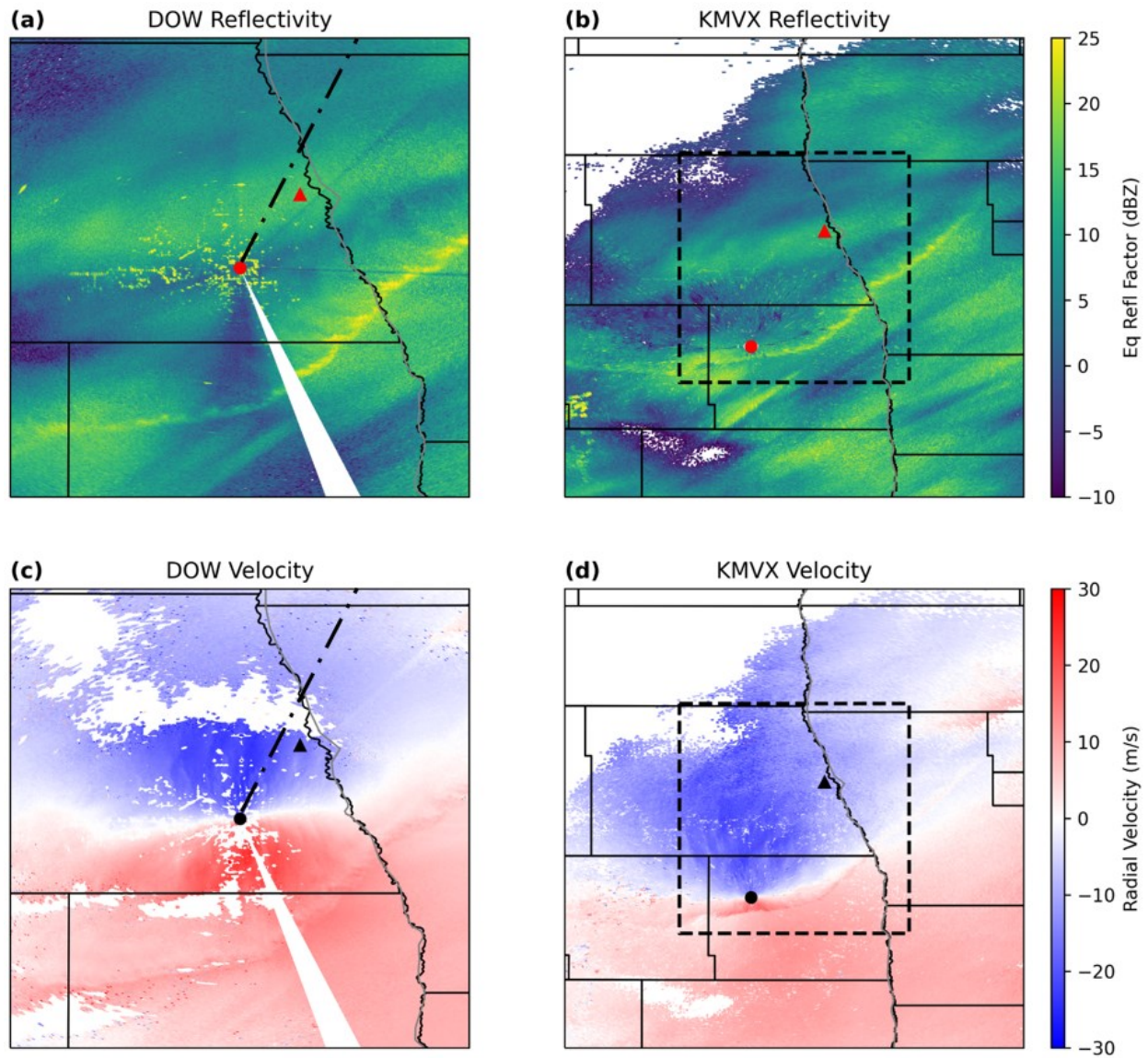


Figure 20 – As in Fig. 16, except for DOW7 data at 0752 UTC and KMXV data at 0756 UTC.

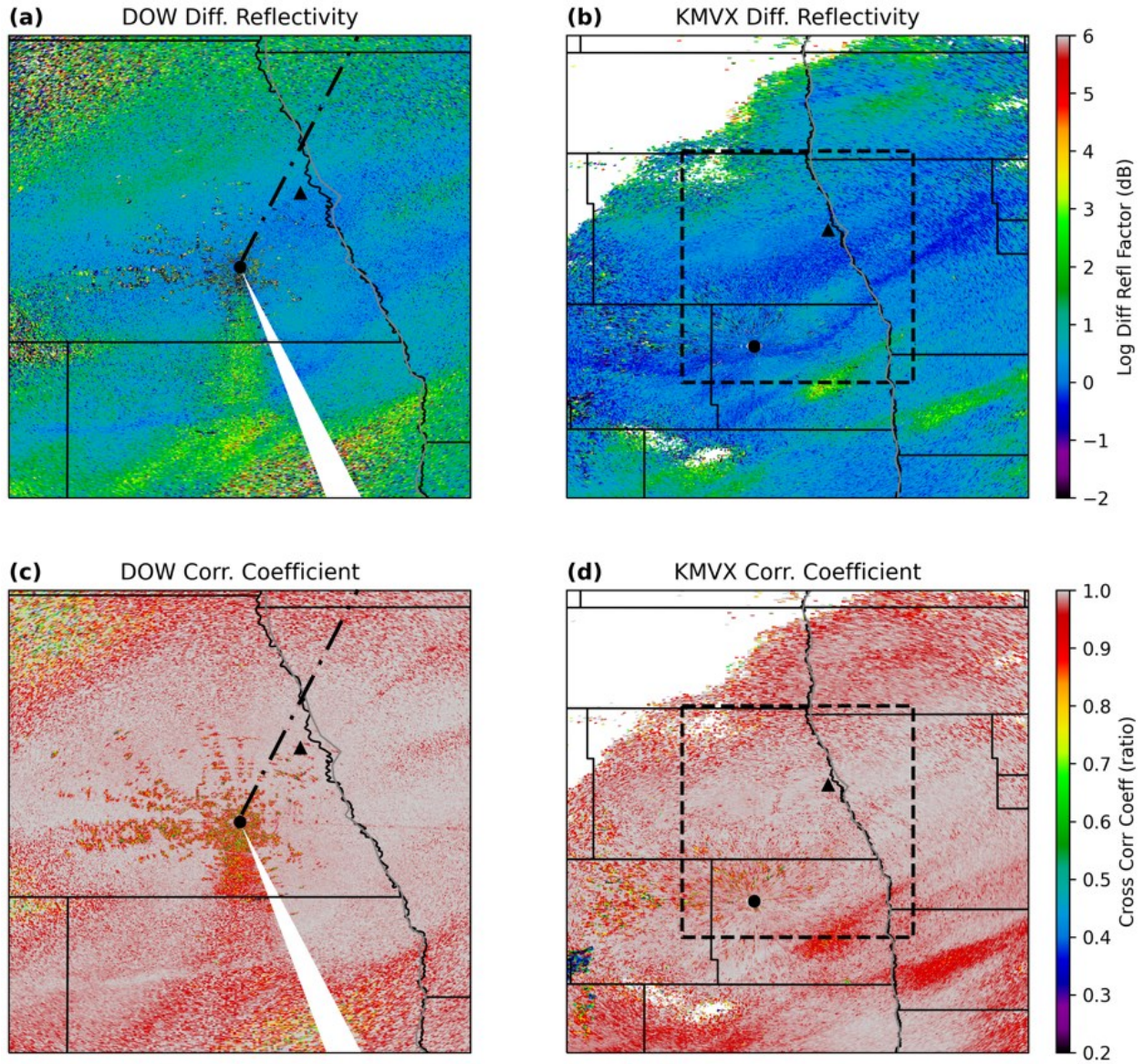


Figure 21 – As in Fig. 17, except for DOW7 data at 0752 UTC and KMXV data at 0756 UTC.

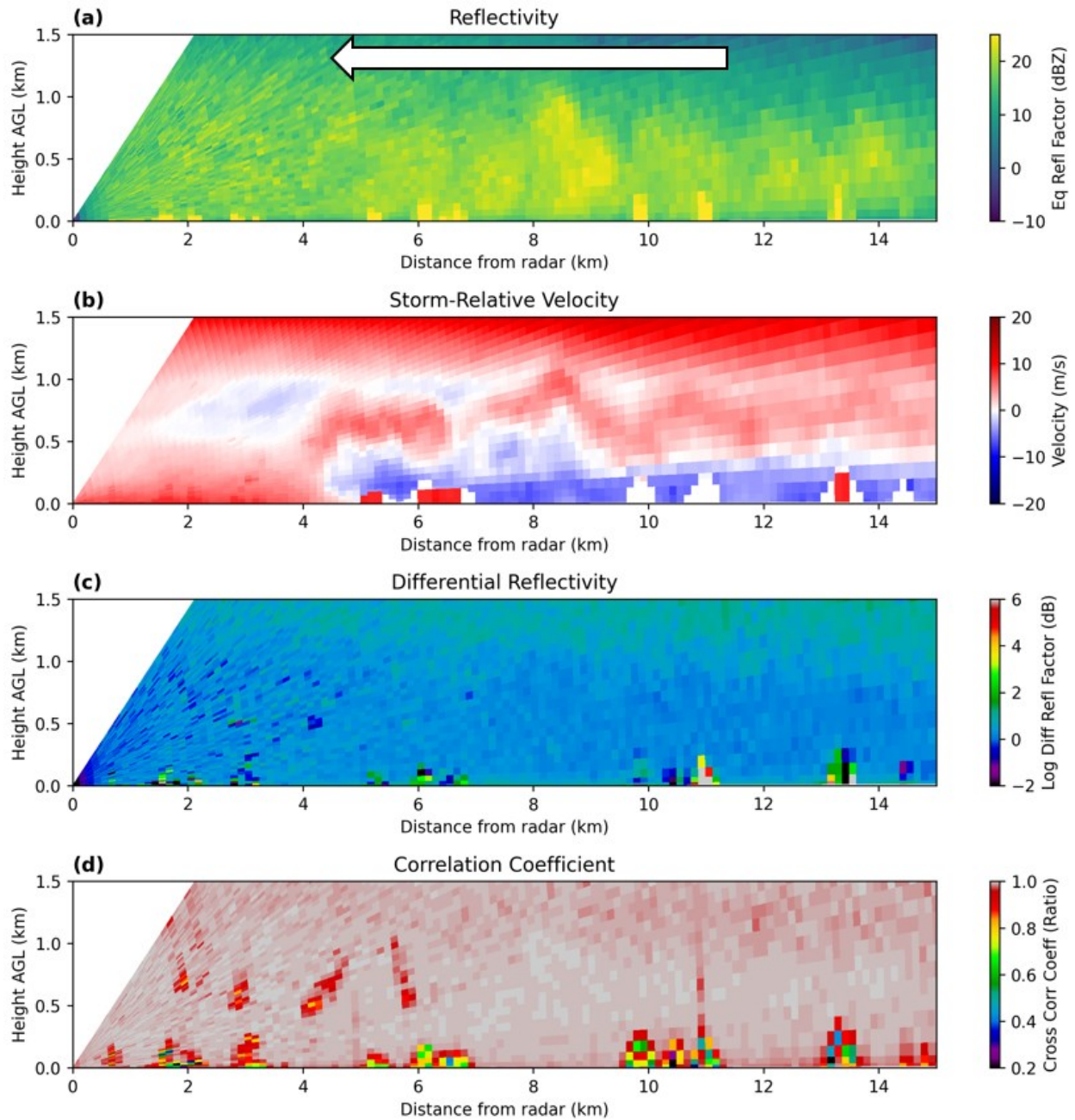


Figure 22 – DOW7 RHI (a) reflectivity, (b) storm-relative velocity, (c) differential reflectivity, and (d) correlation coefficient observed at 0728 UTC at an azimuthal angle of 27.5° with respect to north. The white arrow in (a) indicates the direction the front was moving with respect to the radar.

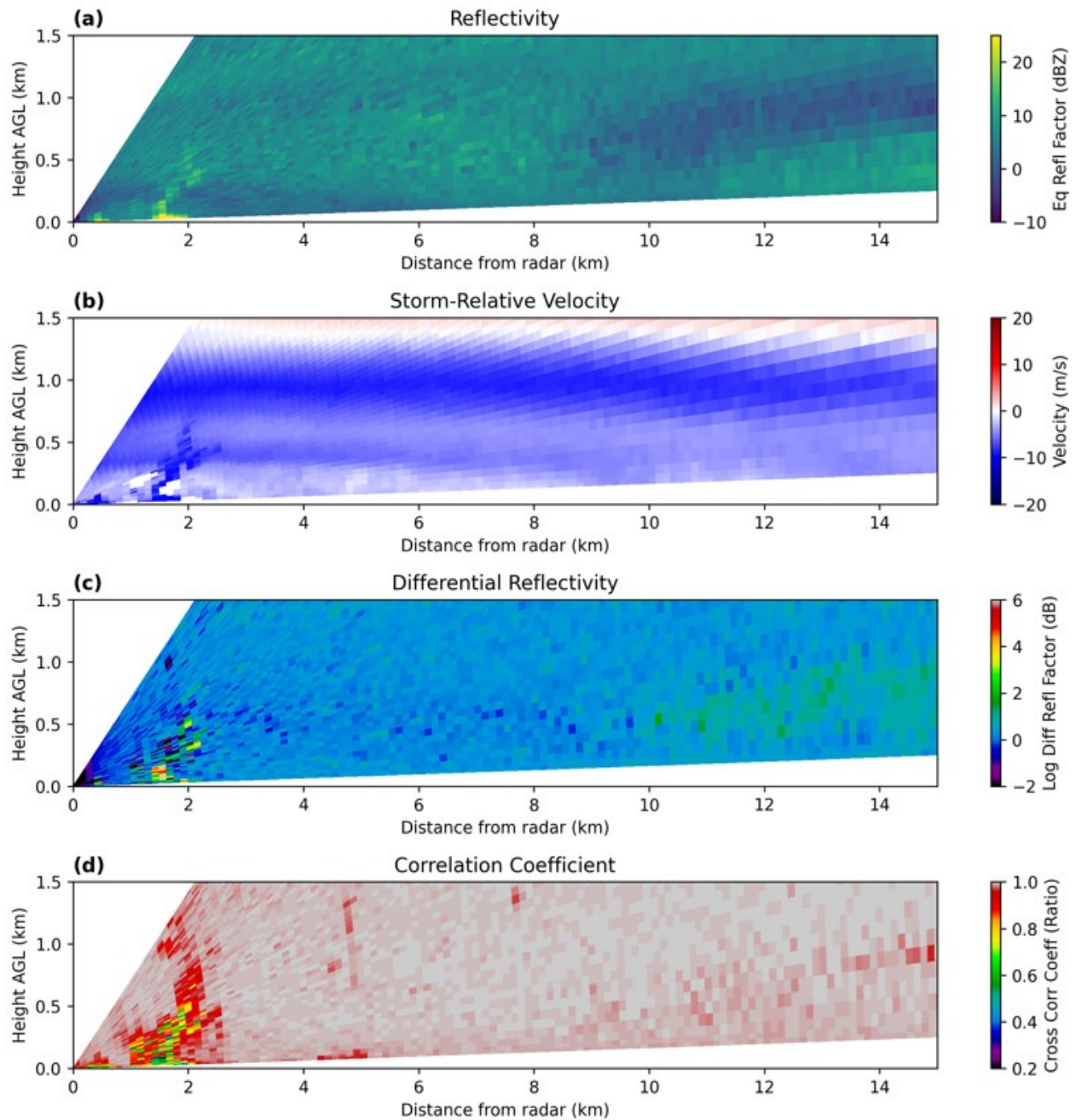


Figure 23 – DOW7 RHI (a) reflectivity, (b) storm-relative velocity, (c) differential reflectivity, and (d) correlation coefficient observed at 0755 UTC at an azimuthal angle of 100° with respect to north.

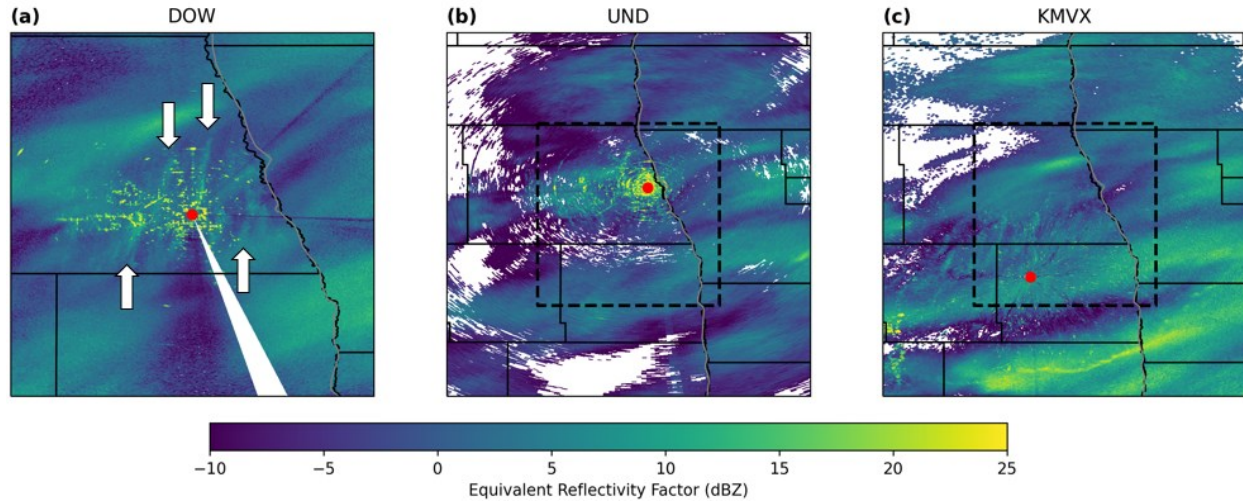


Figure 24 – Radar reflectivity observations at 0840 UTC for (a) DOW7 (1.3°), (b) UND NorthPol (2.0°), and (c) KVVX at (0.5°). The red dots in each panel indicate the locations of each of the respective radars. The black dashed boxes in (b) and (c) denotes the domain of panel (a). The white arrows in panel (a) point out a few of the blowing snow plumes seen by DOW7.

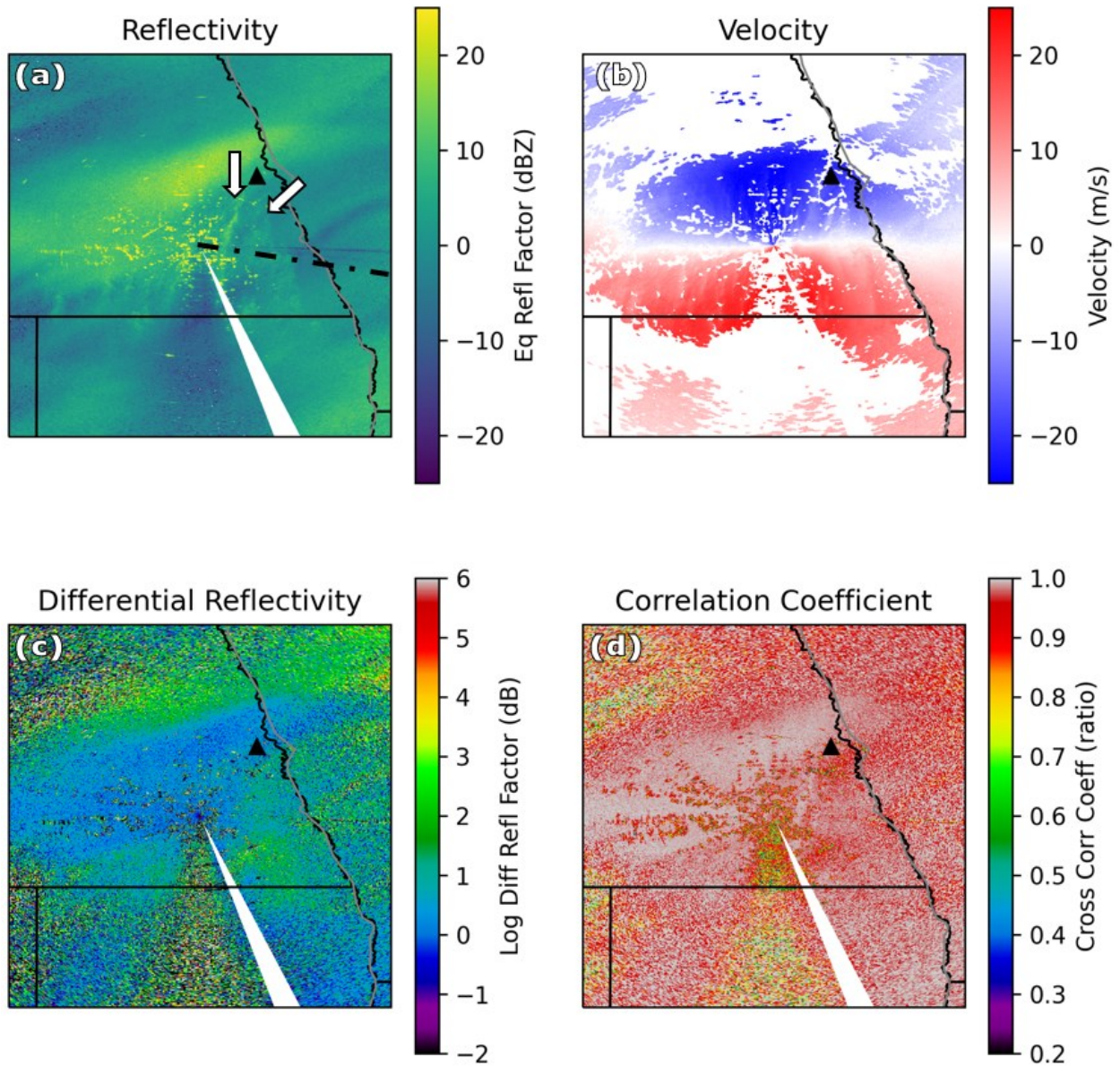


Figure 25 – DOW7 PPI (a) reflectivity, (b) radial velocity, (c) differential reflectivity, and (d) correlation coefficient observed at 0852 UTC at an elevation angle of 1.3°. The black triangles in each panel indicate the location of Grand Forks, ND. The white arrows in (a) point out a couple of the blowing snow plumes investigated in RHI imagery in Fig. 26.

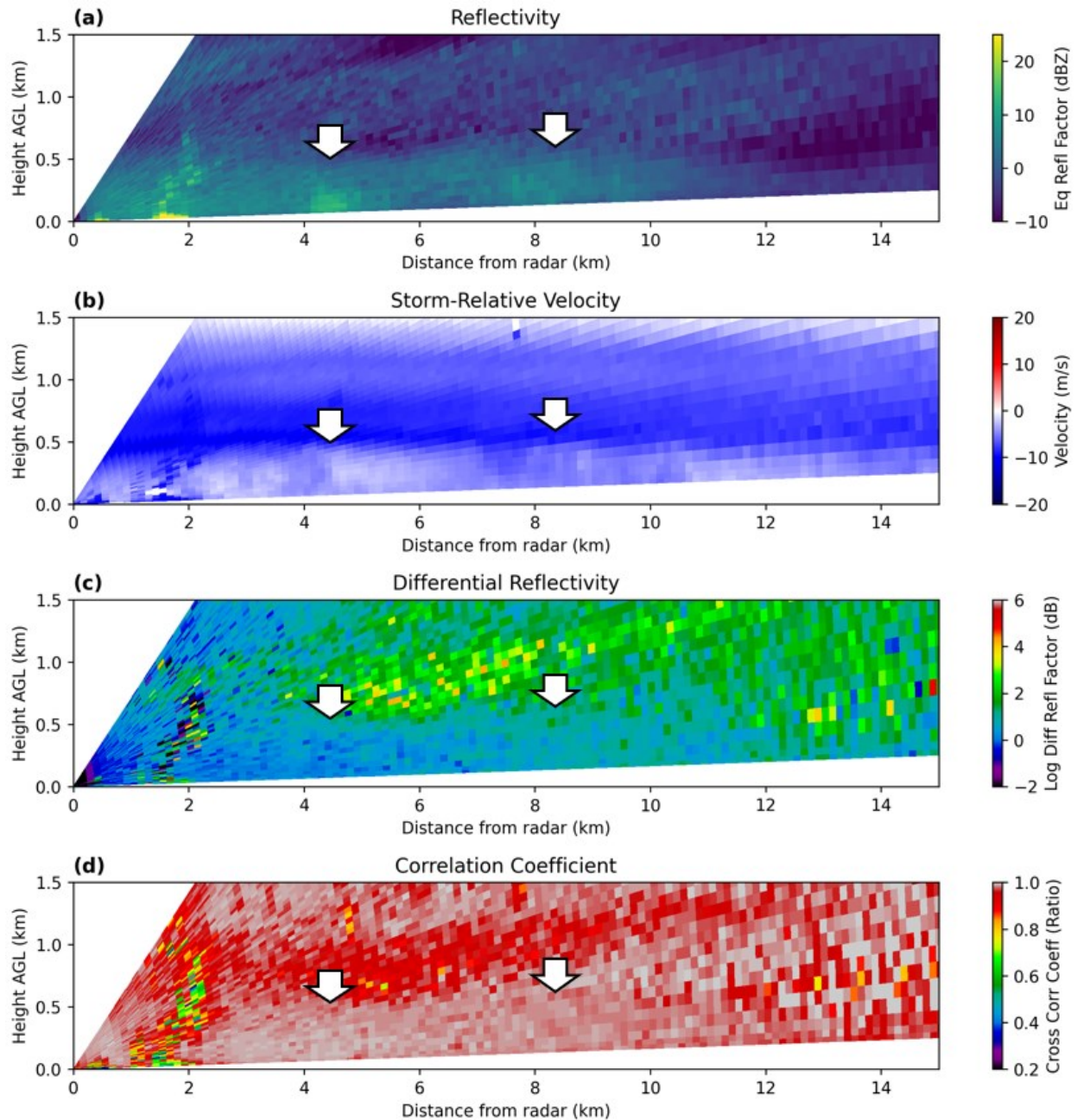


Figure 26 – DOW7 RHI (a) reflectivity, (b) storm-relative velocity, (c) differential reflectivity, and (d) correlation coefficient observed at 0855 UTC at an azimuthal angle of 100° with respect to north. The white arrow in (a) indicates the locations of the chosen blowing snow plumes from Fig. 25.

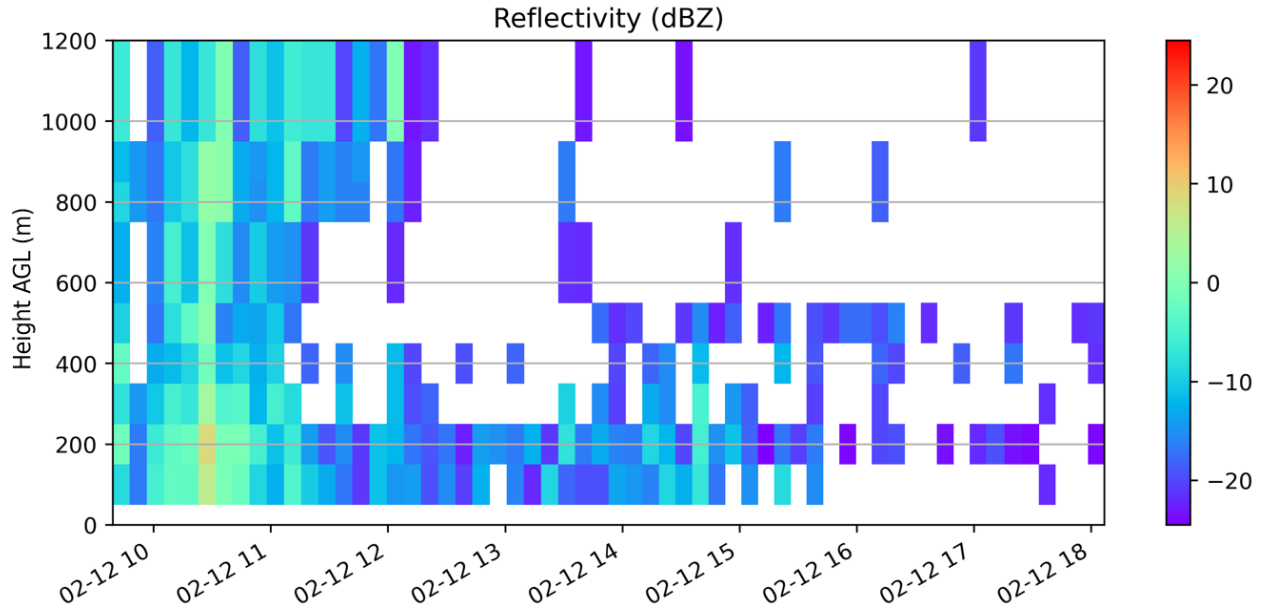


Figure 27 – A time-height series of KMVX radar reflectivity near 47.61°N, 97.34°W approximately 12.8 km (8 miles) north-northwest of KMVX. The radar reflectivity for the bin closest to this point is plotted for every available volume scan.

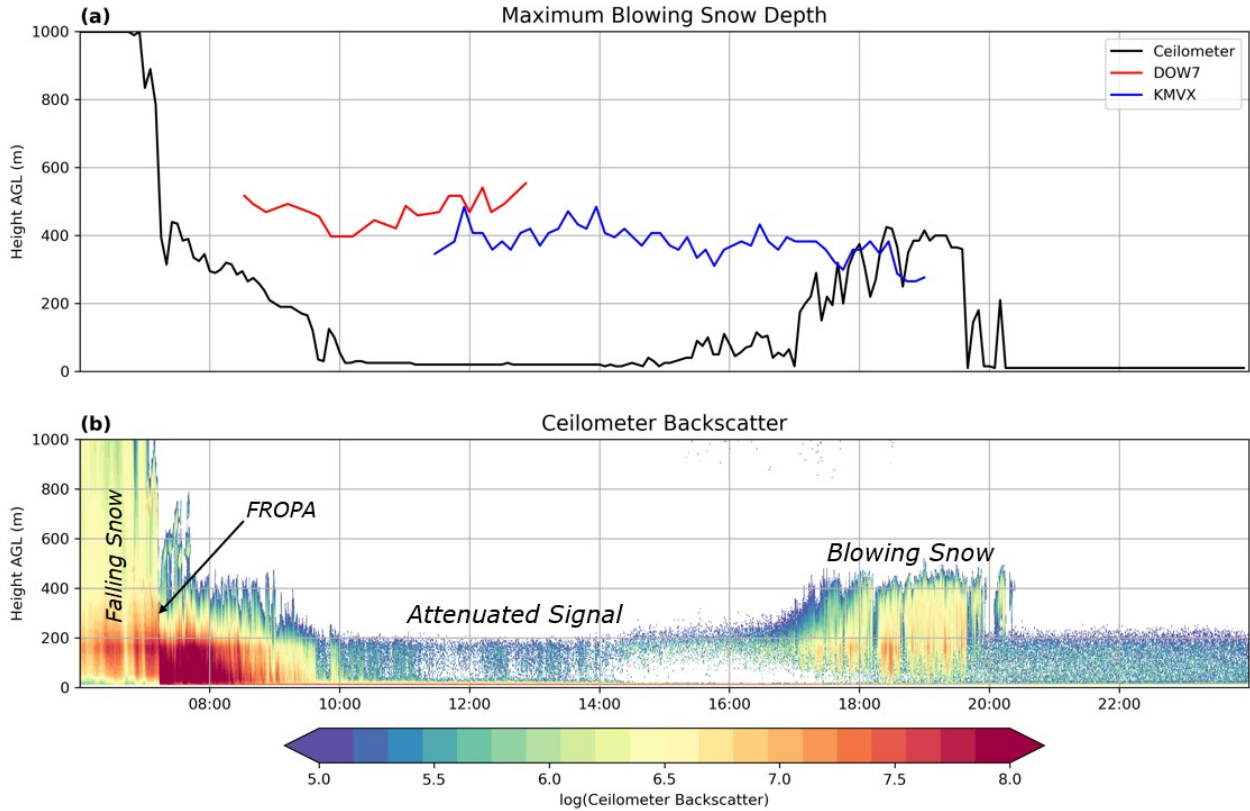


Figure 28 – Panel (a) shows the maximum blowing snow depth as measured with the Lufft ceilometer averaged every 5 minutes (black line), DOW7 (red line), and KMVX (blue line) from 0600 to 2400 UTC on 12 Feb 2020. Panel (b) shows the corresponding ceilometer for the same time period. Times with falling and blowing snow are annotated in (b), in addition to the frontal passage (“FROPA”) and when the signal was attenuated.

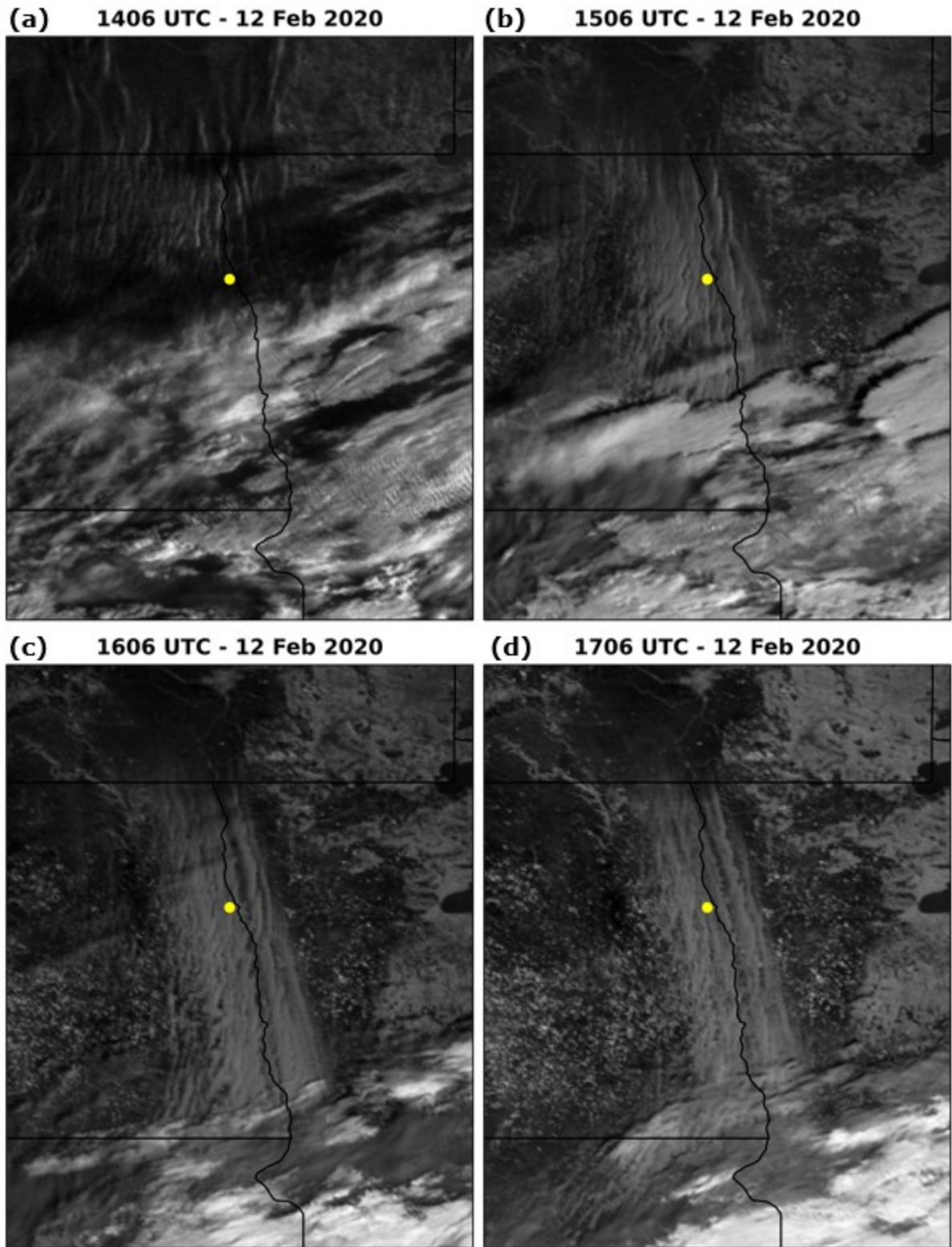
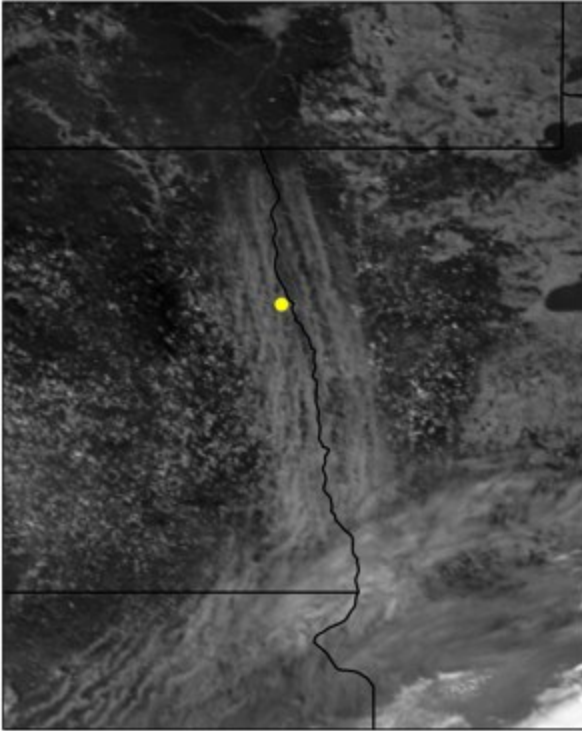
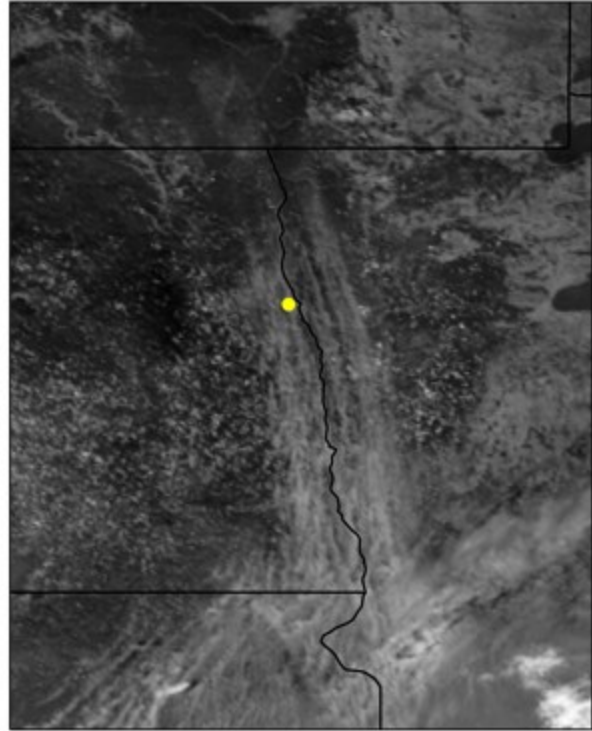


Figure 29 – *GOES-16* imagery from the 1.63- μm band (band 5) at (a) 1406 UTC, (b) 1506 UTC, (c) 1606 UTC, and (d) 1706 UTC on 12 Feb 2020. The yellow dot indicates Grand Forks, ND.

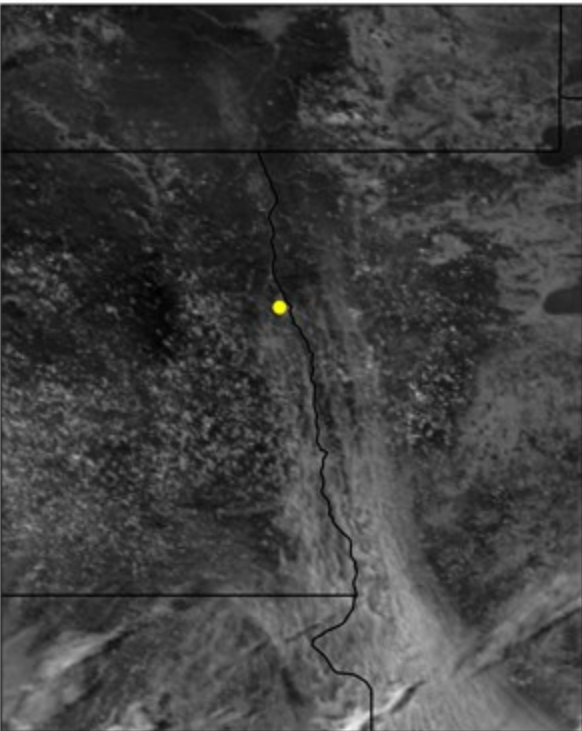
(a) 1806 UTC - 12 Feb 2020



(b) 1906 UTC - 12 Feb 2020



(c) 2006 UTC - 12 Feb 2020



(d) 2106 UTC - 12 Feb 2020

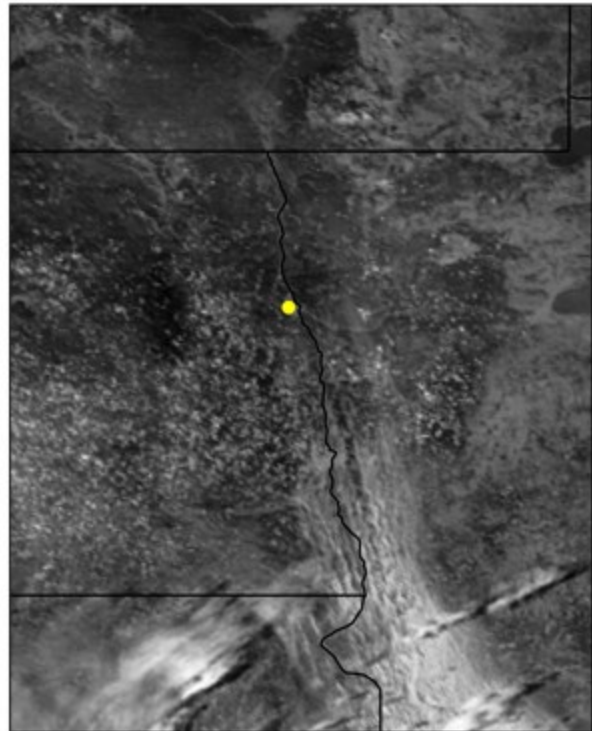


Figure 30 – As in Fig. 29, except for (a) 1806 UTC, (b) 1906 UTC, (c) 2006 UTC, and (d) 2106 UTC on 12 Feb 2020.

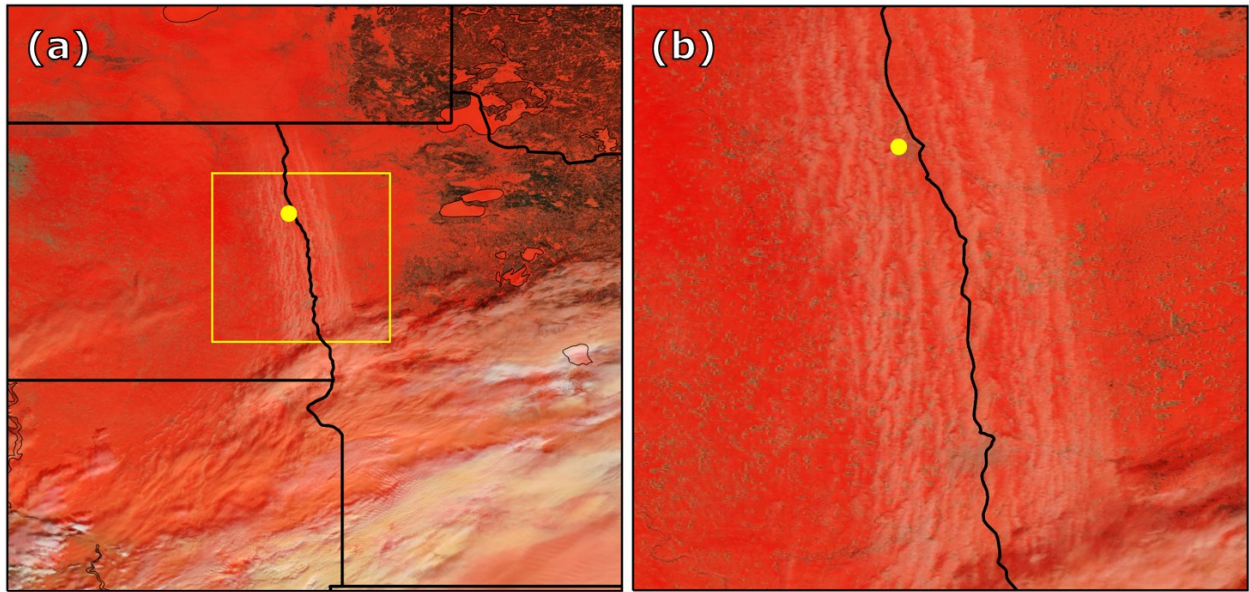


Figure 31 – Imagery from the MODIS instrument aboard NASA’s *Terra* satellite collected around 1700 UTC on 12 Feb 2020 using the 0.45- μm , 1.628- μm , and 2.105- μm bands. The yellow box in panel (a) indicates the domain of panel (b). The yellow dot in each panel denotes the location of Grand Forks, ND.

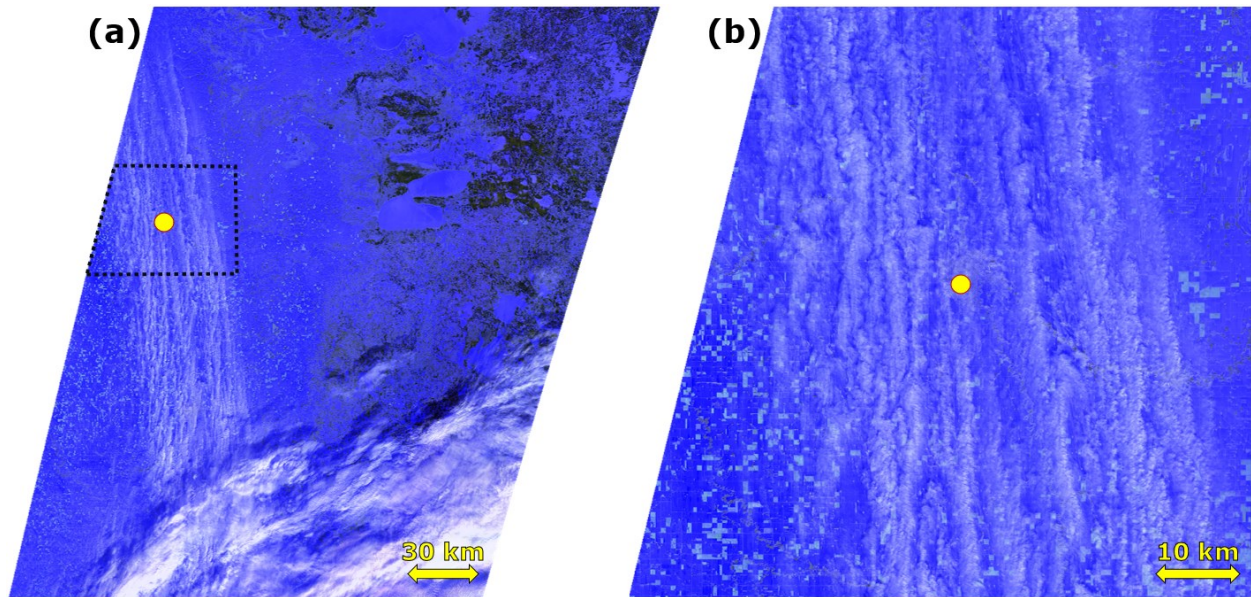


Figure 32 – Imagery from *Sentinel-2* at 1730 UTC on 12 Feb 2020 using the 0.665- μm , 1.614- μm , and 2.202- μm bands. The black dashed polygon in panel (a) indicates the domain of panel (b). The yellow dot in each panel denotes the location of Grand Forks, ND.

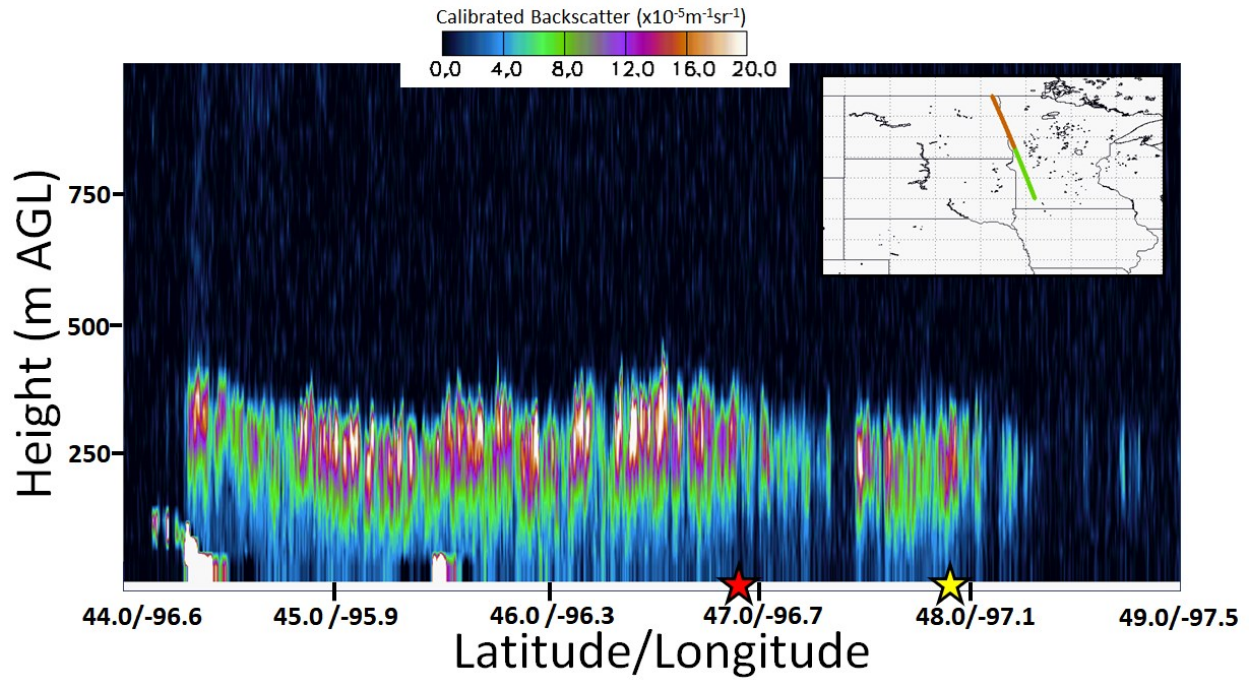


Figure 33 – The CALIOP 532-nm calibrated, attenuated backscatter observed along the path denoted in the subplot in the upper-right. The red and yellow stars denote the approximate locations of Fargo, ND and Grand Forks, ND, respectively. Figure courtesy of Stephen Palm.

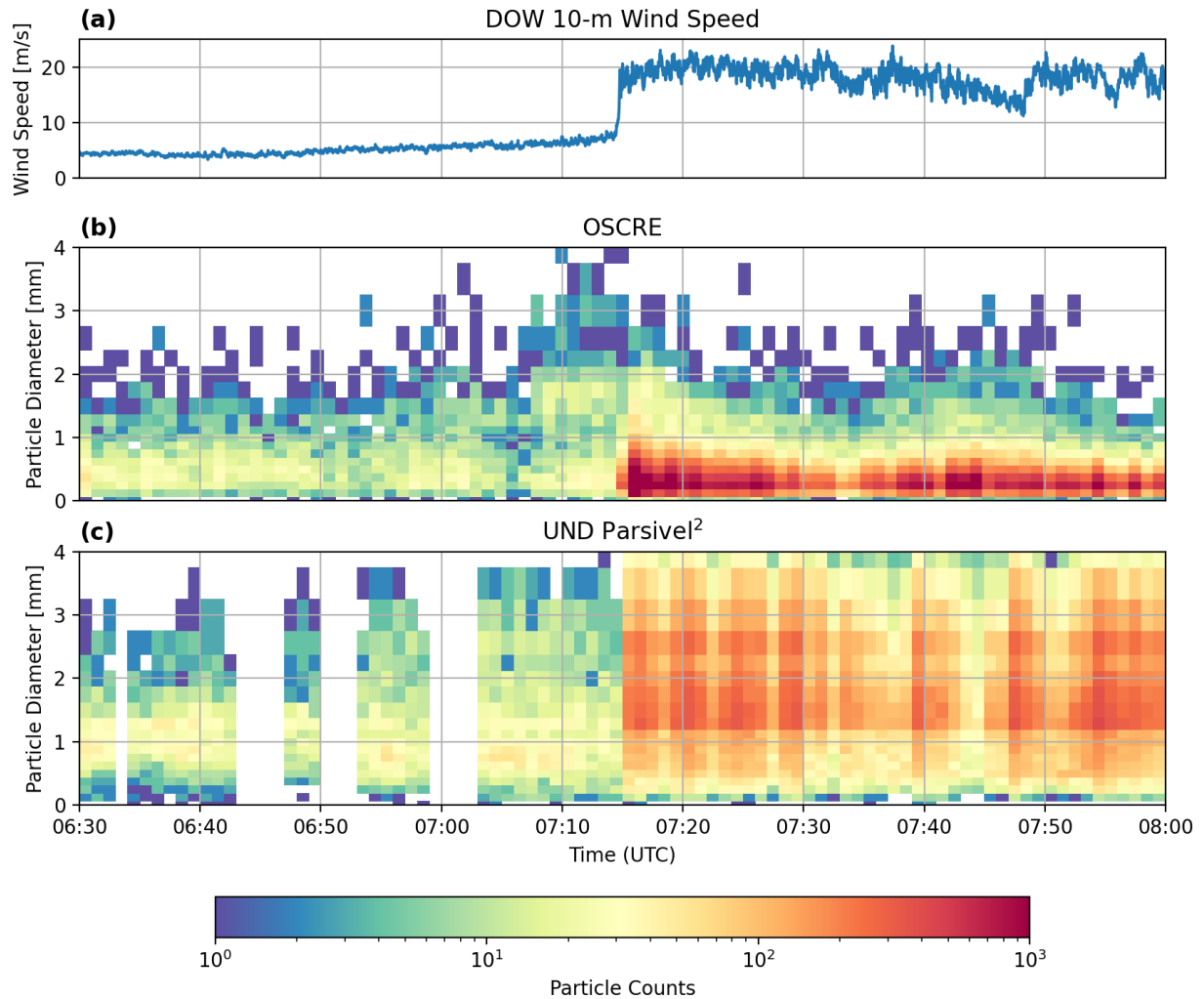


Figure 34 – (a) 10-meter wind speeds as recorded with DOW7; (b) a PSD time-series for OSCRE from 0645 to 0815 UTC, with times shifted 15 minutes into the past to match the frontal passage time recorded with the Parsivel²; (c) a PSD time-series for the Parsivel² from 0630 to 0800 UTC. Maximum particle diameter in (b) and (c) is plotted every minute in vertical bins starting at 0, 0.062, 0.187, 0.312, 0.437, 0.562, 0.687, 0.812, 0.937, 1.062, 1.187, 1.375, 1.625, 1.875, 2.125, 2.375, 2.750, 3.250, and 3.750 mm.

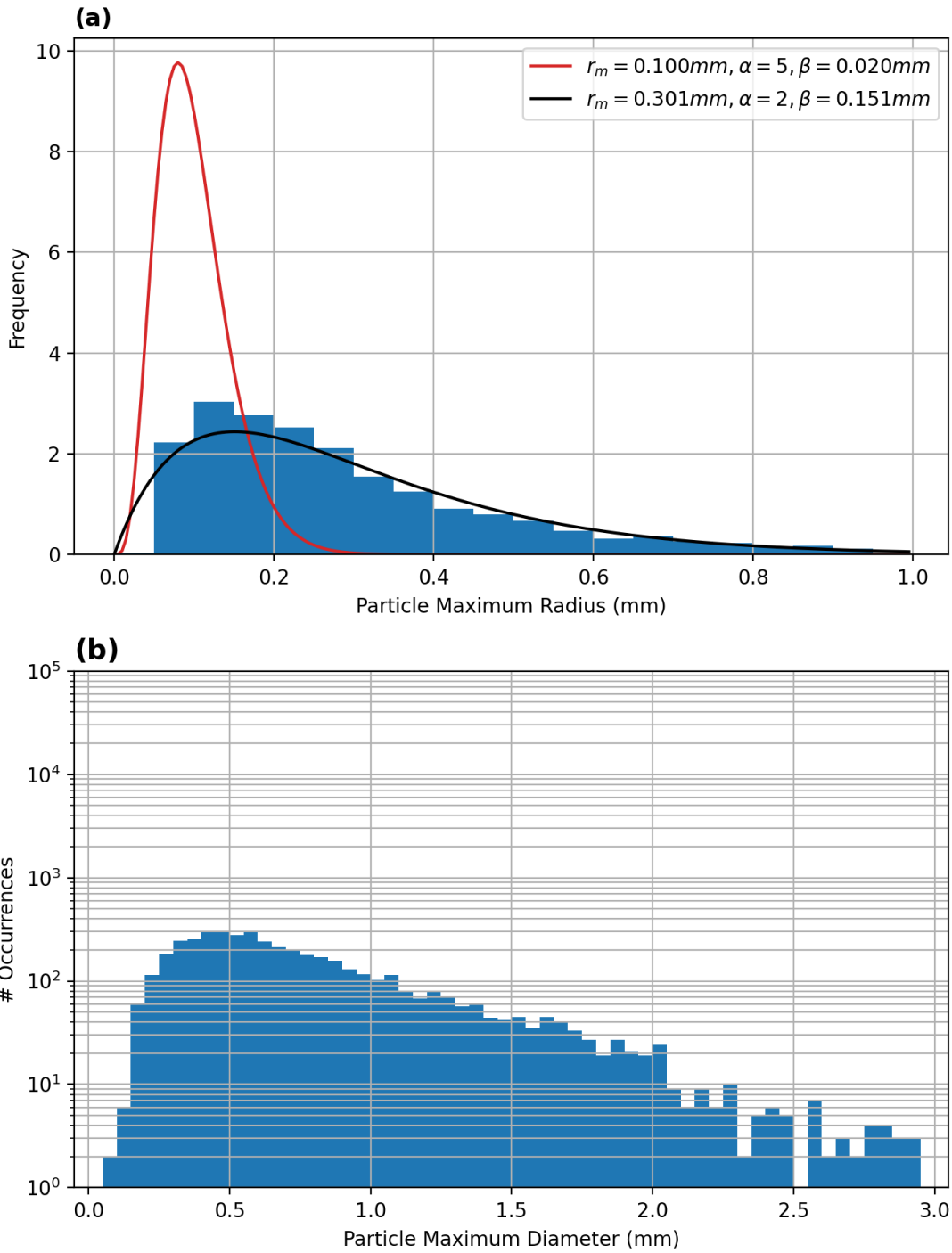


Figure 35– OSCRE particle sizes during the 45 minutes prior to the frontal passage. Plotted in (a) is a gamma distribution, where the blue bars are the particle number density, the black line is the observed gamma distribution, and the red line is the ideal gamma distribution determined by Pomerooy (1988). Plotted in (b) is a particle size distribution.

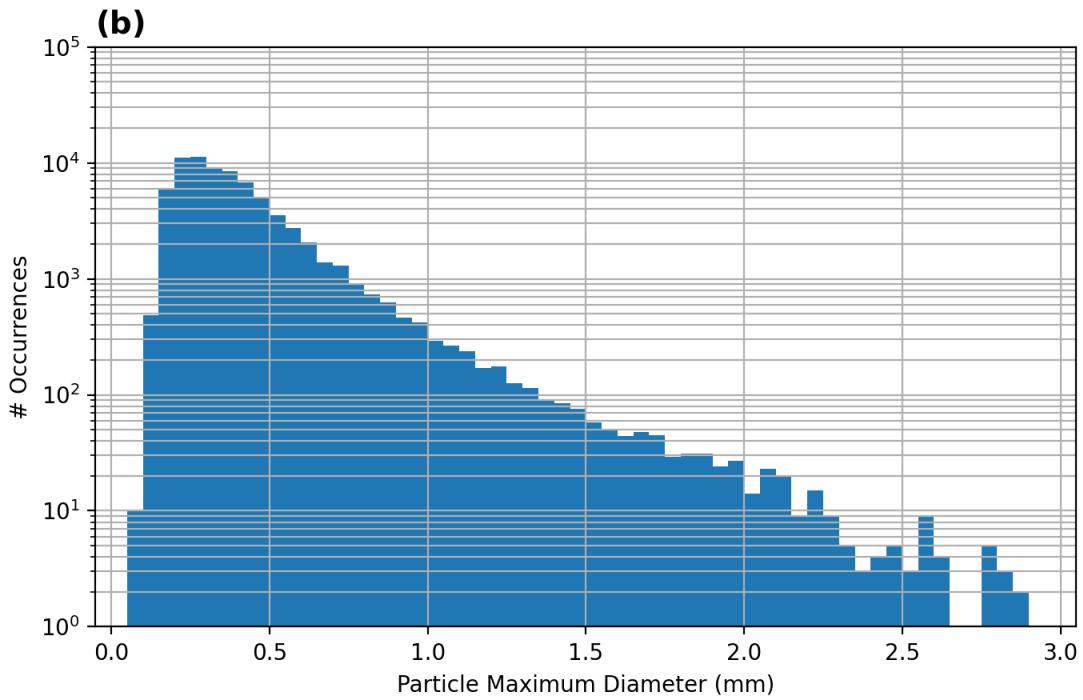
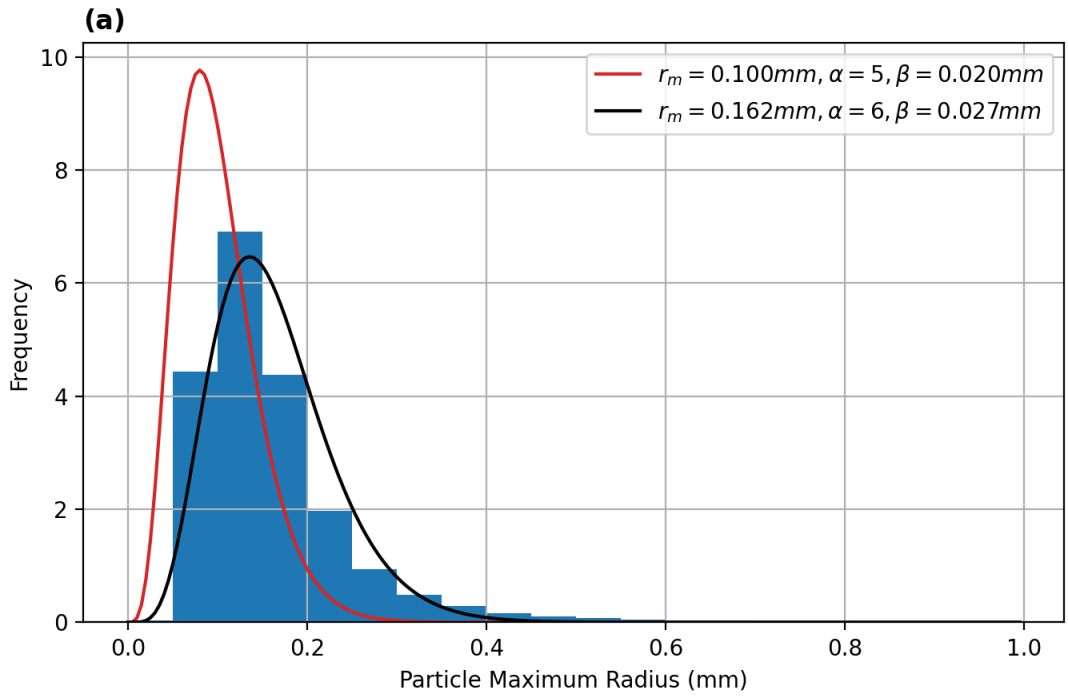


Figure 36 – As in Fig. 35 except for the 45 minutes after the frontal passage.

Table 2 – A summary of the r_{mean} , α , and β values from Pomeroy (1988), for 45 minutes before the frontal passage, and 45 minutes after the frontal passage.

	r_{mean}	α	β
Pomeroy (1988)	0.100 mm	5.0	0.020 mm
45 Minutes Before Fropa	0.301 mm	2.0	0.151 mm
45 Minutes After Fropa	0.162 mm	6.0	0.027 mm

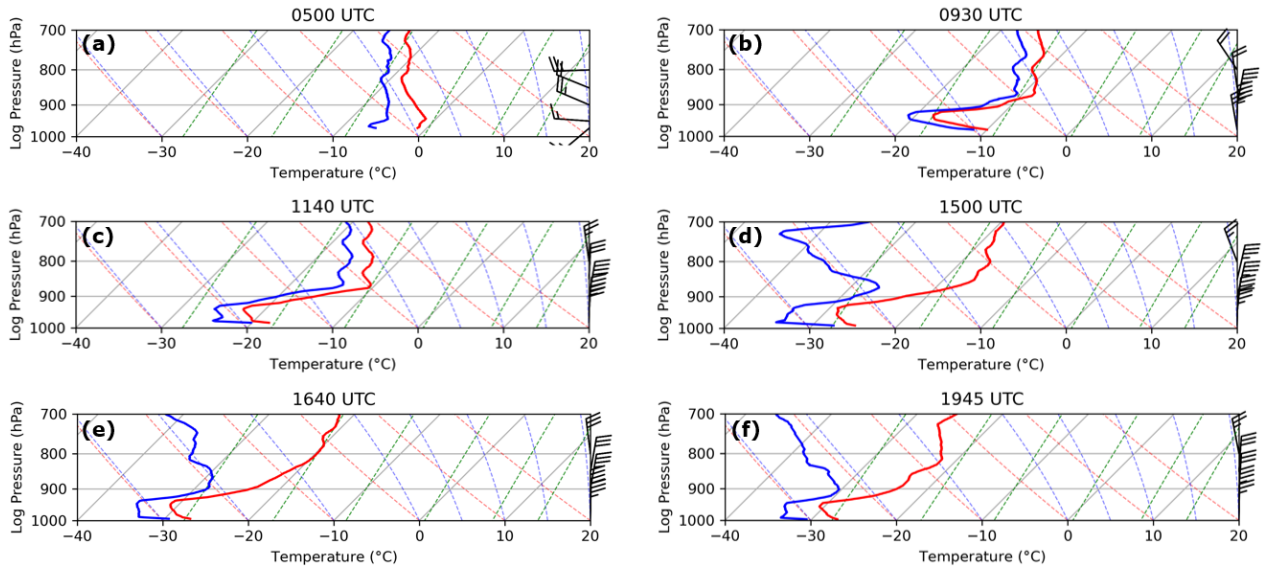


Figure 37 – Thermodynamic profiles plotted on skew- T log- p diagrams from radiosondes launched at (a) 0500 UTC, (b) 0930 UTC, (c) 1140 UTC, (d) 1500 UTC, (e) 1640 UTC, and (f) 1945 UTC.

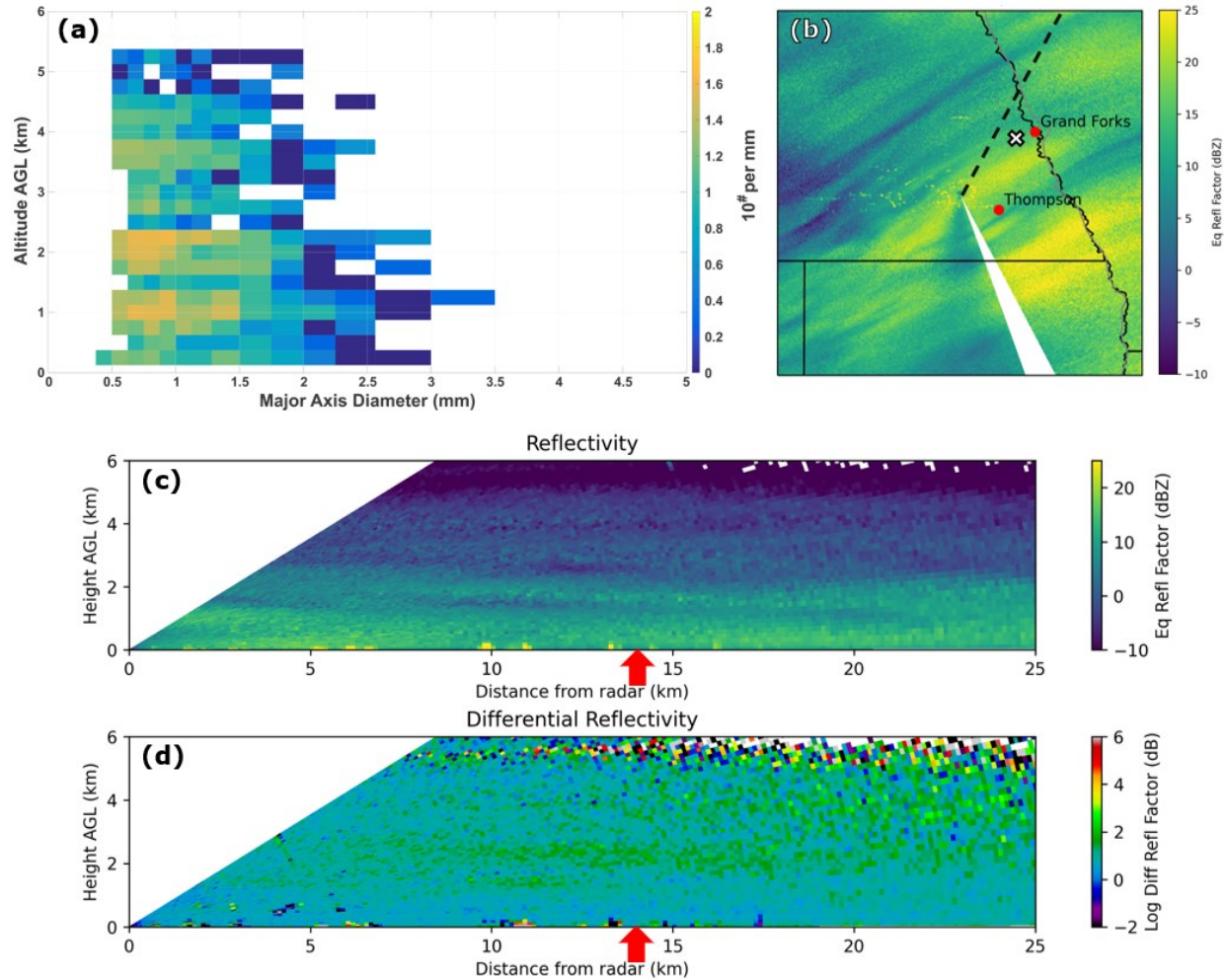


Figure 38 – (a) A PSD with respect to height for the PASIV; (b) radar reflectivity PPI observed with DOW7 at 0641 UTC at an elevation angle of 1.8°; (c) radar reflectivity RHI observed with DOW7 at 0648 UTC at an azimuthal angle of 27.5° with respect to north; and (d) radar differential reflectivity RHI observed with DOW7 at the same time and angle as (c). In panel (b), the white ‘X’ indicates the locations that the PASIV was launched from, and the dashed black line indicates the scan angle for the radar imagery in panels (c) and (d). Grand Forks, ND and Thompson, ND are indicated by red dots. In panels (c) and (d), the red arrows indicate the approximate distance away from DOW7 that the PASIV was launched. Panel (a) is courtesy of Dr. Sean Waugh at the National Severe Storms Laboratory.

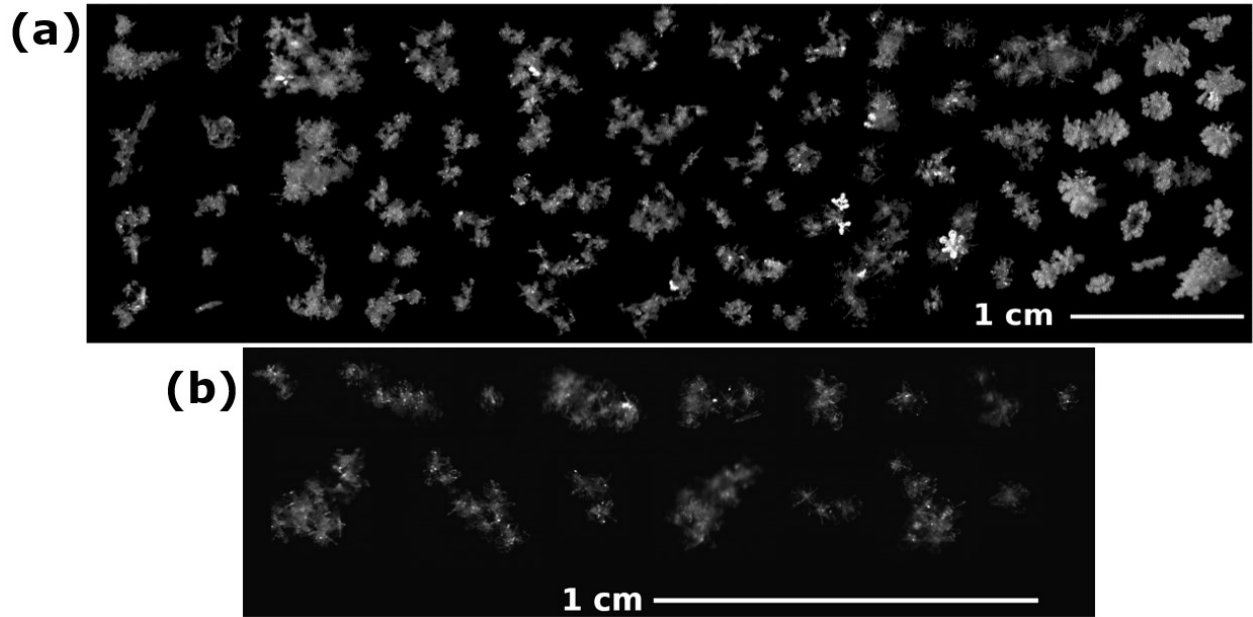


Figure 39 – Composite images of hydrometeors from OSCRE for (a) 0500 to 0730 UTC, and (b) within a 200-second window at 0645 UTC coinciding with the PASIV launch. Panel (a) is adapted from Kennedy et al. (2021).

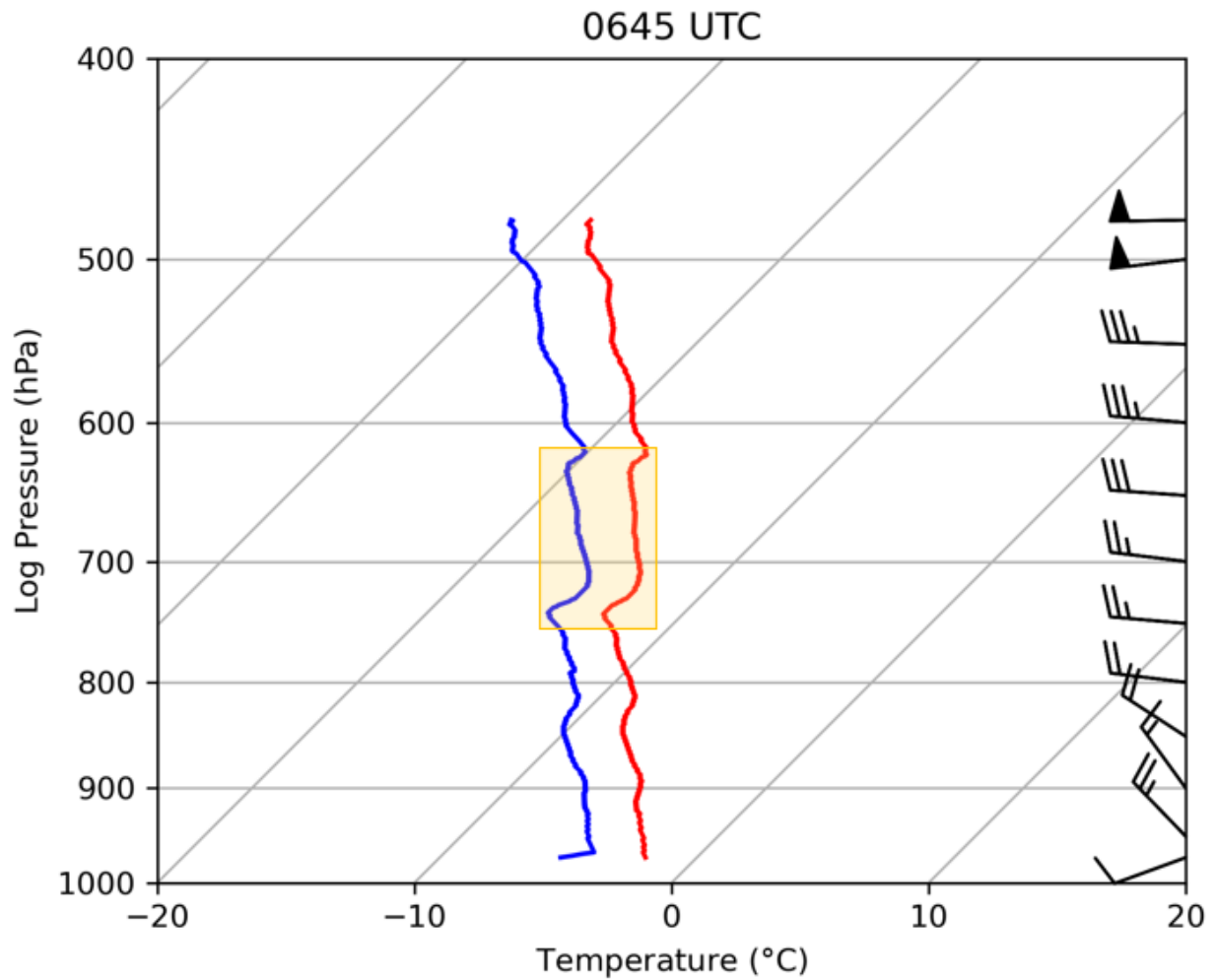


Figure 40 – Data from the radiosonde launched with the PASIV plotted on a skew- T log- p diagram. The portion of the profile within the dendritic growth zone is highlighted in the yellow box.

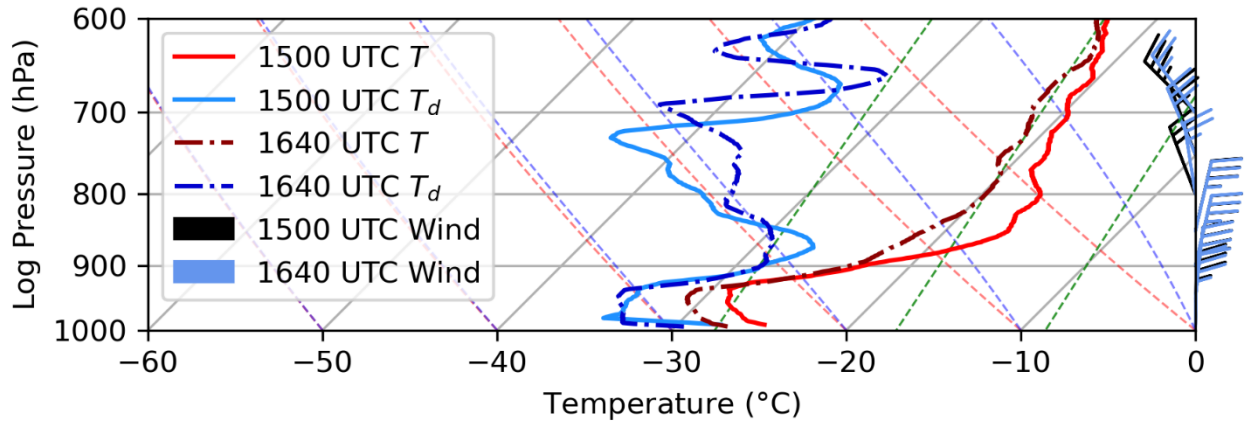


Figure 41 – A skew- T log- p showing the thermodynamic profiles from radiosondes launched at 1500 and 1640 UTC. The solid red and blue lines are the respective temperature and dewpoint profiles at 1500 UTC. The dot-dashed maroon and dark blue lines are the respective temperature and dewpoint profiles at 1640 UTC. The black and periwinkle wind barbs are the winds throughout the column at 1500 and 1640 UTC, respectively.

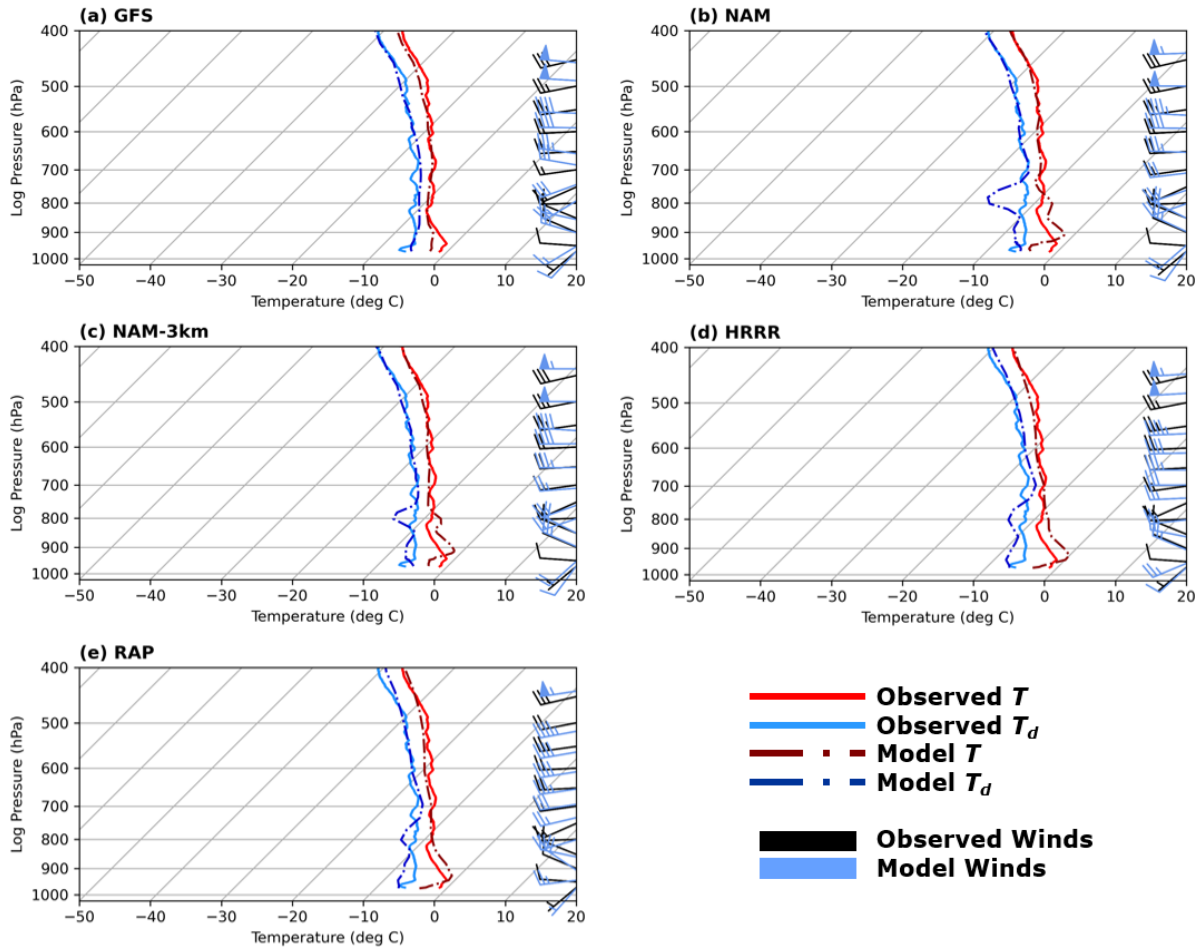


Figure 42 – The 0500 UTC observed sounding is overlaid with multiple 00 UTC model soundings 5 model hours out (0500 UTC model time). The observed sounding is compared to (a) the GFS, (b) the NAM, (c) the NAM-3km, (d) the HRRR, and (e) the RAP. In each panel, the solid red and blue lines are the observed temperature and dewpoint profiles, respectively, and the dot-dashed maroon and navy lines are the model temperature and dewpoint profiles, respectively. The black wind barbs are observed winds and the periwinkle wind barbs are model winds.

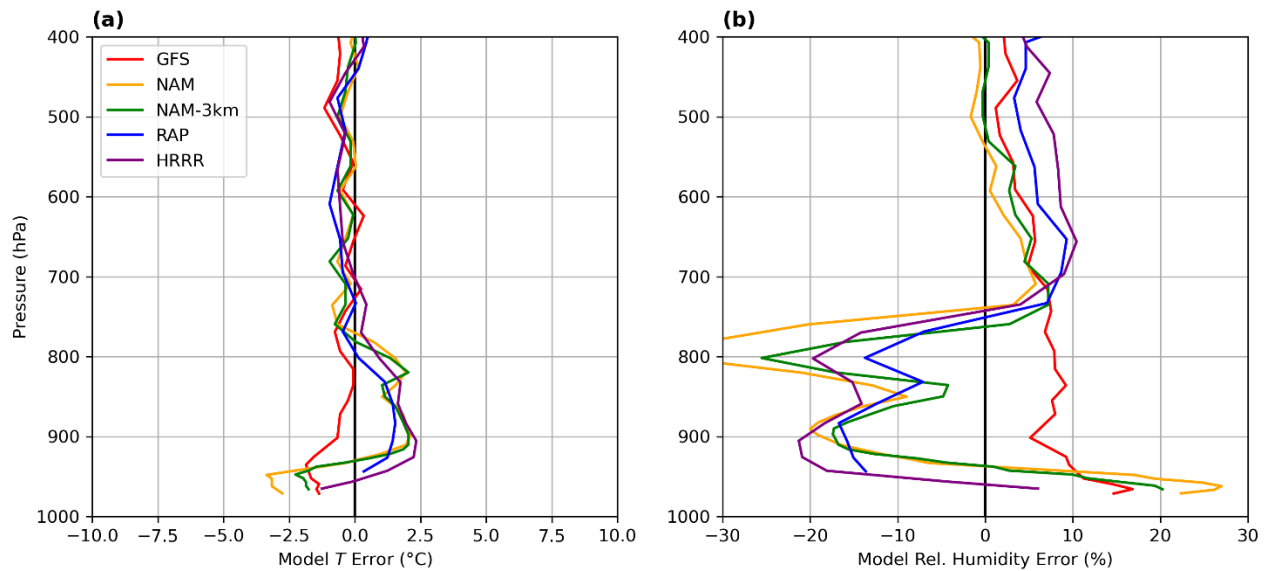


Figure 43 – Panel (a) shows 00 UTC model temperature error at model hour 5 (0500 UTC model time) compared to observed temperatures at 0500 UTC. Panel (b) is the same as (a), except for relative humidity. The thick black line at 0.0 °C in (a) is the respective observed temperature, and the thick black line at 0% in (b) is the respective observed relative humidity. The colored lines are the model error. In both panels, the red line is GFS model error, the yellow line is NAM model error, the green line is NAM-3km model error, the blue line is RAP model error, and the purple line is HRRR model error.

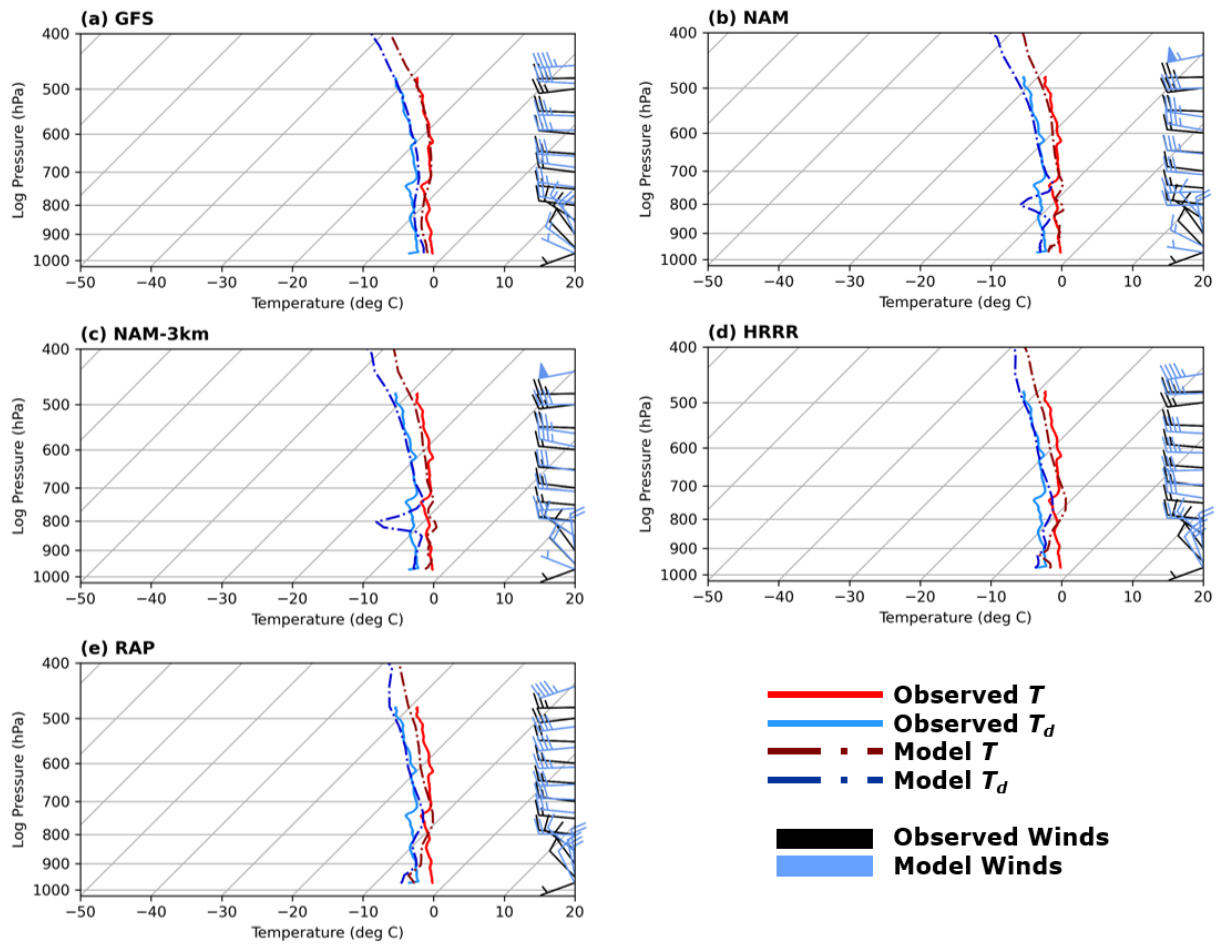


Figure 44 – As in Fig. 42, except for 0645 UTC observations versus 00 UTC models at model hour 7 (0700 UTC model time).

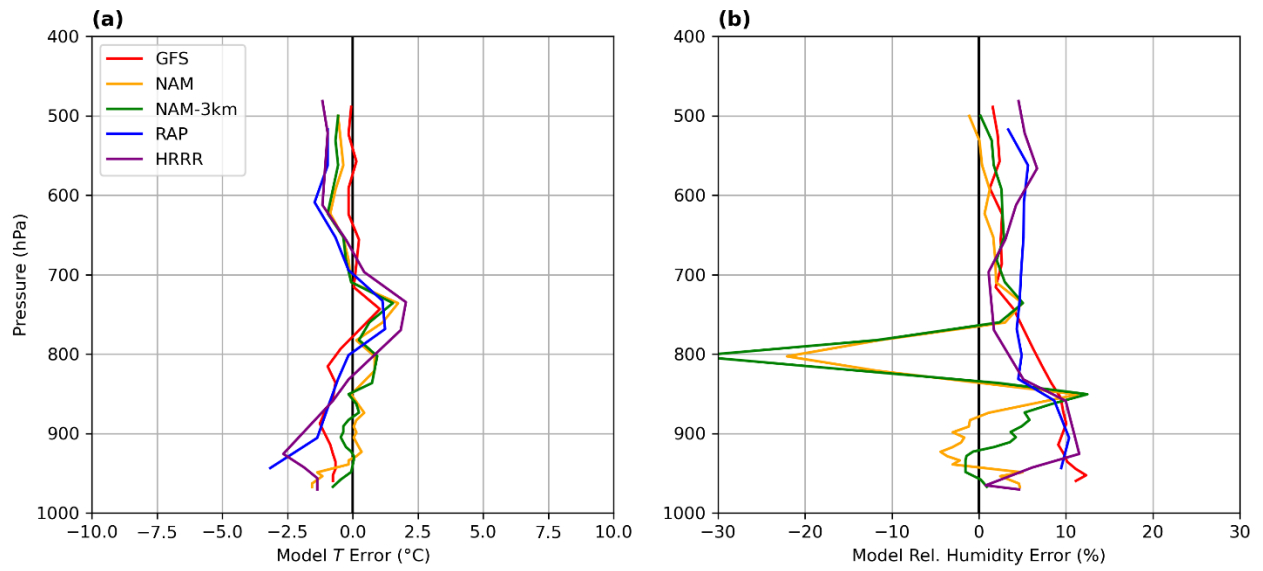


Figure 45 – As in Fig. 43, except for 0645 UTC observations versus 00 UTC models at model hour 7 (0700 UTC model time).

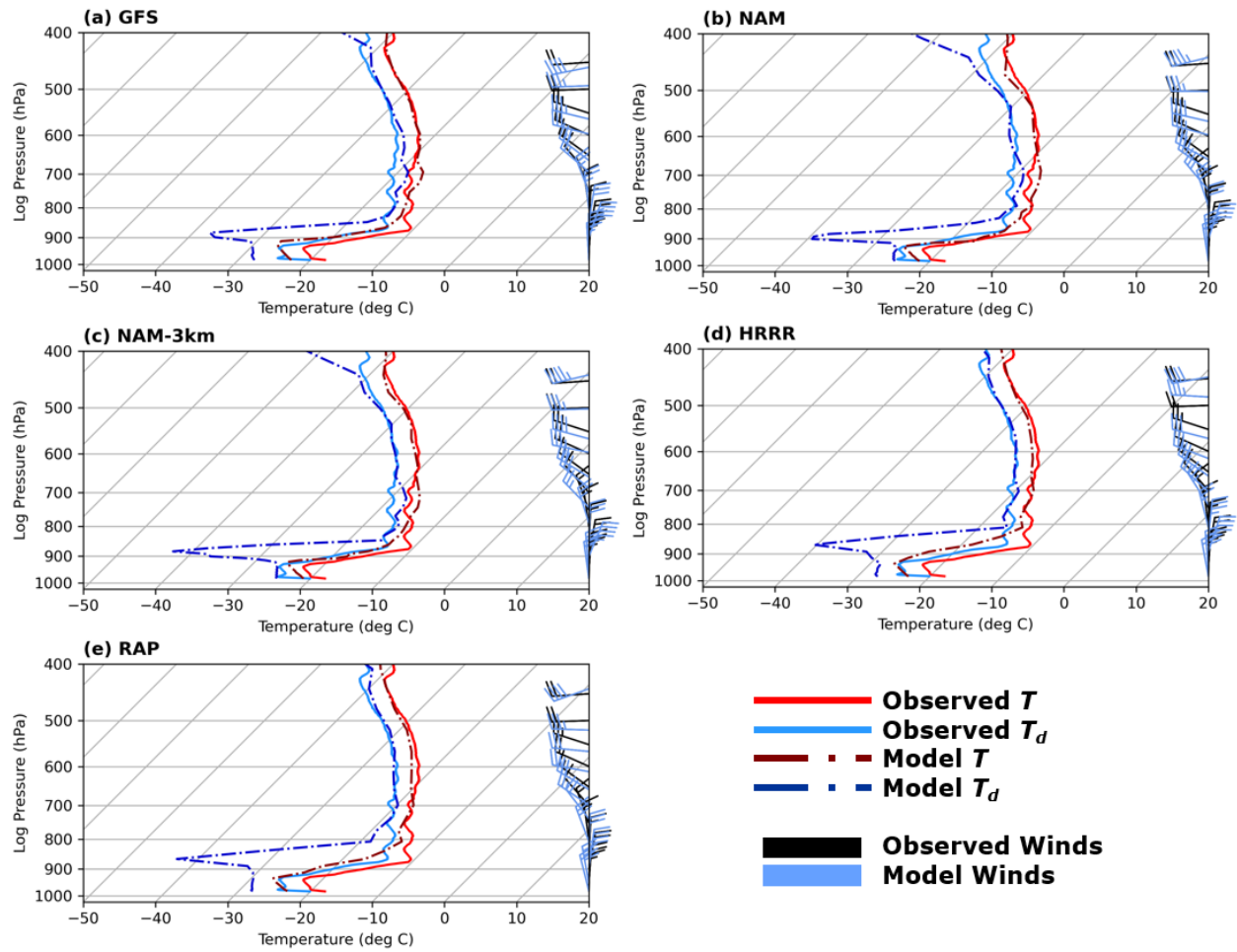


Figure 46 – As in Fig. 42, except for 1140 UTC observations versus 00 UTC models at model hour 12 (1200 UTC model time).

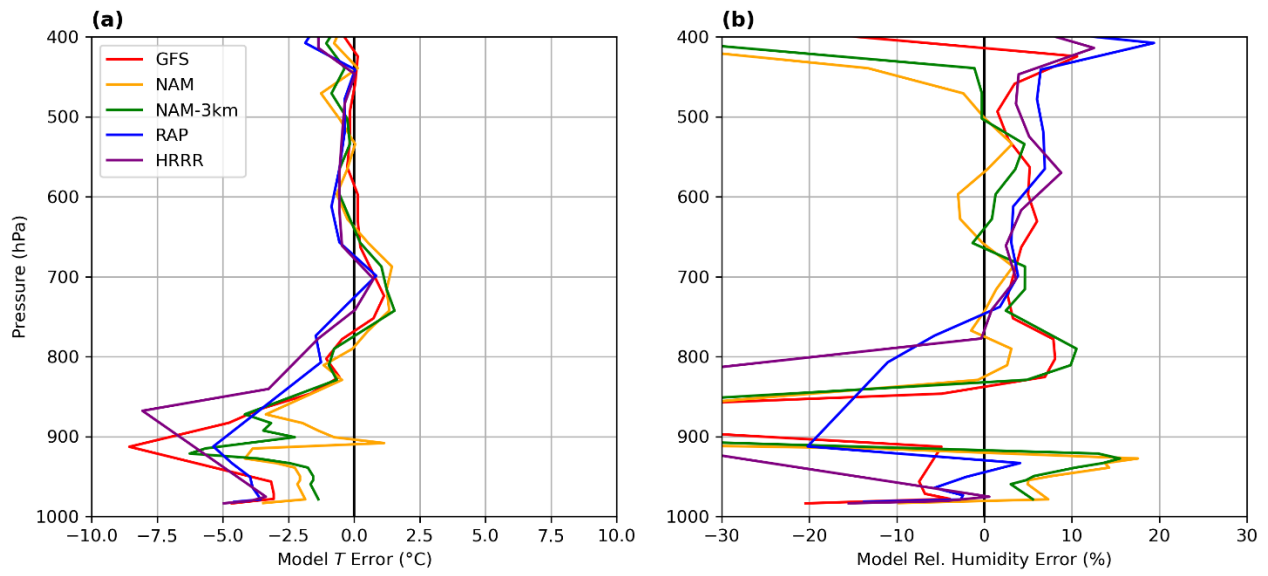


Figure 47 – As in Fig. 43, except for 1140 UTC observations versus 00 UTC models at model hour 12 (1200 UTC model time).

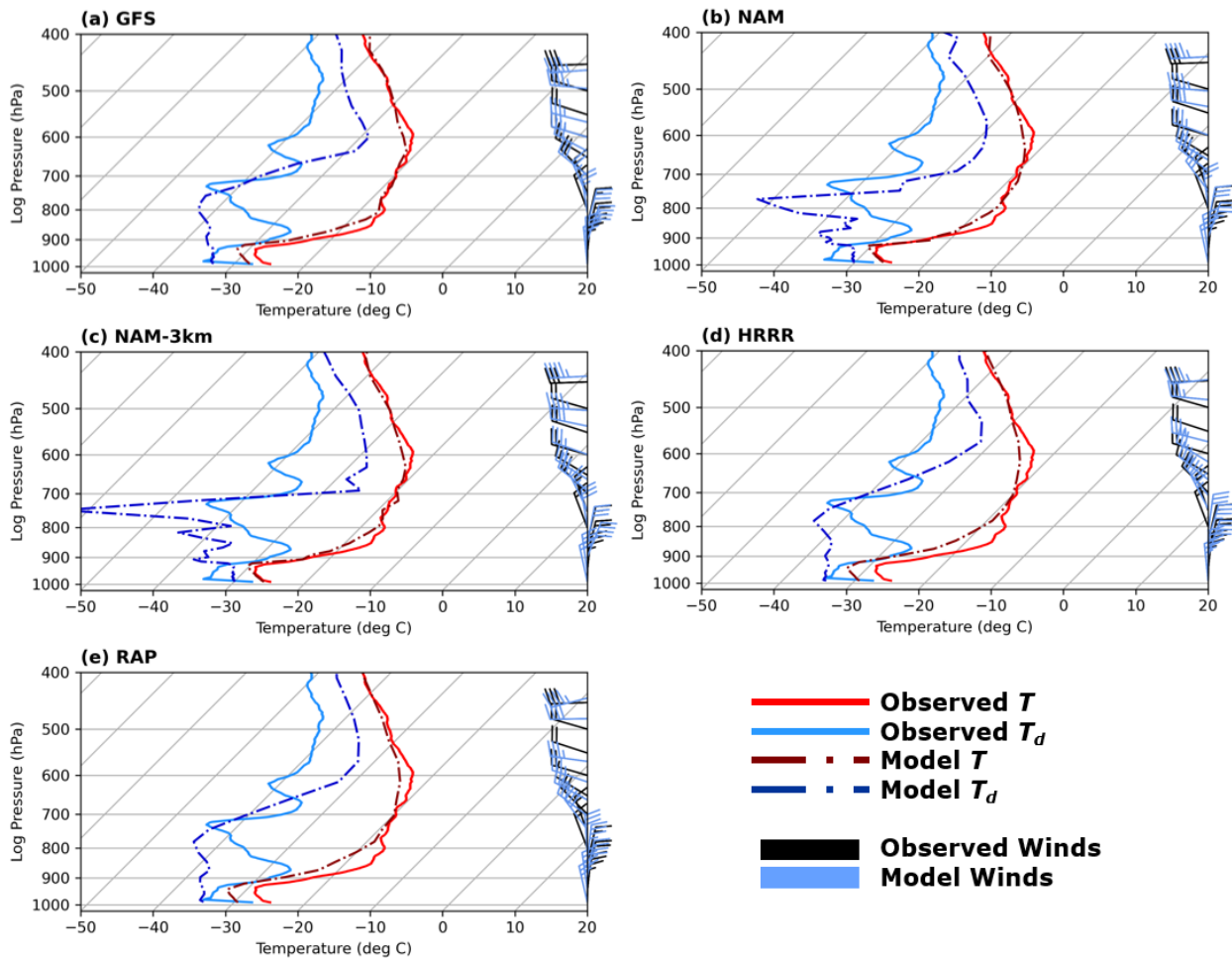


Figure 48 – As in Fig. 42, except for 1500 UTC observations versus 00 UTC models at model hour 15 (1500 UTC model time).

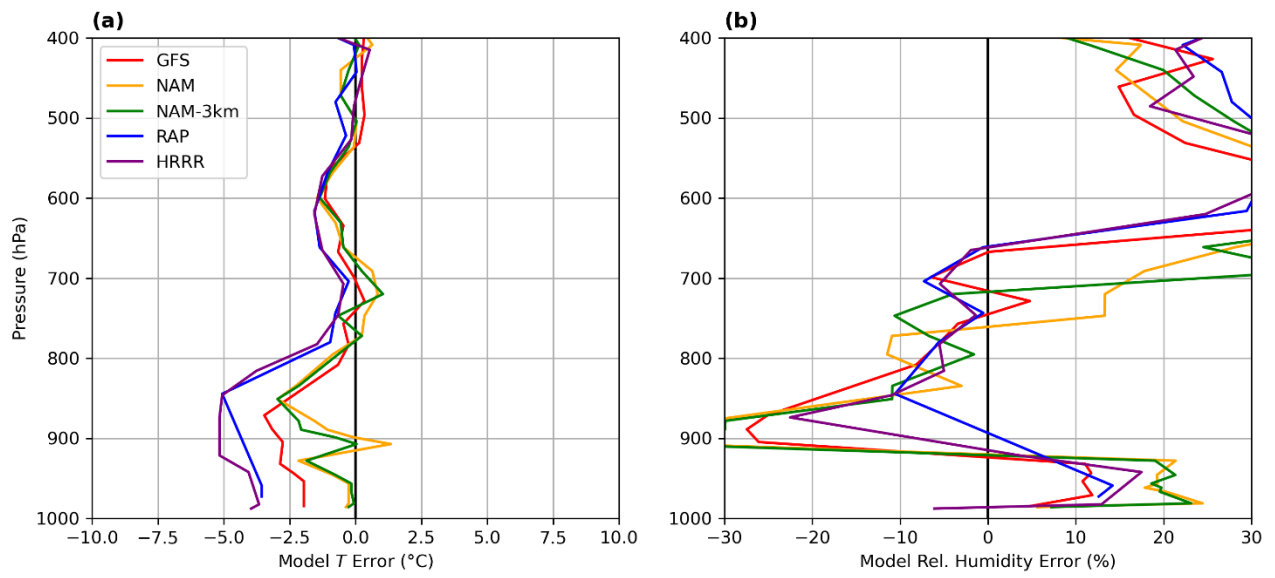


Figure 49 – As in Fig. 43, except for 1500 UTC observations versus 00 UTC models at model hour 15 (1500 UTC model time).

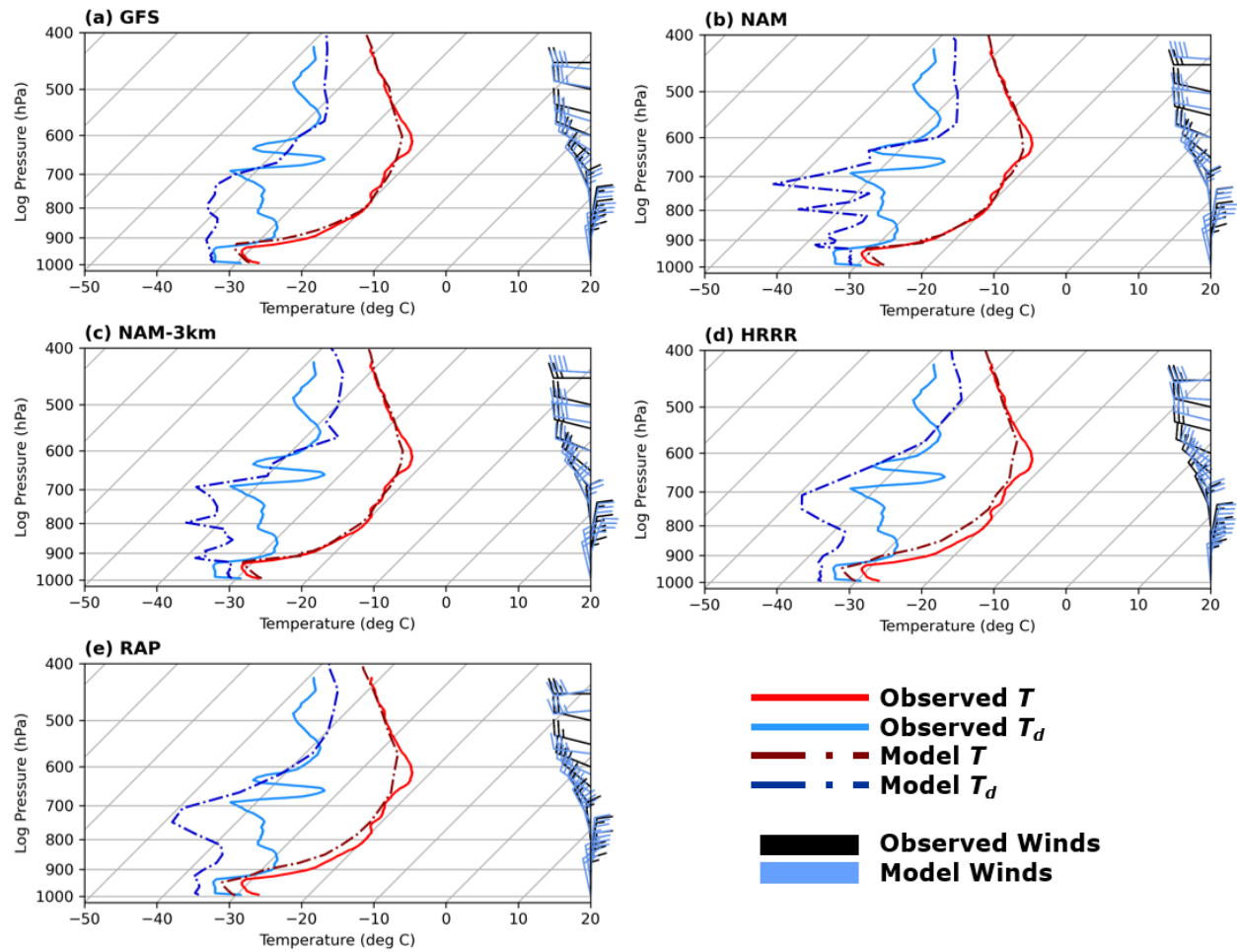


Figure 50 – As in Fig. 42, except for 1640 UTC observations versus 00 UTC models at model hour 17 (1700 UTC model time).

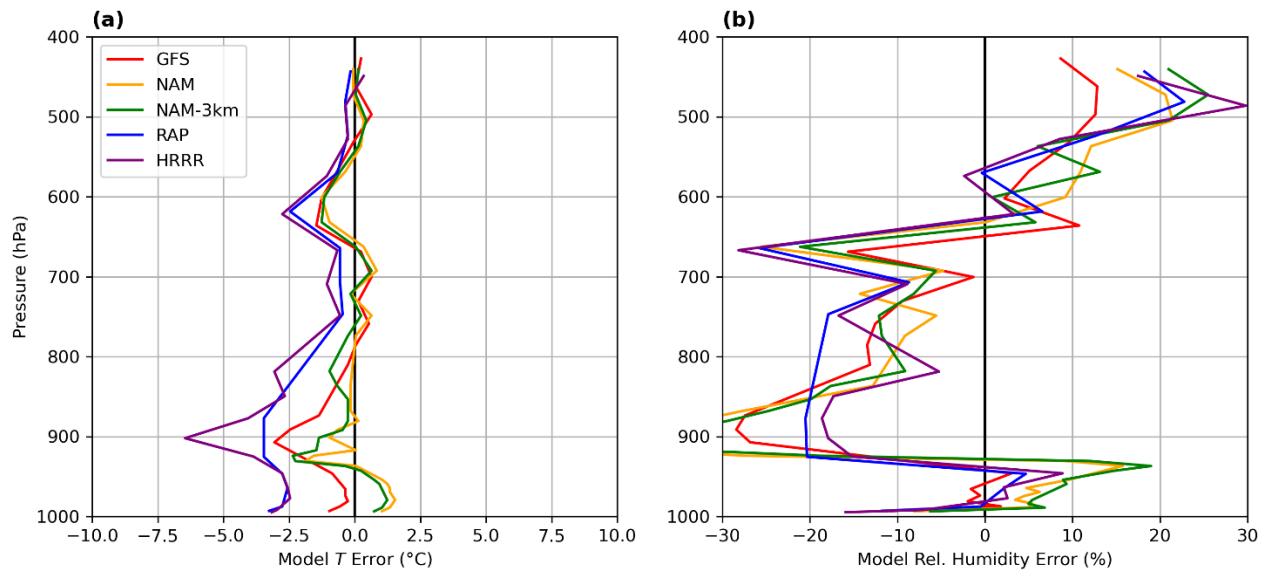


Figure 51 – As in Fig. 43, except for 1640 UTC observations versus 00 UTC models at model hour 17 (1700 UTC model time).

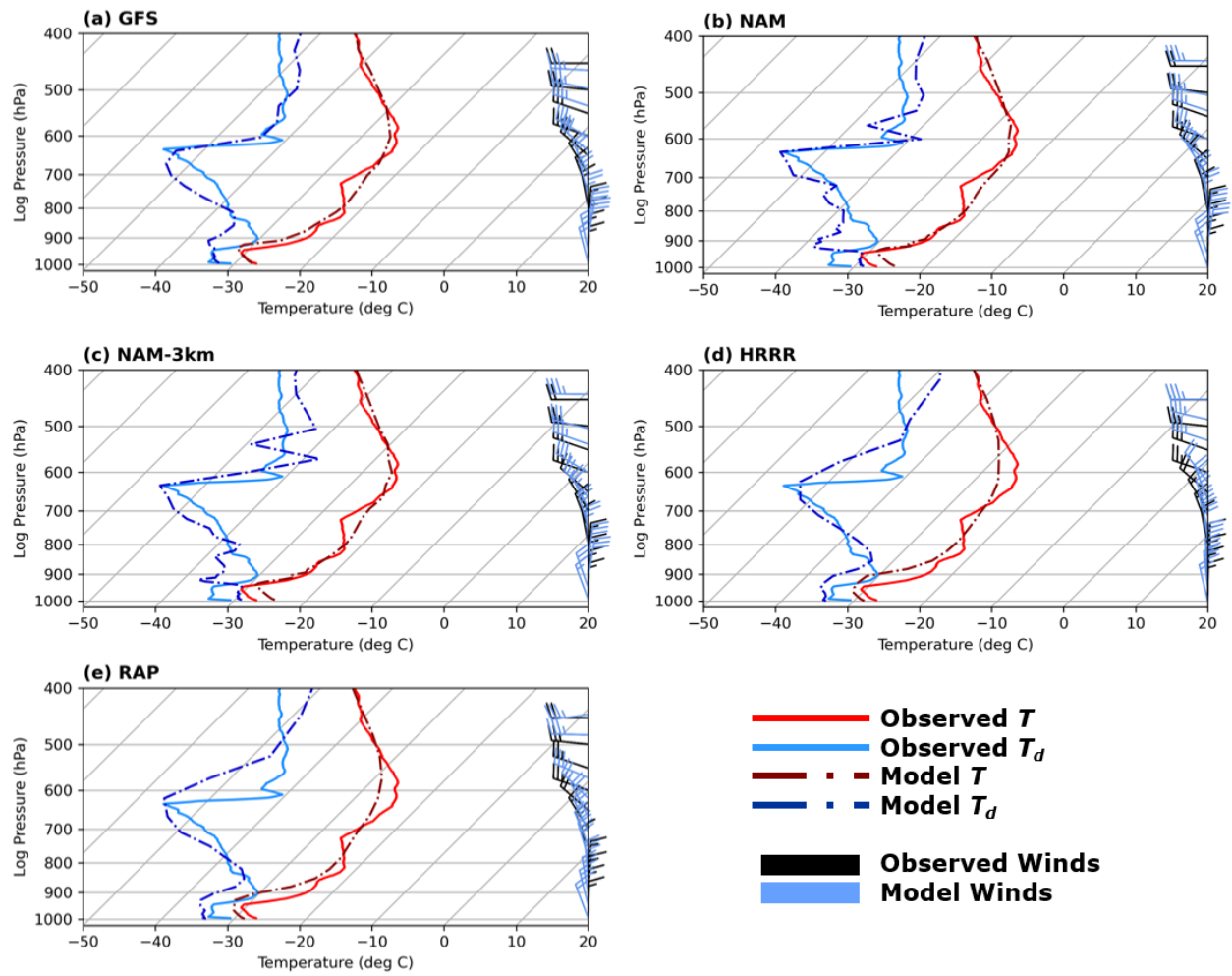


Figure 52 – As in Fig. 42, except for 1945 UTC observations versus 00 UTC models at model hour 20 (2000 UTC model time).

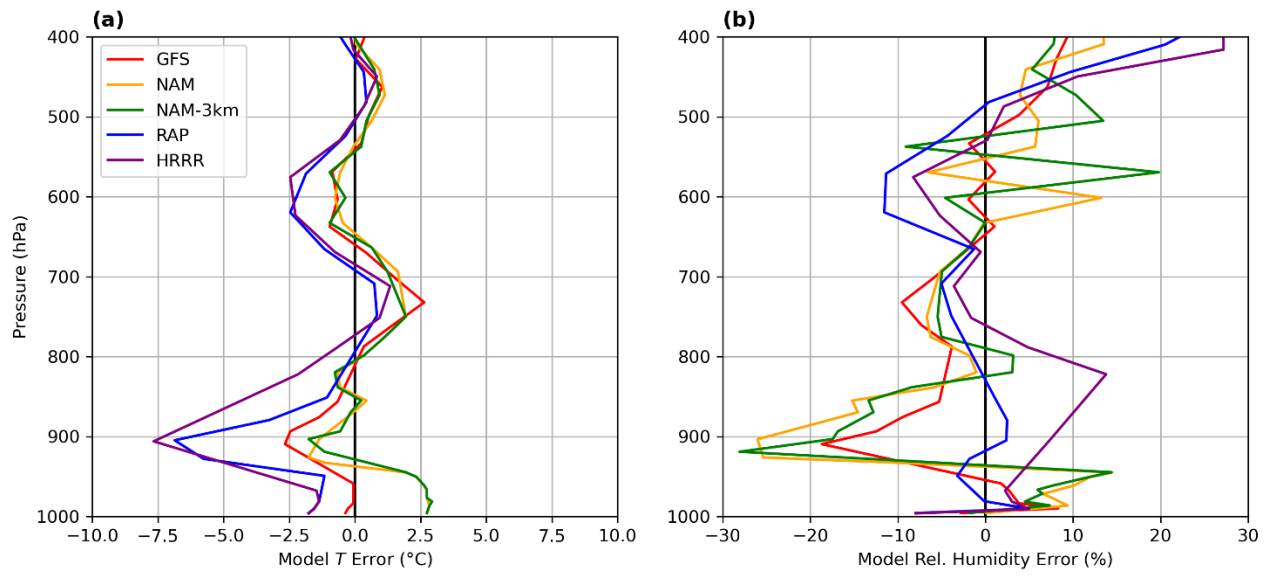


Figure 53 – As in Fig. 43, except for 1945 UTC observations versus 00 UTC models at model hour 20 (2000 UTC model time).

CHAPTER 5

SUMMARY AND CONCLUSIONS

This thesis focused on assessing the 12 February 2020 RRV ground blizzard, an intense blizzard that served as the climax to the BLOWN-UNDER campaign during the winter of 2019-2020. In this event, a vast suite of instrumentation allowed for groundbreaking observations of blowing snow and blizzard conditions, leading to the most comprehensive study of a RRV blizzard to date. An analysis of instrument performance followed in addition to a thorough assessment of the event's meteorology, including an in-depth look into blowing snow plumes. The results of the presented work are summarized hereon.

12 Feb 2020 Synopsis

The 12 Feb 2020 event was a classic RRV ground blizzard and the most intense blizzard of the 2019-2020 winter season. The event was driven by an Arctic Front wherein lobe and cleft instability with the front and Kelvin-Helmholtz billows within the turbulence just behind the front likely aided in dislodging and suspending snow from the surface. Behind the front, blowing snow congregated into HCR-like plumes, creating an environment where blizzard conditions reigned within the plumes and clear skies were observed outside the plumes. With northerly flow, blowing snow plumes were largely confined to the valley. Throughout the event, observations were collected using radar and lidar, balloon-borne instrumentation, microphysical imaging instrumentation, and satellites.

Instrument Performance

The extreme conditions in a ground blizzard pose challenges to maintaining instrument

functionality. Additionally, a few instruments were tested to see how well they would operate in blizzard conditions, such as the PASIV, the Parsivel², and the Lufft ceilometer.

Prior to the BLOWN-UNDER campaign, the PASIV had only been used in summertime thunderstorm research. It was an experiment in itself to determine if it could handle the cold and high winds of a Northern Plains blizzard. Overall, the instrument performed well, however its size proved to be a limitation. First, the amount of helium needed to lift the instrument off the ground is significantly greater than the amount used to lift a radiosonde. Second, controlling the balloon and the instrument on the surface before take-off is difficult in blizzard conditions. In blowing snow research, a smaller instrument that performs the same function would be desirable to satisfy the need for less helium and greater control.

Parsivel² performance in blowing snow was tested to determine if it accurately measures the dimensions of lofted snowflakes. The OSCRE was used as ground truth since photographic imagery is used to obtain measurements. It was shown that the Parsivel² significantly overestimates particle sizes. It is hypothesized that this is due to 1) the differences in surroundings, where the location of the OSCRE can obstruct wind flow, and 2) the Parsivel² counting multiple snowflakes as singular, larger snowflakes. While these hypotheses are plausible and PSD data support them, a lack of comparable particle counts due to differences in instrument field of view and environment make it impossible to come to a definitive conclusion. This assessment is a project for future work.

The Lufft ceilometer was an excellent resource for much of the winter for deciphering the layers of the atmosphere being affected by precipitation, virga, clouds, or other suspended particles. However, it was shown through this event that the instrument has limitations when subjected to blowing snow as the signal was attenuated for several hours and did not return to

normal operation until wind speeds and blowing snow began to subside. Future use of additional ceilometers is planned to survey the atmosphere during blowing snow events and to determine if all ceilometers suffer the same degree of attenuation in more intense blizzard conditions.

Two other instruments that did not operate as expected throughout the event were DOW7 and UND NorthPol. DOW7 worked well through the first few hours of the event, but unfortunately succumbed to blowing snow being lodged into various equipment, forcing the truck to shut down shortly after 1200 UTC. UND NorthPol was operational throughout the event but had issues with data quality where unrealistic return signals were observed at all elevation and zenith angles. It is hypothesized that faulty equipment within the radar dome may have caused the data issues. All other instruments operated and functioned as expected.

Boundary Layer Evolution and Blowing Snow Plumes

The boundary layer evolved significantly throughout the event. Before the Arctic frontal passage, winds were minimal and conditions were tranquil, notwithstanding the pre-frontal precipitation. Immediately after the front, the boundary layer was incredibly turbulent as evidenced by Kelvin-Helmholtz billows on RHI radar scans. Within an hour, post-frontal flow became more laminar with modest, intermittent turbulence in the vertical associated with HCR updrafts causing blowing snow plumes. The entire boundary layer cooled off considerably throughout the event, with temperatures falling 26.3 °C at the surface and 23.5 °C at 925 hPa from 0645 to 1640 UTC.

Radiosondes were launched outside and inside of blowing snow plumes at 1500 and 1640 UTC, respectively. Between the two times the boundary layer cooled by ~2 °C. It is not certain if this is due to sublimation, cold air advection, or a combination of the two. The boundary layer inside of the blowing snow plume was observed to be more moist near the surface and dryer aloft

than outside of the blowing snow plume. At 975 hPa, relative humidity increased from 42% to 62% (+20%), and at 930 hPa the relative humidity increased from 58% to 65% (+7%). This may be indicative of sublimation of blowing snow adding extra moisture to the lower boundary layer. The entirety of the boundary layer was more moist inside the blowing snow plume than outside – the boundary layer averaged 55.0% relative humidity outside versus 65.1% inside. Later in the event, as blowing snow died down, the lower boundary layer experienced slight warming and drying, likely due to suspended snow falling out of the atmosphere. Since this study included an analysis of only one blowing snow plume, general conclusions cannot be made for all blowing snow plumes. To address this, it is ideal to launch more radiosondes into blowing snow plumes and to launch the radiosondes from various locations to better understand the horizontal thermodynamic profile of the atmosphere in these events. This is a subject of future work.

Blowing snow plumes were observed with radar, lidar, and satellites. Comparing the height of the blowing snow with the height of the boundary layer from the radiosondes, blowing snow was confined to the boundary layer, peaking at less than 500 m in depth. Based on radar observations, these plumes seemed to be forced by vertical momentum fluxes from rising branches of HCRs. The initial forcing mechanism for this is unknown and is the subject of future work. Additionally, the aspect ratio of the blowing snow plumes earlier in the event was 8.89–10.0, which is comparable to past research (Kennedy and Jones 2020). Later in the event, satellite observations combined with radiosonde data suggested aspect ratios between 4.70–23.5. It is unclear if the size and spacing of the blowing snow plumes can be forecasted based on the depth of the boundary layer or by HCR orientation with respect to the valley (Kennedy and Jones [2020] observed rolls with similar aspect ratios, but within a deeper boundary layer and within flow non-parallel to the valley). Future observations will need to be collected to determine if a correlation exists.

Model Performance

Overall, the operational models performed poorly with this event, particularly with thermodynamics and kinematics. After the frontal passage and through the first 10 hours of the event, all models struggled with temperature, moisture, and wind speeds. The NAM and NAM-3km handled boundary layer temperatures the best throughout the event, but had a poor handle on the moisture profiles throughout the column, favoring a moist boundary layer. The other models tended to have a cold and moist boundary layer until the end of the event, with temperatures and dewpoints being more than 3 °C too cold in the boundary layer in the hours after the frontal passage. While it is not known for certain why the models had cold and moist biases, it is hypothesized that the models were too forward with cold air advection with moist biases being a by-product of the cold biases. All models simulated the atmosphere drying out above the boundary layer later into the event, whereas it was observed that dewpoints increased with increasing temperature above the boundary layer. This resulted in all models having dewpoint errors of greater than 10 °C in layers above the boundary layer and RH more than 30% too low. With respect to wind, all the models handled wind direction decently with errors limited to 20° in most cases post-frontal passage. However, all models had a negative speed bias in the boundary layer, with winds that were 2.5-7.7 m s⁻¹ (5-15 kts) too weak through much of the event. Wind speed errors improved toward the end of the event as observed winds began to die down with a reduced pressure gradient.

Although the model performance was lackluster, it was expected that the models would not perform well. None of the operational models have an active blowing snow parameterization, and thus assume that once snow reaches the surface, it stays on the surface. Due to this, moisture in the column will be inaccurate since blowing snow and subsequent sublimation are not simulated.

In addition, since blowing snow is not present in the models, radiation and energy fluxes will be inaccurate as well, resulting in inaccurate temperature forecasts. Data from this event can be used to test blowing snow parameterizations – however, much more data will be needed to initiate and test models with blowing snow parameterizations. This is an important area of future work.

References

- Asai, T., 1971: Stability of a plane parallel flow with variable vertical shear and unstable stratification. *J. Meteor. Soc. Japan*, **48**, 129-139.
- Atkinson, B. W. and J. W. Zhang, 1996: Mesoscale shallow convection in the atmosphere. *Rev. Geophys.*, **34**, 403-431.
- Barral, H., C. Genthon, A. Trouvilliez, C. Brun, and C. Amory, 2014: Blowing snow in coastal Adélie Land, Antarctica: three atmospheric-moisture issues. *Cryosphere*, **8**, 1905-2014, doi: 10.5194/tc-8-1905-2014.
- Benjamin, T. B., 1968: Gravity currents and related phenomena. *J. Fluid Mech.*, **31**, 209-248.
- Bintanja, R. and M. R. van den Broeke, 1995: The surface energy balance of Antarctic snow and blue ice. *J. Appl. Meteor.*, **34**, 902-926.
- , 2001a: Modelling snowdrift sublimation and its effect to the moisture budget of the atmospheric boundary layer. *Tellus*, **53A**, 215-232, doi: 10.3402/tellusa.v52i2.12189.
- , 2001b: Characteristics of snowdrift over a bare ice surface in Antarctica. *J. Geophys. Res.*, **106**, 9653-9659
- Bourdages, L., T. J. Duck, G. Lesins, J. R. Drummond, and E. W. Eloranta, 2009: Physical properties of High Arctic tropospheric particles during winter. *Atmos. Chem. Phys.*, **9**, 6881-6897.
- Brown, R. A., 1980: Longitudinal instabilities and secondary flows in the planetary boundary layer: a review. *Rev. Geophys.*, **18**, 683-697, doi: 10.1029/RG018i003p00683.
- Budd, W. F., 1966: The drifting of non-uniform snow particles. *Studies in Antarctic Meteorology*, M. J. Rubin, American Geophysical Union, 59-70.
- Budd, W. F., W. R. J. Dingle, and U. Radok, 1966: The Byrd snowdrift project: outline and basic results. *Studies in Antarctic Meteorology*, M. J. Rubin, American Geophysical Union, 71-134.
- Burrows, W. R., R. A. Treidl, and R. G. Lawford, 1979: The Southern Ontario blizzard of January 26 and 27, 1978. *Atmosphere-Ocean*, **17**, 306-320, doi: 10.1080/07055900.1979.9649068.

- Call, D. A., 2005: Rethinking snowstorms as snow events. *Bull. Amer. Meteor. Soc.*, **86**, 1783-1794, doi: 10.1175/BAMS-86-12-1783.
- Chandrasekar, V. and V. N. Bringi, 1987: Simulation of radar reflectivity and surface measurements of rainfall. *J. Atmos. Oceanic Technol.*, **4**, 464-478, doi: 10.1175/1520-0426(1987)004<0464:SORRAS>2.0.CO;2.
- Coleman, J. S. M. and R. M. Schwartz, 2017: An updated climatology of the Contiguous United States (1959-2014): an examination of spatiotemporal trends. *J. Appl. Meteor. Climatol.*, **56**, 173-187, doi: 10.1175/JAMC-D-15-0350.1.
- Déry, S. J., P. A. Taylor, and J. Xiao, 1998: The thermodynamic effects of sublimating snow in the atmospheric boundary layer. *Boundary-Layer Meteorol.*, **89**, 251-283.
- Faller, A. J., 1965: Large eddies in the atmospheric boundary layer and their possible role in the formation of cloud rows. *J. Atmos. Sci.*, **22**, 176-184.
- Garrett, T. J., C. Fallgatter, K. Shkurko, and D. Howlett, 2012: Fall speed measurement and high-resolution multi-angle photography of hydrometeors in free fall. *Atmos. Measurement Techniques*, **5**, 2625-2633, doi: 10.5194/amt-5-2625-2012.
- Geerts, B., R. Damiani, and S. Haimov, 2006: Finescale vertical structure of a cold front as revealed by an airborne Doppler radar. *Mon. Wea. Rev.*, **134**, 251-271, doi: 10.1175/MWR3056.1.
- , B. Pokharel, and D. A. R. Kristovich, 2015: Blowing snow as a natural glaciogenic cloud seeding mechanism. *Mon. Wea. Rev.*, **143**, 5017-5033, doi: 10.1175/MWR-D-15-0241.1.
- Gelaro, R. and coauthors, 2017: The Modern-Era Retrospective Analysis for Research and Application, Version 2. *J. Climate*, **30**, 5419-5454, doi: 10.1175/JCLI-D-16-0758.1.
- Gordon, M. and P. A. Taylor, 2009: Measurements of blowing snow, Part I: particle shape, size distribution, velocity, and number flux at Churchill, Manitoba, Canada. *Cold Regions Science and Technol.*, **55**, 63-74, doi: 10.1016/j.coldregions.2008.05.00.
- , S. Savelyev, and P. A. Taylor, 2009: Measurements of blowing snow, Part II: mass and number density profiles and saltation height at Franklin Bay, NWT, Canada. *Cold Regions Science and Technol.*, **55**, 75-85, doi: 10.1016/j.coldregions.2008.07.001.

- Gossart, A., N. Souverijns, I. V. Gorodetskaya, S. Lhermitte, J. T. M. Lenaerts, J. H. Schween, A. Mangold, Q. Laffineur, and N. P. M. van Lipzig, 2017: Blowing snow detection from ground-based ceilometers: application to East Antarctica. *Cryosphere*, **11**, 2755-2772, doi: 10.5194/tc-11-2755-2017.
- Grossman, R. L., 1982: An analysis of vertical velocity spectra obtained in the BOMEX fair-weather, trade-wind boundary layer. *Bound.-Layer Meteor.*, **23**, 323-357.
- Grünewald, T., M. Schirmer, R. Mott, and M. Lehning, 2010: Spatial and temporal variability of snow depth and ablation rates in a small mountain catchment. *Cryosphere*, **4**, 215-225, doi: 10.5194/tc-4-215-2010.
- Härtel, C., E. Meiburg, and F. Necker, 2000: Analysis and direct numerical simulation of the flow at a gravity current head. Part 2: the lobe and cleft instability. *J. Fluid Mech.*, **418**, 213-229.
- Helmus, J. J. and S. M. Collis, 2016: The Python ARM Radar Toolkit (Py-ART), a library for working with weather radar data in the Python programming language. *J. Open Res. Software*, **4**, e25, doi: 10.5334/jors.119.
- Hershey, B. W. and L. F. Osborne, 2008: The physical nature and prediction of blowing snow within the roadway environment. *Surface Transportation Weather and Snow Removal and Ice Control Technology*, Volume Number E-C126, Fourth National Conference on Surface Transportation Weather, Transportation Research Circular, 676 pp.
- Johnson, E., 1962: The Prehistory of the Red River Valley. *Minnesota History*, **38**, 157-165.
- Jones, H. G., J. W. Pomeroy, D. A. Walker, and R. W. Hoham, 2001: *Snow Ecology: an Interdisciplinary Examination of Snow-Covered Ecosystems*. Cambridge University Press, 400 pp.
- Kapela, A. F., P. W. Leftwich, and R. F. Van Ess, 1995: Forecasting the Impacts of strong wintertime post-cold front winds in the Northern Plains. *Weather Forecast*, **10**, 229-244.
- Keller, F., F. Kienast, and M. Beniston, 2000: Evidence of response of vegetation to environmental change on high-elevation sites in the Swiss Alps. *Regional Environment Change*, **1**, 70-77.
- Kennedy, A., A. Trellinger, T. Grafenauer, and G. Gust, 2019: A climatology of atmospheric patterns associated with Red River Valley blizzards. *Climate*, **7**, 66, doi: 10.3390/cli7050066.

- and C. Jones, 2020: *GOES-16* Observations of Blowing Snow in Horizontal Convective Rolls on 24 February 2019. *Mon. Wea. Rev.*, **148**, 1737-1750, doi: 10.1175/MWR-D-19-0354.s1.
- , A. Scott, N. Loeb, A. Szczepanski, K. Lucke, J. Marquis, and S. Waugh, 2021: Bringing Microphysics to the Masses: The Blowing Snow Observation at the University of North Dakota: Education through Research (BLOWN-UNDER) Campaign. *Bull. Amer. Meteor. Soc.*, accepted for publishing.
- Kluver, D., T. Mote, D. Leathers, G. R. Henderson, W. Chan, and D. A. Robinson, 2016: Creation and validation of a comprehensive 1° by 1° daily gridded North American dataset for 1900-2009: snowfall. *J. Atmos. Oceanic Technol.*, **33**, 857-871, doi: 10.1175/JTECH-D-15-0027.1.
- Kocin, P. J., P. N. Schumacher, R. F. Morales Jr., and L. W. Uccellini, 1995: Overview of the 12-14 March 1993 Superstorm. *Bull. Amer. Meteor. Soc.*, **76**, 165-182.
- Lee, B. D. and R. B. Wilhelmson, 1997: The numerical simulation of non-supercell tornadogenesis, part I: initiation and evolution of pretornadic mesocyclone circulations along a dry outflow boundary. *J. Atmos. Sci.*, **54**, 32-60, doi: 10.1175/1520-0469(1997)054<0032:TNSONS>2.0.CO;2.
- LeMone, M. A., 1973: The structure and dynamics of horizontal roll vortices in the planetary boundary layer. *J. Atmos. Sci.*, **30**, 1077-1091.
- Lenaerts, J. T. M. and coauthors, 2016: Meltwater produced by wind-albedo interaction stored in an East Antarctic ice shelf. *Nature Climate Change*, **7**, 58-62, doi: 10.1038/nclimate3180.
- Letcher, T. W., S. A. LeGrand, and C. Polashenski, 2021: Applying a physically based blowing snow diagnostic parameterization to improve wintertime visibility forecasts in the WRF model. *Wea. Forecasting*, **36**, 615-626, doi: 10.1175/WAF-D-20-0106.1.
- Li, L. and J. W. Pomeroy, 1997: Estimates of threshold wind speeds for snow transport using meteorological data. *J. Appl. Meteor.*, **36**, 205-213.
- Lilly, D. K., 1966: On the instability of Ekman boundary flow. *J. Atmos. Sci.*, **23**, 481-494.
- Loeb, N. A and A. Kennedy, 2021: Blowing snow at McMurdo Station, Antarctica during the AWARE field campaign: surface and ceilometer observations. *J. Geophys. Res.*, **126**, e2020JD033935, doi: 10.1029/2020JD033935.

- Löffler-Mang, M. and J. Joss, 2000: An optical disdrometer for measuring size and velocity of hydrometeors. *J. Atmos. Oceanic Technol.*, **17**, 130-139.
- Luce, C. H., D. G. Tarboton, and K. R. Cooley, 1998: The influence of the spatial distribution of snow on basin-averaged snowmelt. *Hydrol. Processes*, **12**, 1671-1683.
- Mahesh, A., R. Eager, J. R. Campbell, and J. D. Spinhirne, 2003: Observations of blowing snow at the South Pole. *J. Geophys. Res.*, **108**, 4707-4716, doi: 10.1029/2002JD003327.
- Mann, G. W., P. S. Anderson, and S. D. Mobbs, 2000: Profile measurements of blowing snow at Halley, Antarctica. *J. Geophys. Res.*, **105**, 24491-24508, doi: 10.1029/2000JD900247.
- May, R. M., S. C. Arms, P. Marsh, E. Bruning, J. R. Leeman, K. Goebbert, J. E. Thielen, and Z. S. Bruick, 2021: MetPy: A Python package for meteorological data. Unidata, <https://github.com/Unidata/MetPy>, doi: 10.5065/D6WW7G29.
- NCEI, 2021: 1991-2020 Climate Normals. Accessed 21 May 2021, <https://www.ncei.noaa.gov/access/us-climate-normals/>.
- NDSU, 2021: North Dakota Agricultural Weather Network. Accessed 17 May 2021, <https://ndawn.ndsu.nodak.edu>.
- Niziol, T. A., 1987: Operational forecasting of lake effect snowfall in Western and Central New York. *Wea. Forecasting*, **2**, 310-321.
- NOAA ASOS, 2021: Automated Surface Observing Systems. Accessed 17 May 2021, <https://www.weather.gov/asos/>.
- NOHRSC, 2021: Regional Snow Analyses: Upper Midwest. Accessed 15 June 2021, https://www.nohrsc.noaa.gov/nsa/index.html?region=Upper_Midwest&year=2020&month=2&day=12&units=e#snow_reports.
- NWS, 2021: Blizzard definition. Accessed 19 May 2021, <https://w1.weather.gov/glossary/index.php?word=blizzard>.
- Palm, S. P., Y. Yang, J. D. Spinhirne, and A. Marshak, 2011: Satellite remote sensing of blowing snow properties over Antarctica. *J. Geophys. Res.*, **16**, D16123, doi: 10.1029/2011JD015828.

- , V. Kayetha, Y. Yang, and R. Pauly, 2017: Blowing snow sublimation and transport over Antarctica from 11 years of *CALIPSO* observations. *Cryosphere*, **11**, 2555-2569, doi: 10.5194/tc-11-2555-2017.
- , Y. Yang, V. Kayetha, and J. P. Nicolas, 2018: Insight into the thermodynamic structure of blowing-snow layers in Antarctica from dropsonde and *CALIPSO* measurements. *J. Appl. Meteor. Climatol.*, **57**, 2733-2748, doi: 10.1175/JAMC-D-18-0082.1.
- Pazmany, A., R. McIntosh, R. Kelly, and G. Vali, 1994: An airborne 95 GHz dual-polarized radar for cloud studies. *IEEE Trans. Geosci. Remote Sens.*, **32**, 731-739.
- Pomeroy, J. W., 1988: *Wind Transport of Snow*. PhD Thesis, Division of Hydrology, University of Saskatchewan, Saskatoon, 226pp.
- , D. H. Male, 1988: Optical properties of blowing snow. *J. Glaciol.*, **34**, 3-10, doi: 10.3189/S0022143000008996.
- , P. Marsh, and D. M. Gray, 1997: Application of a distributed blowing snow model to the Arctic. *Hydrol. Processes*, **11**, 1451-1464.
- and R. L. H. Essery, 1999: Turbulent fluxes during blowing snow: field tests of model sublimation predictions. *Hydrol. Processes*, **13**, 2963-2975.
- Rignot, E., I. Velicogna, M. R. van den Broeke, A. Monaghan, and J. T. M. Lenaerts, 2011: Acceleration of the contribution of the Greenland and Antarctic ice sheets to sea level rise. *Geophys. Res. Letters*, **38**, L05503, doi: 10.1029/2011GL046583.
- Rinehart, R. E., 1997: *Radar for Meteorologists*. Rinehart Publications, 428 pp.
- Rooney, J. F., 1967: The urban snow hazard of the United States: an appraisal of disruption. *Geographical Rev.*, **57**, 538-559, doi: 10.2307/212932.
- Rossi, E., 1999: *White Death: The Blizzard of '77*. Seventy Seven (77) Publishing, 432 pp.
- Savelyev, S. A., M. Gordon, J. Hanesiak, T. Papakyriakou, and P. A. Taylor, 2006: Blowing snow studies in the Canadian Ice Shelf Exchange Study, 2003-04. *Hydrol. Processes*, **20**, 817-827, doi: 10.1002/hyp.6118.
- Schaer, M., C. Praz, and A. Berne, 2020: Identification of blowing snow particles in images from a Multi-Angle Snowflake Camera. *Cryosphere*, **14**, 367-384, doi: 10.5194/tc-14-367-2020.

- Schmidt, R. A., 1972: *Sublimation of Wind-Transported Snow*. USDA Forest Service, 24 pp.
- , 1980: Threshold wind speeds and elastic impact in snow transport. *J. Glaciol.*, **34**, 453-467.
- , 1982: Vertical profiles of wind speed, snow concentrations, and humidity in blowing snow. *Boundary-Layer Meteor.*, **23**, 223-246.
- Schmit, T. J., P. Griffith, M. M. Gunshor, J. M. Daniels, S. J. Goodman, and W. J. Lebar, 2017: A closer look at the ABI on the GOES-R series. *Bull. Amer. Meteor. Soc.*, **98**, 681-698, doi: 10.1175/BAMS-D-15-00230.1.
- , S. S. Lindstrom, J. J. Gerth, and M. M. Gunshor, 2018: Applications of the 16 spectral bands on the Advanced Baseline Imager (ABI). *J. Operational Meteor.*, **6**, 33-46, doi: 10.15191/nwajom.2018.0604.
- Schwartz, R. M. and T. W. Schmidlin, 2002: Climatology of blizzards in the conterminous United States, 1959-2000. *J. Climate*, **15**, 1765-1772, doi: 10.1175/1520-0442(2002)015<1765:COBITC>2.0.CO;2.
- Sekhon, R. S. and R. C. Srivastava, 1970: Snow size spectra and radar reflectivity. *J. Atmos. Sci.*, **27**, 299-307, doi: 10.1175/1520-0469(1970)027<0299:SSSARR>2.0.CO;2.
- Seliga, T. A. and V. N. Bringi, 1976: Potential use of radar differential reflectivity measurements at orthogonal polarizations for measuring precipitation. *J. Appl. Meteor.*, **15**, 69-76.
- Simpson, J. E., 1972: Effects of the lower boundary layer on the head of a gravity current. *J. Fluid Mech.*, **53**, 759-768.
- Smith, Jr., P. L., C. G. Myers, and H. D. Orville, 1975: Radar reflectivity factor calculations in numerical cloud models using bulk parameterization of precipitation. *J. Appl. Meteor.*, **14**, 1156-1165, doi: 10.1175/1520-0450(1975)014<1156:RRFCIN>2.0.CO;2.
- Stensrud, D. J. and H. N. Shirer, 1988: Development of boundary layer rolls from dynamic instabilities. *J. Atmos. Sci.*, **45**, 1007-1019.
- Stewart, R. E. and coauthors, 1995: Winter storms over Canada. *Atmos.-Ocean*, **33**, 223-247, doi: 10.1080/070559900.1995.9649533.

- Thiery, W., I. V. Gorodetskaya, R. Bintanja, N. P. M. Van Lipzig, M. R. van den Broeke, C. H. Reijmer, and P. Kuipers Munneke, 2012: Surface and snowdrift sublimation at Princess Elisabeth station, East Antarctica. *Cryosphere*, **6**, 841-857, doi: 10.5194/tc-6-841-2012.
- Tokay, A., W. A. Petersen, P. Gatlin, and M. Wingo, 2013: Comparison of raindrop size distribution measurements by collocated disdrometers. *J. Atmos. Oceanic Technol.*, **30**, 1672-1690, doi: 10.1175/JTECH-D-12-00163.1.
- Walter, B. A., 1980: Wintertime observations of roll clouds over the Bering Sea. *Mon. Wea. Rev.*, **108**, 2024-2031, doi: 10.1175/1520-0493(1980)108<2024:WOORCO>2.0.CO;2.
- Walter, B., H. Huwald, J. Gehring, Y. Bühler, and M. Lehning, 2020: Radar measurements of blowing snow off a mountain ridge. *Cryosphere*, **14**, 1779-1794, doi: 10.5194/tc-14-1779-2020.
- Waugh, S. M., C. L. Ziegler, D. R. MacGorman, S. E. Fredrickson, D. W. Kennedy, and W. D. Rust, 2015: A balloonborne Particle Size, Imaging, and Velocity probe for in situ microphysical measurements. *J. Atmos. Oceanic Technol.*, **32**, 1562-1580, doi: 10.1175/JTECH-D-1400216.1.
- Weckwerth, T. M., J. W. Wilson, R. M. Wakimoto, and N. A. Crook, 1997: Horizontal convective rolls: determining the environmental conditions supporting their existence and characteristics. *Mon. Wea. Rev.*, **125**, 505-526.
- , T. W. Horst, and J. W. Wilson, 1999: An observational study of the evolution of horizontal convective rolls. *Mon. Wea. Rev.*, **127**, 2160-2179.
- Woodcock, A. H., 1942: Soaring over the open sea. *Sci. Mon.*, **55**, 226-232.
- Wurman, J., J. Straka, E. Rasmussen, M. Randall, and A. Zahrai, 1997: Design and deployment of a portable, pencil-beam, pulsed, 3-cm Doppler Radar. *J. Atmos. Oceanic Technol.*, **14**, 1502-1512.
- Xie, C. Y., J. J. Tao, and L. S. Zhang, 2019: Origin of lobe and cleft at the gravity current front. *Physical Rev.*, **100**, 031103.
- Yamanauchi, T. and S. Kawaguchi, 1985: Effects of drifting snow on surface radiation budget in the katabatic wind zone, Antarctica. *Annals of Glaciol.*, **6**, 238-241.

- , K. Suzuki, and S. Kawaguchi, 1987: Detection of clouds in Antarctica from infrared multi-spectral data of AVHRR. *J. Meteor. Soc. Japan*, **65**, 949-962.
- Yang, Y., S. P. Palm, A. Marshak, D. L. Wu, H. Yu, and Q. Fu, 2014: First satellite-detected perturbations of outgoing longwave radiation associated with blowing snow events over Antarctica. *Geophys. Res. Lett.*, **41**, 730-735, doi: 10.1022/2013GL058932.
- , A. Anderson, D. Kiv, J. Germann, M. Fuchs, S. Palm, and T. Wang, 2020: Study of Antarctic blowing snow storms using MODIS and CALIOP observations with a machine learning model. *Earth and Space Sci.*, **8**, 2020EA001310, doi: 10.1029/2020EA001310.
- Young, G. S., D. A. Kristovich, M. R. Hjelmfelt, and R. C. Foster, 2002: Rolls, streets, waves, and more: a review of quasi-two-dimensional structures in the atmospheric boundary layer. *Bull. Amer. Meteor. Soc.*, **83**, 997-1002, doi: 10.1175/1520-0477(2002)083<0997:RSWAMA>2.3.CO;2.
- , T. D. Sikora, and N. S. Winstead, 2005: Use of synthetic aperture radar in finescale surface analysis of synoptic-scale fronts at sea. *Wea. Forecasting*, **20**, 311-327, doi: 10.1175/WAF853.1.